國立交通大學

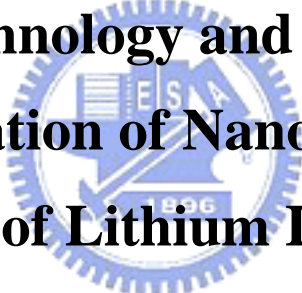## 材料科學與工程學系

博士論文

分散技術及其在奈米陶瓷和鋰電池電極製備之應用研究

Dispersion Technology and Its Applications to the Fabrication of Nano-ceramics and Electrode of Lithium Ion Battery

學生姓名：應國良（Kuo- Liang Ying）

指導教授：謝宗雍 博士（Dr. Tsung-Eong Hsieh）

中華民國96年10月

分散技術及其在奈米陶瓷和鋰電池電極製備之應用研究

學生：應國良　　　　　　　　　　　　　　指導教授：謝宗雍 博士

國立交通大學 材料科學與工程學系

摘　　要

本論文探討奈米分散技術及其在鈦酸鋇（BaTiO₃，BTO）奈米陶瓷和鋰電池中鋰鈷氧（LiCoO₂）之電極製備之應用；鈦酸鋇相關之陶瓷材料包含純鈦酸鋇、鈦酸鍶鋇（Ba₀.₇Sr₀.₃TiO₃，BST）和添加氧化鑭之鈦酸鍶鋇（La₂O₃-doped BST，LBST）。奈米陶瓷實驗中使用兩性之氨丙基丙醯胺（α-N，N-2 甲基-丙烯乙基氧，Polyacrylamide/(α-N，N-dimethyl-N-acryloyloxyethyl) Ammonium Ethanate，PDAAE）和陰離子型高分子分散劑（聚甲基丙烯酸，Poly(methacrylic Acid，PMAA-Na）為分散劑，本研究另合成一種新型之樹枝狀高分子分散劑（聚（4-4，2 苯 胺 甲 基 苯 氧 基 鄰 苯 二 甲 酐 ）， Poly(4-{4-[di(4-aminophenyl)methyl]phenoxy}phthalic Ether Imide，PEI）以分散奈米碳管（Carbon Nanotube，CNT）並應用於鋰電池鋰鈷氧電極基板 之製備中，以提高鋰電池之效能。

奈米鈦酸鍶鋇及其相關之陶瓷係利用物理研磨加上化學分散進行製備漿料，分散效果之測試包含：黏度、沈降體積、表面電位和高分子分散劑之吸附量來判斷粉體之分散狀況，之後奈米粉體再經過適當之燒結過程而製成電容並測試其相關之介電性質。實驗中發現，控制燒結環境條件可將奈米陶瓷粉末燒結成具有良好之微結構、結晶相和介電特性之電容元件。

奈米陶瓷部份之主要研究成果如下：奈米鈦酸鋇在經由 1100°C，6 小時之燒

結可獲得小晶粒、高密度和良好之介電性質（室溫下介電常數為 8000，介電損失為 5×10^{-3}）之電容元件。其次，高密度（≥ 95%）、高介電性質之奈米鈦酸鍶鋇電容可藉 1200°C、6 小時燒結製程（晶粒大小約為 200 nm，室溫下介電常數為 9700，介電損失為 0.04）或 1300°C、1 小時燒結製程（晶粒大小約為 220 nm，室溫下介電常數為 9800，介電損失為 0.075）而獲得。此外，奈米鈦酸鍶鋇電容相較於傳統之鈦酸鋇及鈦酸鍶鋇具有較低之居禮溫度。最後，添加 1 *mol.*%氧化鑭之鈦酸鍶鋇經由 1400°C、1 小時燒結可得晶粒大小約為 200 nm、最佳之介電常數為 13800 和最低之介電損失 2.8×10^{-4} 之電容元件。

在關於奈米碳管之分散部分，經由等溫吸附曲線、流變和沈降實驗得知 PEI 之最佳劑量為 2 *wt.*%（此係相對於奈米碳管重量之比例）。由電化學阻抗光譜（Electrochemical impedance spectroscopy，EIS）之量測得發現電池之交流阻抗由 287 Ω（電極未添加 PEI）降至 161 Ω（電極中含 2 *wt.*%之 PEI），而其主要之原因為分散良好之奈米碳管在電極中形成一網狀結構並藉此提供良好之電荷轉移路徑。在充放電實驗（Charge-discharge Test）中發現，電極含分散良好之奈米碳管之鋰電池在大電流放電下（8 C）其放電容值仍可維持在 74 %（電流密度為 101 mAh/g），高放電容量和較長之壽命將有助於大型鋰電池在高電源工具、電動腳踏車、電動摩托車等之應用。

Dispersion Technology and Its Applications to the Fabrication of Nano-ceramics and Electrode of Lithium Ion Battery

Student: Kuo-Liang Ying   Advisor: Dr. Tsung-Eong Hsieh

Department of Materials Science and Engineering

National Chiao-Tung University

Abstract

This thesis discusses the dispersion technology and their applications to the fabrication of barium titanate (BaTiO$_3$, BTO)-relating nano-ceramics and LiCoO$_2$ electrode of lithium ion battery (LIB). The BTO-relating ceramics include the genuine BTO, Ba$_{0.7}$Sr$_{0.3}$TiO$_3$ (BST) and La$_2$O$_3$-doped BST (LBST). An amphibious dispersant, polyacrylamide/(α-N, N-dimethyl-N-acryloyloxyethyl) ammonium ethanate (PDAAE), and an anionic dispersant, poly(methacrylic acid) (PMAA-Na), were adopted to the dispersion of nano-ceramics. A new dispersant, poly(4-{4-[di(4-aminophenyl)methyl]phenoxy}phthalic ether imide) (PEI), was synthesized for the dispersion of carbon nanotube (CNT) conduction agent in LiCoO$_2$ electrode so as to improve the performance of high power LIBs.

BST-relating nano-ceramic powders were prepared *via* a physical grinding in conjunction with the chemical dispersion. Dispersion properties including viscosity, sedimentation volume, particle size distribution, zeta-potential and isothermal adsorption were investigated so as to determine the optimal dispersion condition. The capacitor samples were then prepared by appropriate sintering process and then

dielectric property measurement was followed. It was found that specific control on sintering condition is required for the nano-ceramic powders to achieve desired microstructure, crystalline phase and dielectric properties of devices.

The major achievements in BTO-relating nano-ceramics are as follows. BTO sample sintered at 1100°C for 6 hrs possesses relatively small grain sizes (about 140 nm), high density (about 95% T.D.) and distinct room-temperature dielectric properties (dielectric constant = 8000; dielectric loss = 5×10^{-3}). High-density ($\geq 95\%$) BST samples with desired dielectric properties could be obtained *via* sintering at 1200°C for 6 hrs (grain size $\approx$ 200 nm; dielectric constant = 9700; dielectric loss = 0.04) or at 1300°C for 1 hr (grain size $\approx$ 220 nm; dielectric constant = 9800; dielectric loss = 0.075). Besides, the BST samples exhibited a lower Curie point (T_C) in comparison with conventional BTO and BST systems. The 1.0 *mol*.% La-doped BST sample sintered at 1400°C for 1 hr possesses the finest grain size about 200 nm, the highest dielectric constant about 13800 and lowest dielectric loss about 2.8×10^{-4}.

In the part relating to the dispersion of CNT, the optimal amount of PEI (about 2 *wt*.% relating to the weight of CNT) was determined by means of the studies of adsorption isotherm, rheology and sedimentation behaviors. Electrochemical impedance spectroscopy (EIS) revealed that the ac resistance of electrode decreases from 287 Ω for cell without PEI to 161Ω for the cell at containing optimal amount of PEI. This is attributed to the network established by dispersed CNTs that effectively promotes the charge carrier migration in electrode. The C-rate test indicated that at the high-rate discharge test results, that the LIB test cell with modified electrode possesses 8 C-discharge capacity of 101 mAh/g, which is about 74% of its 0.2 C-discharge capacity. The results of high rate capability and long cycle life evidences the promising applications of such a LIB to power sources, *e.g.*, power tools, electric bicycle, electric motorcycle, *etc*.

致　　　謝

Contents

List of Figures

xiv

Table Captions

List of Symbols

C: capacitance

ε_r: relative dielectric constant

ε_0: dielectric constant in vacuum

d_{50}: mean particle size

Ce: equilibrium concentration of dispersants in solution

As: adsorbent of the dispersant

Cm: monolayer adsorbent of the dispersant

CHAPTER 1

Introduction

Emergence of nano-materials has attracted numerous research interests in last decade. Nano-materials involve fundamental studies in various fields of physics and chemistry as well as the applications in electronics, mechanics, biotechnology, *etc*. A major difficulty encountered in the study of nano-scale materials is their appgrgation.[1-3] When the size of materials is reduced to nano-scale, they tend to aggregate together due to the van der Waals force attraction resulted from large specific surface area (SSA). Appropriate dispersive technique is hence one of the key issues to realize the applications of nano-materials in various occassions.[3,4]
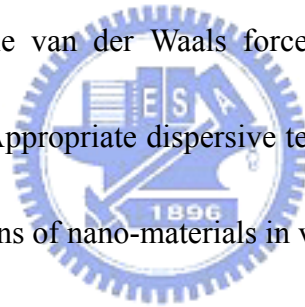
Colloidal processing comprises of the dispersion of fine ceramic particles in a liquid medium and subsequent consolidation of the colloidal particle. This assists in producing a uniform microstructure and high packing density for the powder compaction.[5-8] The dispersibility of the colloidal suspension affects both the sintering behaviors and resultant properties of the dense ceramics. Dispersants such as polyacrylic acid, ammonium salt of polyacryloc acid, polymethacrylic acid, ammonium polymethacrylate and phosphate ester are added to prepare a stable suspension with high content of ceramic powder and high-density green body.[9-12] In

first part of this thesis study, we investigate the dispersion method and preparation of nano-scale BTO-relating (BTO, BST and La-doped BST) ceramic powders *via* a combination process of mechanical grinding and chemical dispersion utilizing the known PDAAE and PMAA-Na dispersants. The sintering behavior, microstructure changes and dielectric properties of capacitor samples fabricated based on such nano-ceramic powders were investigated accordingly. Experimental results showed that the nano-ceramic samples possess relatively small grain sizes, high density and distinct room-temperature dielectric properties under a specific control on the sintering condition of samples. For nano-BTO sample, dielectric constant = 8000 and dielectric loss = 5×10^{-3} were achieved. For nano-BST sample, dielectric constant = 9700 and dielectric loss = 0.04 were achieved. The dramatic improvement of dielectric properties in comparison with conventional BTO-relating ceramics was mainly attributed to the fine microstructure in the samples. As to the La-doped BST sample, the best dielectric properties are dielectric constant about 13800 and lowest dielectric loss about 2.8×10^{-4}. This was ascribed to the fine microstructure as well as the segregation of La elements in the grain boundaries which enhance the electrical polarization in the samples

In second part of this thesis study, we first synthesized a new chemical dispersant, PEI, that may be compatible to the $LiCoO_2$ electrode preparation process utilizing the

highly polar solvent, N-methyl pyrrolidone (NMP). The dispersant was then

implanted to the dispersion of CNT which serves as the conduction agent of electrode

in LIBs. The optimal dispersant content (relating to the weight of CNT) was

determined as 2 *wt.*% by means of the studies of adsorption isotherm, rheology and

sedimentation behaviors. Electrochemical impedance spectroscopy (EIS) revealed that

the ac resistance of electrode decreases from 287 Ω for cell without PEI to 161Ω for

the cell at containing optimal amount of PEI. This is attributed to the network

established by dispersed CNTs that effectively promotes the charge carrier migration

in electrode. The cycling performance showed that the test cell containing 2 *wt.*% PEI

obviously exhibits the better capacity retention in comparison with the cell free of PEI.

The C-rate test indicated that at the high-rate discharge test results, that the LIB test

cell with modified electrode possesses 8 C-discharge capacity of 101 mAh/g, which is

about 74% of its 0.2 C-discharge capacity. The results of high rate capability and long

cycle life evidences the promising applications of such a LIB to power sources, *e.g.*,

power tools, electric bicycle, electric motorcycle, *etc*.

CHAPTER 2

Literature Review

2.1. Dispersive Theory

2.1.1. Inter-particle Force[13]

The importance of inter-particle forces can be realized from the consideration of the stability of colloidal dispersion in medium. By controlling the inter-particle forces, colloidal suspension are able to disperse in various conditions, *e.g.*, weakly flocculation, or strongly flocculation, as shown in Fig. 2-1. From the plot of potential energy *versus* particle separation, the particles repel one another when they approach to a close distance and the positive potential implies the repulsive force in a well-dispersed state. In the weakly flocculate state, particles coagulate in a secondary minimum, forming flocs in a suspension. Mechanical forces, especially the shear force can disperse the flocs. In the strongly flocculated state, particles aggregate strongly by a primary minimum attractive force, forming clusters in the suspension.

Colloidal stability in ceramic systems is dominate by the total inter-particle energy, E_{total}, which can be simply expressed as

$$E_{total} = E_{vdW} + E_{elect} + E_{steric} \qquad (2.1)$$

where E_{vdW} is the attractive interaction due to short-range van der Waals interactions between particles, E_{elect} is the repulsive potential resulting from electrostatic interactions between charged particle surface, and E_{steric} is the repulsion between particle surfaces bearing polymeric species. The first two terms of Eq. (2.1) constitute the major part of Derjaguin-Landau-Verwey-Overbeek (DLVO) theory. Brief considerations of the theories underlying each of interaction are described as follows.
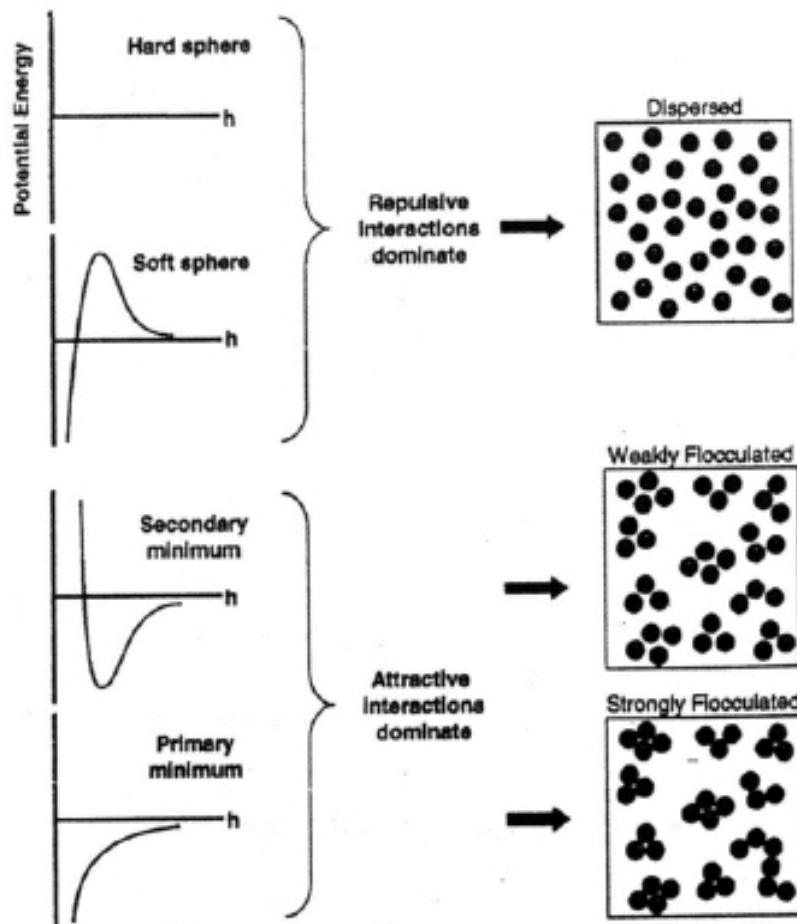
Figure 2-1. Illustration of the relationship between the total inter-particle interaction potential energy and resulting suspension structure.

2.1.2. DLVO Theory[14-17]

DLVO theory was simultaneously developed by Derjaguin, Landau, Verwey, and

Overbeek.[14-17] It is the interaction between charged particles. The theory is a central

concept for predicting colloidal stability. In the theory, the repulsive electrostatic term

is the source for a stable suspension and an attractive van der Waals force induces

flocculation of the particles. Under such a competition of two opposite forces, the

theory offers the understanding of colloidal powder processing phenomena.

According to the DLVO theory, the total energy between two particles is given

by

$$V_{total, DLVO} = V_{vdW} + V_{elect} \qquad (2.2)$$

where the $V_{total\ DLVO}$ is the total energy, V_{vdW} is the van der Waals attractive force, V_{elect}

is the electric repulsive force.

The total energy relationship to distance is shown in Fig. 2-2. This curve showed

the V_{max} (*i.e.*, the energy barrier). Some particles can pass through energy barrier to

lowest energy state (primary minimum) and reach a stable coagulation when particles

get close to each other. The work of the dispersant will increase the value of V_{max} and

avoid particles to aggregate.

In the view of long range forces, the attractive van der Waals forces, F_{vdW}, is

noticeably insensitive to variation in electrolyte concentration and pH value, and thus

it may be considered as constant in a first approximation. In contrast, at small enough

distances, the van der Waals attraction always exceeds the electrostatic repulsion. The

electrostatic interaction, in fact, rises more slowly as the separation distance approach

zero.[16,17]
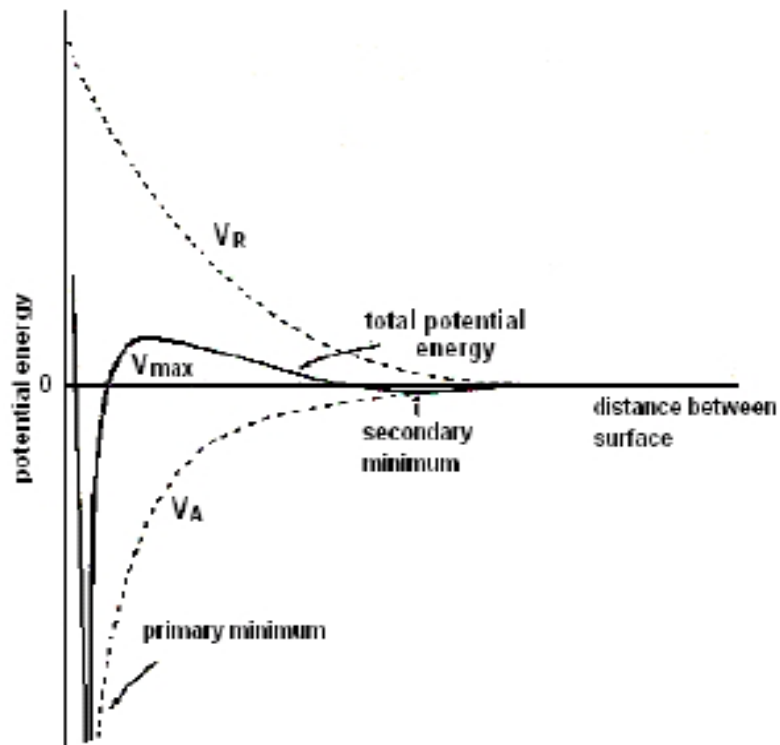
Figure 2-2. DLVO theory: the plot of total energy *versus* distance.

2.1.3. Electrostatic Double Layer Forces[18-21]

(1) Electrical Double Layer

Electrostatic forces repel the ions of same charge but attract oppositely charged ones into a thin, non-shear layer next to surface. Hence, in the polar liquid media, particles are able to develop a charge at the solid-liquid interface. Although net charge neutrality must be achieved, a difference in electrical potential between the surface and the bulk solution can be maintained, as shown in Fig. 2-3.[18]

(2) Zeta Potential

The electric potential at the shear plane is called a zeta potential. The zeta potential measured by an electrophoresis technique; the sign of zeta potential is the same sign of the surface charge. If all the particles in a suspension have a large negative or positive zeta potential then they will tend to repel each other. On the other hand, if the particles have a low zeta potential value, then there will be much less force to preclude the particles from coming together, and resulting in fluctuation. The general dividing line between stable and unstable suspensions with micro ceramic particles is generally taken at +30 or −30 mV. Particle with zeta potentials greater than 30 mV are generally considered as stable. [19-21]
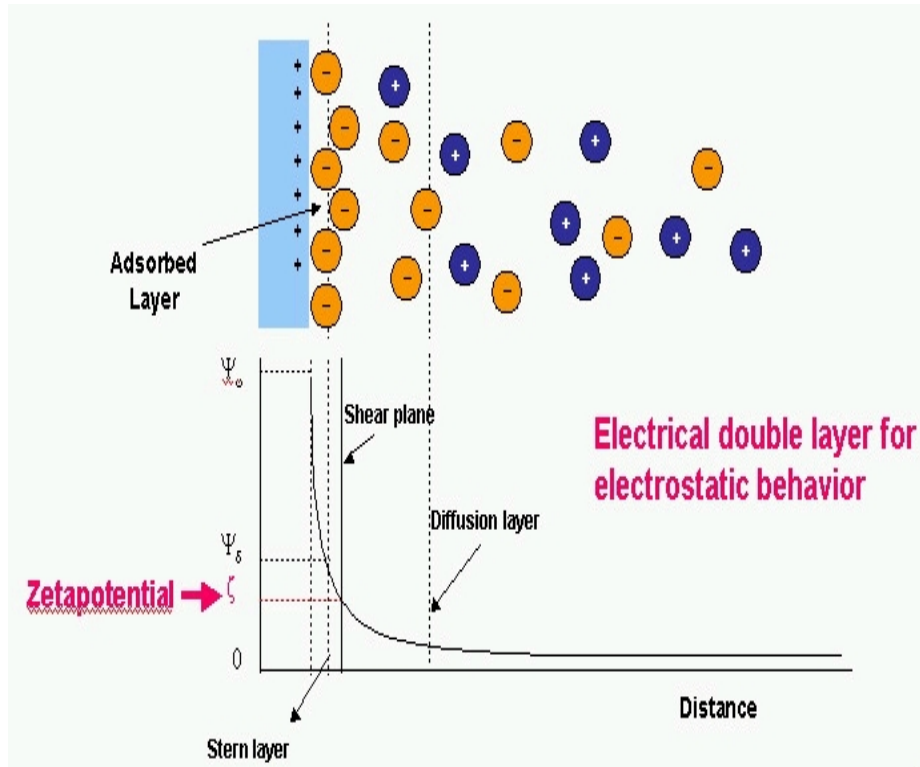
Figure 2-3. Structure of the electrical double layer.
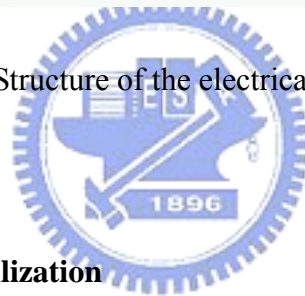
2.1.4. Polymer Induced stabilization

Polymers are usually applied as dispersants in ceramic colloidal processing. Steric stabilization of colloidal particles is imparted by the polymer attached to the particle surface. Since the spatial extensions of polymer molecules are usually in excess of the range of van der Waals attraction between colloidal particles, the polymers are capable of offering repulsion. One major advantage of polymers is that their dimensions are sensitive to electrolyte concentration, unlike electrical double layer.[17]

(1) Conformation of Adsorbed Polymers

9

The spatial extension of polymer molecules depends upon the mode of adsorption on the surface. If the chains are attached terminally at one end, they are referred to as *tails*. Terminal adsorption at both ends leads to *loops*. All segments abutting on the surface are termed *trains*. Schematic illustrations are shown in Fig. 2-4.[22,23]
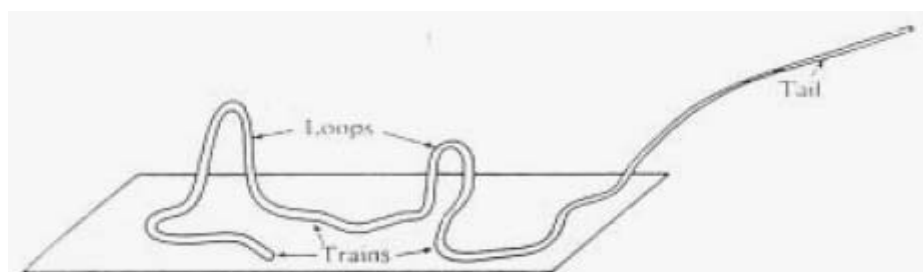
Figure 2-4. Conformations of homopolymer chains at the surface of a colloidal particle showing schematically trains, loops and tails

(2) Steric Forces

When two surfaces covered with polymer approach each other, once the separation distance is below a few radius of gyration, the outer segments start to overlap, which often results in a repulsive osmotic force because of the unfavorable entropy that occurs when the chains are compressed between the surfaces. This repulsion is usually referred to as the steric force as illustrated in Fig. 2-5.[13] To be effective, the thickness of adsorbed layer between particles must be large enough, thus,

the van der Waals attraction can be overwhelmed and bridging flocculation would be avoided. Besides, such polymers should be anchored strongly onto the particle surface to prevent desorption during particle collisions. Additionally, the thickness, the amount of the absorbed polymer, and solvency of the adsorbed polymer layers, and the affinity of the polymer to surface are all noticeable interrelated.[13,24]
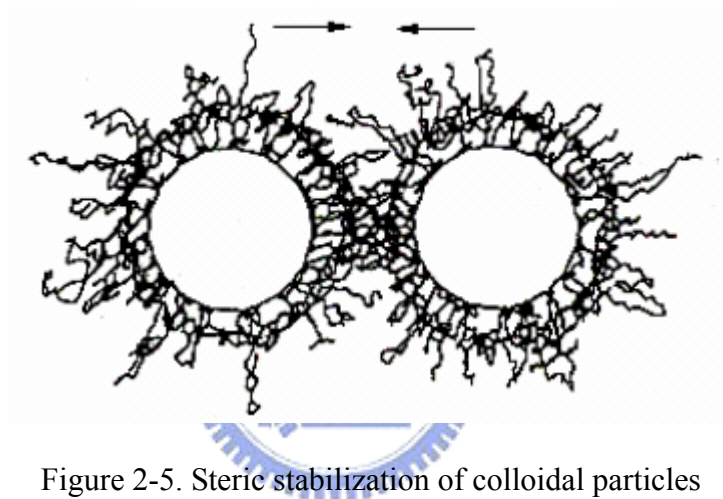
Figure 2-5. Steric stabilization of colloidal particles

(3). Electrosteric Forces

Electrosteric stabilization depicts how polyelectrolyte dispersants are utilized to induce electrostatic and steric repulsions to control colloidal stability. Polyelectrolyte adsorption is remarkably affected by the chemical and physical properties of particle surface. Adsorption is strongly favored when polyelectrolyte species and the colloid surface are oppositely charged. For a given system, the adsorption behavior and conformation of polyelectolytes can be adjusted by pH values and ionic strength of

solution.[13]

For thicker adsorbed layer with extending chains protruding into the solution, the polymeric contribution becomes more significant. For examples, the PDAAE and PMAA, the principal mechanism of stabilization should be electrostatic and steric force. Besides the steric contribution there is always an electrostatic contribution, since the adsorption of highly charged polyelectolytes on a weakly charged particles surface often causes an increase in the net charge density.[23,24]

2.2. The Characteristics of Barium Titanate (BTO)

2.2.1. Surface Chemistry of BTO

It has been reported that when BTO is milled in deionized water, Ba^{2+} ions are leached out from the powder. That would result in a Ti-rich surface. It is also found that the level of Ba^{2+} leaching is dependent upon the pH of solution. The reason for the unfavorable effects is the instability of alkaline earth titanates in water, which has been experimentally observed first on calcium titanate ($CaTiO_3$). The reaction of $BaTiO_3$ in H_2O are

$$BaTiO_3 + 2H^+ \rightarrow Ba^{2+} + TiO_2 + H_2O \qquad (2.3)$$

and

$$BaTiO_3 + H_2O \rightarrow Ba^{2+} + TiO_2 + 2OH^- \qquad (2.4)$$
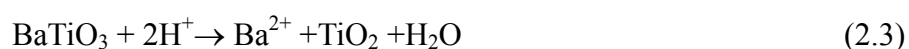
The dissolution of Ba^{2+} ion not only change Ba/Ti ration of particle surface, but also affect the pH value of solution. In the other way, leached Ba^{2+} ions would be reposited on the powder surface during dry period, and result in exaggerated grain growth and sintered density.[23]

2.2.2. The Properties of BTO[25-31]

BTO-based compounds are the most important ferroelectric materials frequently used as capacitor materials for their excellent dielectric properties. The crystal structure of BTO is simple perovskite, so BTO can easily form solid solutions with other oxides. This is the reason why BTO is most widely used in various electronic applications.

BTiO powders are synthesized conventional by solid-state reaction of titanium dioxide (TiO_2) and barium carbonate ($BaCO_3$). After mixing, the powders are calcined in a temperature of 1250 to 1350°C. The reaction can be shown as

$$BaCO_3 + TiO_2 \rightarrow BaTiO_3 + CO_2 \qquad (2.5)$$

The phase diagram in BaO-TiO$_2$ system is shown in Fig. 2-6. BTO is formed

when the stoichiometric ratio of TiO$_2$/BaO was nearly unity. Figure 2-6 also shows

various crystal structures of BTO. Above 1460°C, the structure of BTO is a

non-ferroelectric hexagonal form. The hexagonal phase transforms to cubic phase (*i.e.*,

the perovskite type shown in Fig. 2-7) when temperature is below 1460°C.
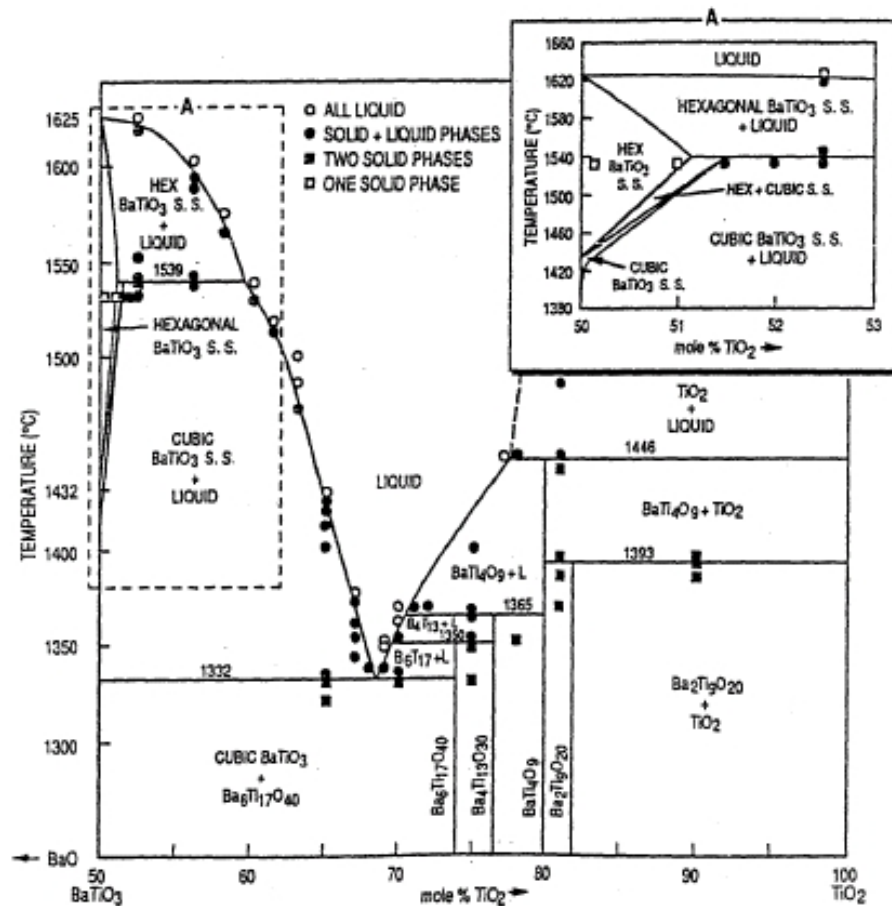
Figure 2-6. BaO-TiO$_2$ binary alloy phase diagram.
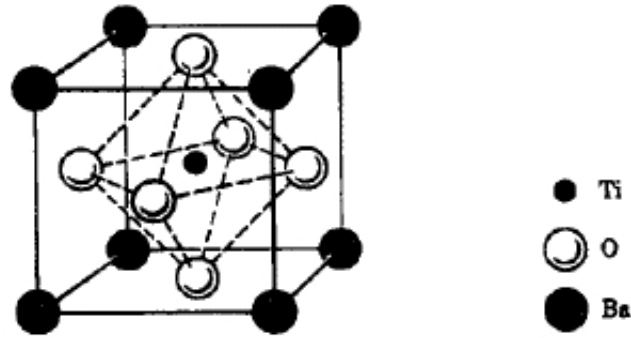
Figure 2-7. Ion position in ideal perovskite structure.

In perovskite BTO, the Ba^{2+} ion with the ionic size about 0.159 nm locates at the

corner site of cubic crystal and Ti^{4+} with the ionic size about 0.061 nm locates at the

body center site of this crystal. The O^{2-} ions located at the face-center site of the

crystal and are octahedron formed to surround the Ti^{4+}.[25-28]

The cubic crystal is one of symmetrical paraelectric materials, and has no

behavior of spontaneous polarization. Below 130°C, the perovskite-type structure

elongates along the plane (001). This temperature of phase transformation is termed

as Curie temperature (T_C). The cell of tetragonal phase with the lattice constant c

larger than a is formed as shown in Fig. 2-8. The Ti^{4+} ion was deviation from the

center of the crystal, and dielectric dipole is formed in the crystal.[29,30]

Upon further cooling, another two polymorphic transitions occur at 0°C and

−90°C. The orthorhombic phase with elongation along a body diagonal is formed at

0°C and the rhombohedral phase with elongation along a body diagonal is formed at

−90°C as shown in Fig. 2-9. In each temperature range, the direction of ferroelectric

dipole parallels the elongation of the unite cell. The relationship of dielectric constant

versus temperature is given in Fig. 2-10.
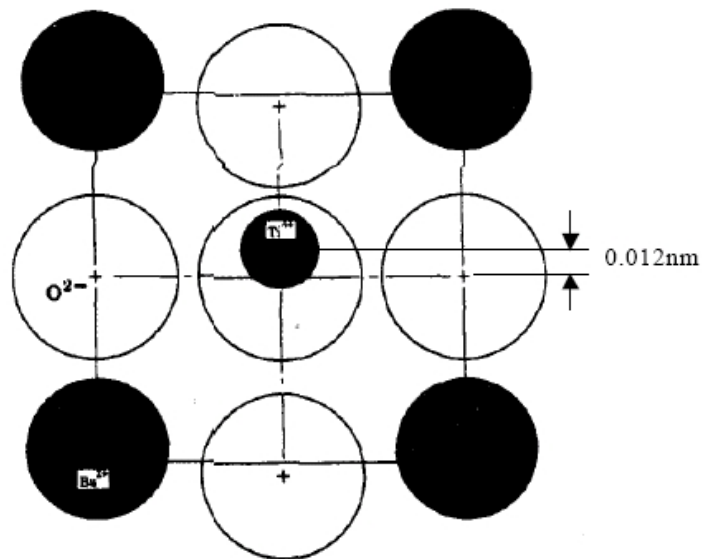
Figure 2-8. Ion position in tetragonal BTO.
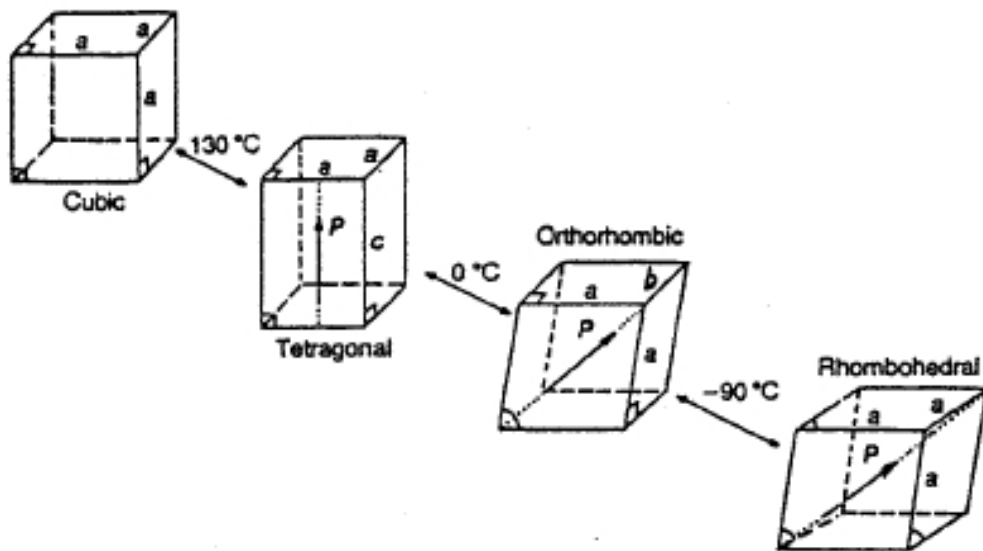
Figure 2-9. Structural variation of BTO unit cell.
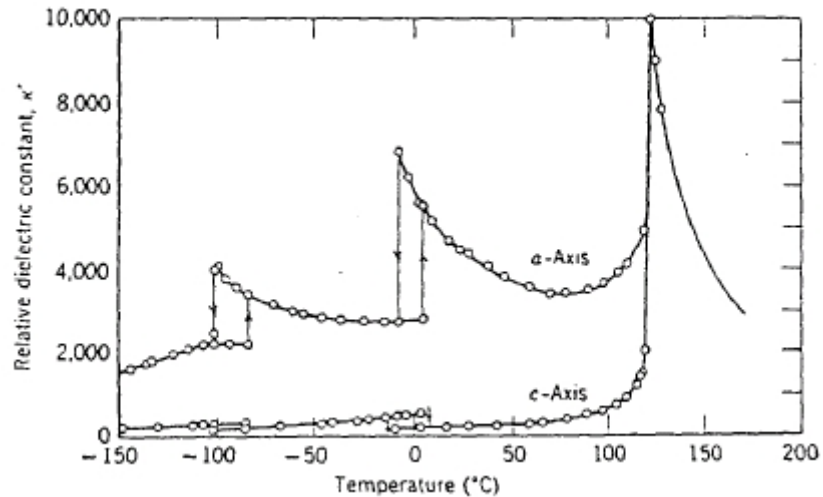
Figure 2-10. Temperature dependence dielectric constant.

The interface between domain and domain is called "domain wall" or "domain boundary". As the differential of polarization between domains is 180°, the domains are termed the 180° domains; whereas, the differential of polarization is 90°, the domains are termed the 90° domains. The domain structure is illustrated in Fig. 2-11. The 90° domains of BTO exhibit a lamellae shape varied from micro thickness.[28]

Due to phase transformation of BTO takes place during cooling through T_C, the crystal structure transforms from cubic crystal into tetragonal one, leading to the increase of c and decrease of a lattice constant. The change of lattice constant may produce stress within the structure. In single crystal, the stress can be released without any stress concentration by free surface. Whereas, for polycrystalline BTO, the transformation tends to be retarded due to the compact structure and anisotropy of grains, the internal stress is thus formed. The internal stress is released by the

17

formation of 90° domains.[31]
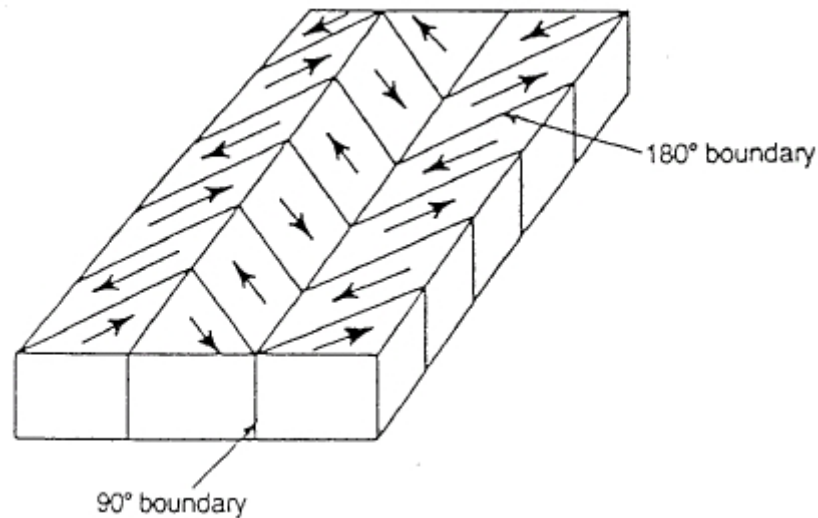
Figure 2-11. Schematic illustration of domain structure.

2.2.3. The Sintering Behavior of BTO[32-41]

The solid sintering process can be divided into the initial stage, the intermediate

stage and the final stage as illustrated in Figure 2-12. The green body can be treated as

loose powders bonded by polymeric binder. In the initial stage: the powders start to

combine with each other in order to reduce the total surface free energy. As the area

of intimate contact between powders dramatically increases and the intra-particle

holes start to round-up, the sintering process would step into the intermediate stage. In

this stage, there are open holes which allow the flow out of gas from the interior to

exterior of sintered body. This also eliminates the solid-gas interfaces and thus

promotes the densification. In this stage, diffusion would dominate the atom

movement so as to induce the lattice rearrangement aw well as the grain growth. In

final stage of sintering, the open holes nearly diminish; their diminution eliminates the

barrier of gain growth and thus grain coarsening becomes obvious.
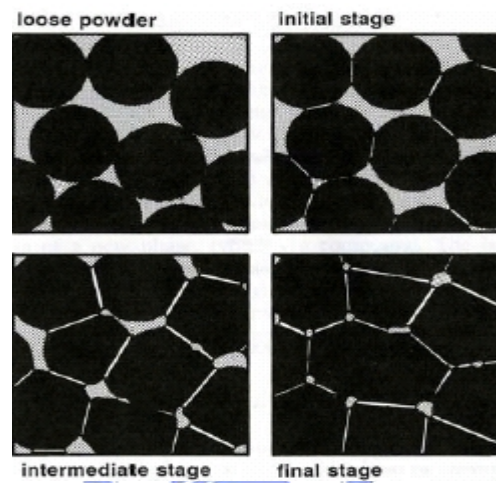
Figure 2-12. Structure evolution of sintering process.

The co-existence of abnormal grain growth and increase of densification in BTO

was first reported by Xue et al.[32] However, most reports pointed out that pores are

easily trapped into abnormal grain.

Schmelz proposed that a solid-state diffusion controlled mechanism is dominated

in initial shrinkage of BTO as the temperature is 1000°C below the eutectic

temperature (at 1250°C).[33] On the other hand, Enomoto et al. and Xue suggested that

grain boundary diffusion mechanism is the main controlling mechanism for the

sintering of BTO.[34,35]

As sintering proceeds, the dominant mechanism is under investigation for many years. Anderson suggested that the species dominating the diffusion is oxygen vacancy in the initial stage of sintering of BTO by the analysis of sintering kinetics.[36] The result was also supported by Nowontny et al.[37]

Various fluxes are added in electric ceramics to promote the sintering rate. The addition of fluxes, such as LiF and 4PbO-B_2O_3 can lower the sintering temperature to yield dense BTO.[38,39]

Most of the studies relating to sintering of BTO concentrated on the liquid-phase sintering.[40] Nevertheless, liquid-phase sintering may cause the abnormal grain growth and consequently low the relative permittivity. The amount of liquid phase, the solubility of solid phase in liquid, good wetting and grain size of BTO are important as far as good electrical properties are concerned.[41]

2.2.4. The Electrical Properties of BTO

An enhancement of the dielectric constant (ε_r), for fine grain ($\approx$ 1 μm) BTO ceramics below T_C, was reported as early as 1981.[34] When BTO ceramics are prepared with a grain size as small as 0.5- 1 μm, the ε_r values below T_C, become significantly enhanced, e.g., $\varepsilon_r \approx$ 5000 for fine grain (0.5 μm) material, compared with

$\varepsilon_r \approx 1500$ for coarse grain (50 μm) ceramics at room temperature. The effect is clearly illustrated in the data reported by Enomoto and Yamaji, as shown in Fig. 2-13.[34] The value of 5000 for fine-grain microstructures was suggested by Buessem *et al.,* and Martirena *et al.*[42,43] These authors ascribed the high relative permittivity observed in the fine grained BTO to of high internal stress in fine-grained BTO. No 90° domains can exist in fine-grained BTO whose grain size is smaller than 1 μm. The internal stress of fine-grained BTO is increased when the lattice is distorted below Curie temperature. It is due to the absence of stress relaxation by the formation of 90° domains as normally shown in coarse grains.[42,43] With further reduction in grain size below 0.5 to 1.0 μm, the ε_r value in the tetragonal phase was observed to decrease again. This behavior is illustrated in the data reported by Arlt *et al.*[44] Due to practical difficulties in preparing dense BTO ceramics with a grain size less than 0.5 μm, little data has been reported for ε_r values below that grain size. Most importantly, a rigorous explanation of the effect has remained elusive. Arlt *et al.,* proposed that the decrease in ε_r resulted from changes in crystal structure (*i.e.*, a "pseudocubic" structure, not tetragonal structure) with grain size reduction.

The electric properties of BTO depend highly on its microstructure. For the commercial BTO dielectrics, doping with various elements to tailor the dielectrics properties is commonly seen. The types of additives methods include isovalence

substitution, donor doping, and acceptor doping.
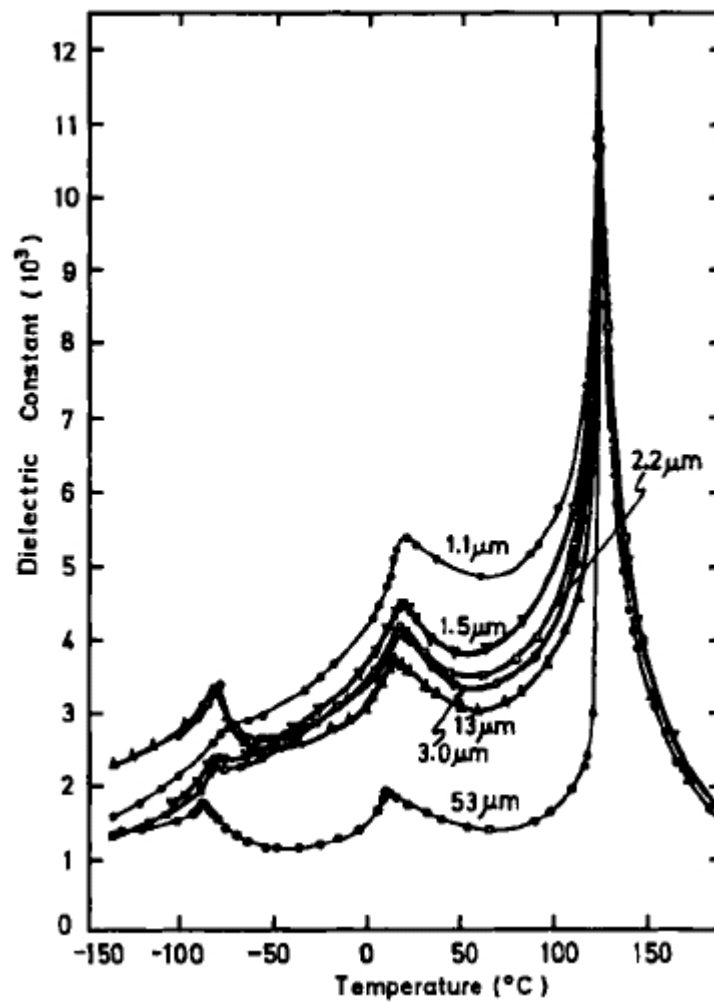
Figure 2-13. Effect of grain size on measured values of dielectric constant for BTO

ceramics with grain sizes ranging from 1-50 μm.

The ion that has the similar ionic radius as Ba^{2+} or Ti^{4+} or has same valence as

Ba^{2+} or Ti^{4+} can easily substitute the site of Ba^{2+} or Ti^{4+} in BTO lattice. The frequent

isovalence substitutions are Pb^{2+}, Ca^{2+}, Sr^{2+}, *et al.* for replacing Ba^{2+}; Zr^{4+}, Sn^{4+}, Hf^{4+},

et al. for replacing Ti^{4+}. If the effect of dopants can change the T_C, the dopants are named the shifter of T_C, *e.g.*, the Sr^{2+} and Pb^{2+} shown in Fig. 2-14. On the other hand, extending the temperature range of usage is also important. For the modification of BTO-based capacitors in a wider temperature range, Zr^{4+}, and Hf^{4+} are usually added to modify the dielectric coefficient with temperature. Another type of dopants that are useful in formulating BTO dielectric are know as Curie-peak broadeners.[41-45]

Donor doping is the doping of excess-valance ions in order to replace the metal ions in the lattice. For instance, Nd^{3+} and La^{3+} replace Ba^{2+}; Nb^{5+} and Ta^{5+} replace Ti^{4+}. However, doping with low level of donors may lead to the inhibitions of grain growth of BTO.[46,47]
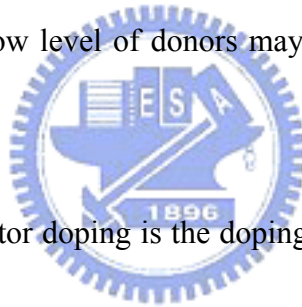
On the other hand, acceptor doping is the doping of less valence ions in order to replace the metallic ions in the lattice. Most of the previous studies reported about the substitution of Ti^{4+}. For example, Mn^{2+} or Mn^{3+}, Co^{2+} or Co^{3+}, and Ni^{2+} replace Ti^{4+}. After the equilibrium of the substitution, the oxygen vacancies are formed. The vacancies will induce the electrolytic migration of the O^{2-} in the direct current field. It reduces the resistance and the dissipation factor of BTO, the dielectric properties increases.[48-50] At last, the dopants that may replace the site of A or B in ABO$_3$ structure are summarized in Table 2-1.
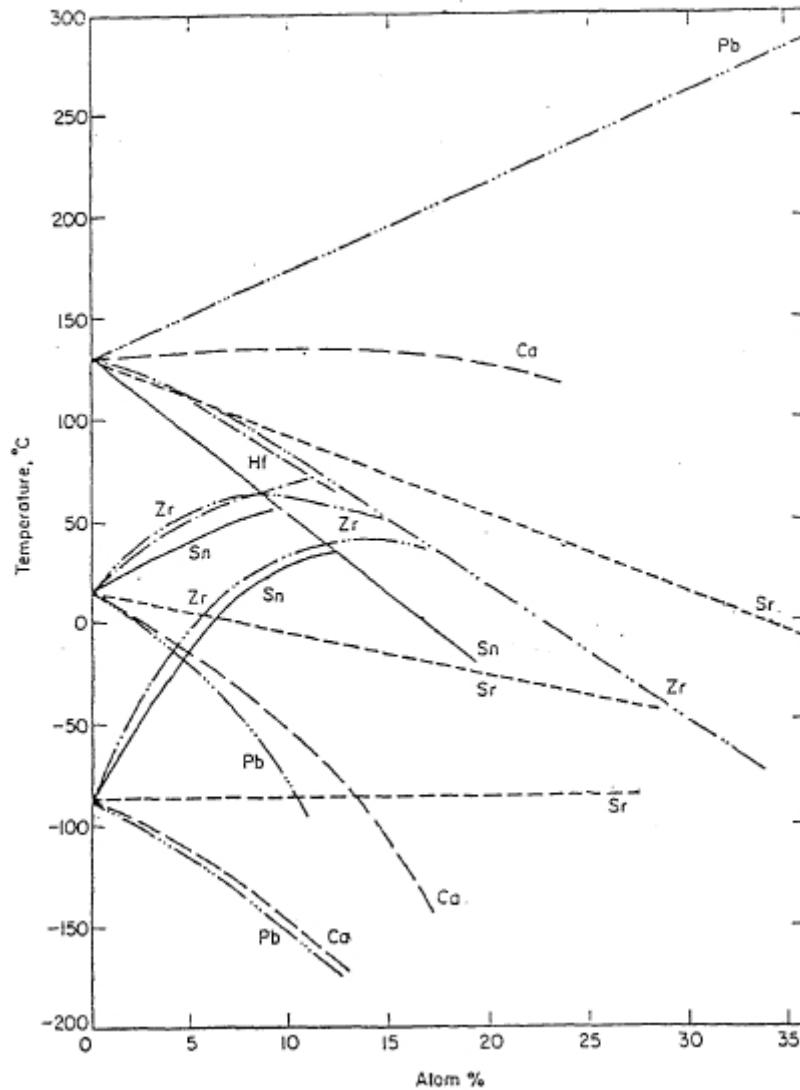
Figure 2-14. Effect of isovalent substitution on T_C of BTO composition.

2-3. Introduction to LIBs

During the pass two decades, LIBs are extensively studied due to their practical

applications in various fields. Among those attempts, great efforts have been made to

improve their capacity and cycle life in order to develop portable LIBs with the

desirable performance characteristics such as high capacity, long cycle life and high

Table 2-1. Ionic radius and dopants to replace sites in ABO_3.

Dopant	Ionic radius (nm)	Replace site		Replace method		
		A-site	B-site	Donor	Acceptor	Isovalent
Y	0.121	●		●		
Yb	0.118	●		●		
Bi	0.131	●		●		
Er	0.120	●		●		
Ho	0.126	●		●		
Pb	0.163	●				●
Ce	0.128	●		●		
Dy	0.123	●		●		
La	0.116	●		●		
Al	0.675		●		●	
Nb	0.086		●	●		
Zr	0.086		●			●
Nd	0.141	●		●		
Mg	0.086		●		●	
Mn	0.081		●		●	
Sn	0.090		●			●
Co	0.083		●		●	

(Ionic radii: Ba^{2+} = 0.136 nm; Ti^{4+} = 0.061 nm; O^{2-} = 0.126 nm)

discharge-rate capability. LIBs comprise of cells using positive and negative materials capable of intercalating Li ions. As the battery is cycled, Li ions exchange between the positive and negative electrodes. Lithium metal has several unique properties including it is light and it has a large negative electrode potential (−3.04 V *versus* standard hydrogen electrode), which gives the LIB a high energy density and working voltage compared to, for example, a nickel-metal hydride battery. In LIBs, lithium ions are employed as "energy carries" and move from the anode across the

electrolyte to the cathode during battery discharge and *vice versa* as the battery is recharged. The working principle of LIB is based on the intercalation of Li ion in the active materials as shown in Fig. 2-14.[51] In the LIB, the cathode generally contains lithium metal oxides (*e.g.*, $LiCoO_2$, $LiNiO_2$ or $LiMnO_2$) and normally serves as the Li sources. During the first charge process, Li ions de-intercalated from the cathode were again intercalated into the carbonaceous anode and the process is reversed as in the discharge process. Therefore, Li ions are shifted between two electrodes during the charge-discharge process. The battery, as prepared, is in a discharged state, where Li ions are contained within the cathode active materials. During the charge cycle, an external current is applied to the battery that leads the Li ions move through the separator (with the aid of an electrolyte which is a conductor of lithium ions) to the anode side, where contains graphite particles capable of intercalating lithium ions and remains ready for the discharge cycle when an external load is connected to the battery. The charge/discharge total reactions and the anode reaction based on Li^+ intercalation and deintercalation are show as below:

$$LiCoO_2 + yC \underset{discharge}{\overset{charge}{\rightleftharpoons}} Li_{1-x}CoO_2 + Li_xC_y$$

$$yC + xLi + xe^- \underset{discharge}{\overset{charge}{\rightleftharpoons}} Li_xC_y$$

(2-6)
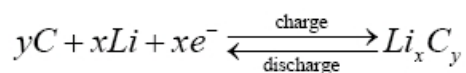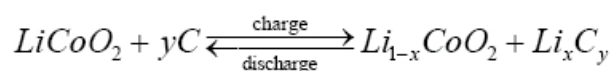
26
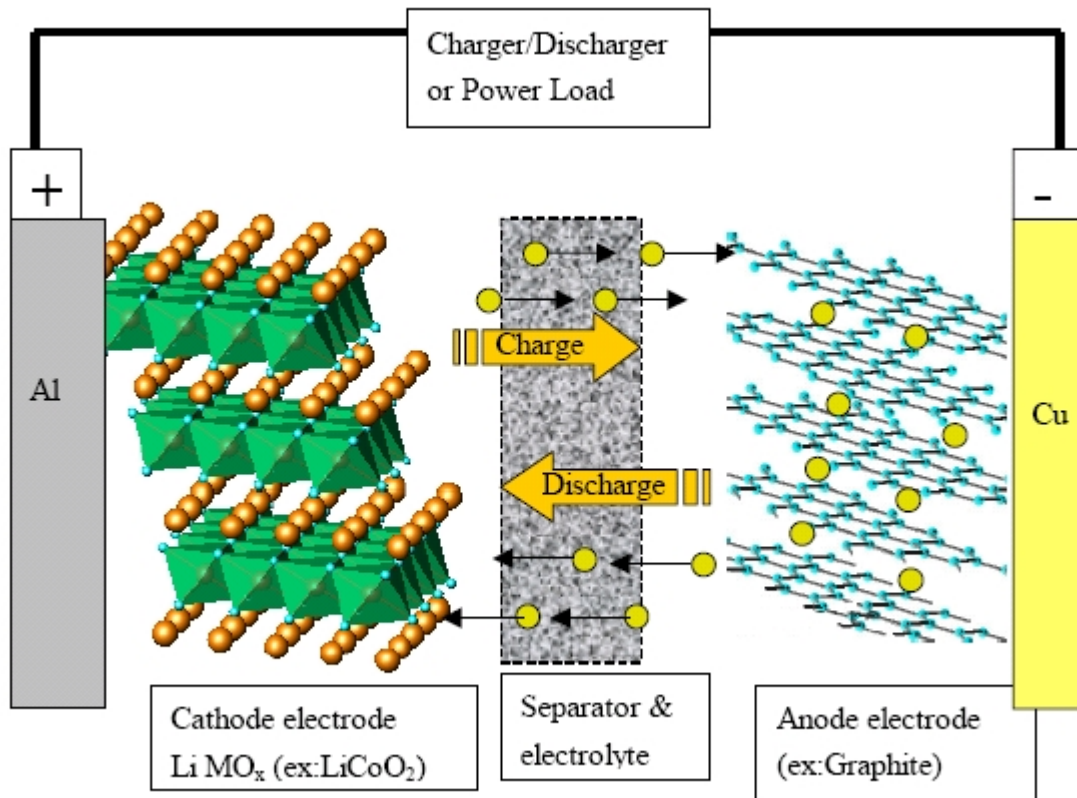
Figure 2-15. Schematic illustration of LIBs.
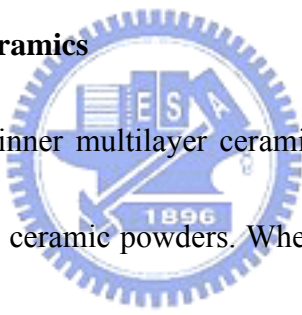
2-4. CNT-based Anode in LIBs

CNT has a relatively high mechanical strength and electrical conductivity. CNTs are graphitized carbon fibers and have high length/diameter ration, so they have high conductivity and tend to form special network-like morphology by nature.[52,53] CNTs have been characterized in terms of the highly preferred orientation of their graphitic basal planes parallel to the fiber axis, with an annular ring texture in the cross section. This structure gives rise to excellent mechanical properties, very high electrical and thermal conductivity, and a high graphitizability. In order to improve the conductivity

and adhesion of the composite cathode during bending, CNT was added to form a network-like composite electrode. The interconnected structure not only provides high conductivity but also binds all other compositions together. Electrochemical performances of the thin and flexible batteries with carbon-nanofiber composite cathodes were investigated in terms of life-cycle stability, high-current discharge behavior, and lowtemperature discharge performance.

2.5. Motivations

2.5.1. Nano BTO-relating Ceramics

Recent development of thinner multilayer ceramic capacitors (MLCC) demands the usage of smaller-sized raw ceramic powders. When the thickness of an individual layer in MLCC is scaled down to 2 μm, nano-meter scale ceramic powders are required in order to produce the defect-free layers. From our previous studies, to achieve a high packing density and uniform microstructure in green tape, slurry with fine dispersion is essential. However, dispersion of ceramic powders in nanometer scale is a difficult issue in comparison with the powders in micrometer scale since the nano-scale powders exhibit a larger SSA and van der Waals attractive force.

So far, the dispersive research about nano ceramic is still unclear. In our study, we disperse the nano powder in order to eliminate the agglomeration caused by van der

Waals attraction resulted from large SSA of nano-sized particles before using. Furthermore, the effects of grain size on the dielectric properties of electroceramics is also one of important research topics in electronic ceramics. This work studied the dispersion and sintering behaviors of nanometer-scale BTO, BST and BST material doping with La_2O_3 powders at nanometer scale in order to obtain the desired dielectric properties. The densification process at different sintering temperatures and time spans as well as the relationships between grain sizes, crystallization behaviors, microstructure changes and dielectric properties of BTO-relating capacitors based on such nano-scale ceramic powders were investigated.
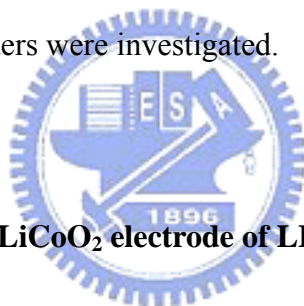
2.5.2. Dispersion of CNTs in $LiCoO_2$ electrode of LIBs

In 1990, the LIBs were commercialized by Sony Energytech. Owing to the need of small power source with high energy density and long cycle life for portable devices, the lithium-ion batteries have been used popularly for 3C products. The lithium metal oxides $LiMO_2$ (M = Co, Ni and NiCo) have been used as cathode materials for lithium-ion batteries. However, the powder conductivities are poor for the pure lithium metal oxides. Various conductive materials such as carbon black, graphite, carbon fiber and CNT are used to improve the conductivity of positive electrode.

CNT is an alternative of conductive agent in LIB electrode due to its relatively high mechanical strength and electrical conductivity as well as the nature of forming a network-like morphology. However, in most cases, the CNTs aggregates seriously like tied hair and its aggregates do not break up during the ball mixing process. Up to now, study relating to dispersion of CNT is still missing. This work demonstrates the dispersion method of CNTs and its applicability to the performance improvement of LIBs.

CHAPTER 3

Experimental Methods

3.1. Dispersion and Preparation of Nano-ceramic Powders

3.1.1. Raw Materials

(1) **BTO samples**: High purity, amorphous BTO powder (Seedchem, Australia, Purity

≈ 99.95) with Ba/Ti = 0.915, average size = 100 nm, and specific area = 9.18 m^2/g

was utilized as the raw material of experiment.

(2) **BST samples**: The BTO ($Ba_{0.7}Sr_{0.3}TiO_3$) specimens were synthesized based on the

commercial BTO and $SrTiO_3$ (STO) powders supplied by Ferro Corp., Penn Yan,

NY, USA, and fabricated *via* the solid-state reaction process.[54] According to the

supplier's data, the purities and average sizes of BTO and STO were both 99.9%

and about 100 nm. The crystal structures of BTO and STO are both cubic. The

chemical dispersant for nano-ceramic powders, PDAAE, was prepared from

acrylamide and (α-N, N-dimethyl-N-acryloyloxyethyl) ammonium ethanate

(DAAE) *via* the free-radical polymerization and the detailed preparation

procedures of PDAAE could be found elsewhere.[55] Powder slurries were prepared

by mixing the BTO and STO powders at fixed molar ratio of 7:3 and then

grinding with appropriate amount of PDAAE chemical dispersant in a laboratory

mill (MiniZeta 03, NETZSCH-Feinmahlte chnik GmbH, see Fig. 3-1) for

appropriate time spans.

1 Support   4 Lever   7 Product outlet

2 Grinding tank   5 Collecting vessel 8 Mixer
                 (special accessory)

3 Fitting pin   6 Tank floor

                 9 Ventilating plug
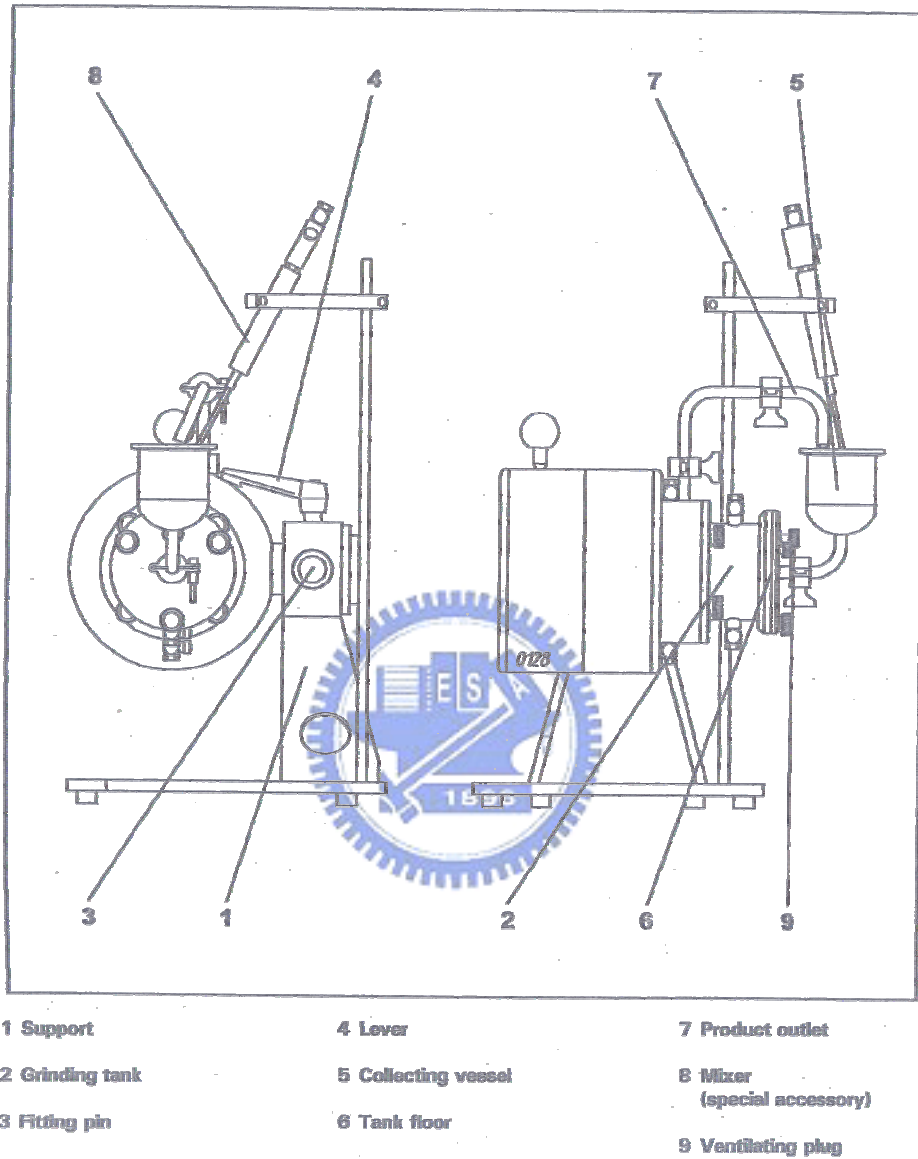
Figure 3-1. The structure of MiniZeta 03 laboratory mill.

(3) **La-doped BST samples**: Commercially available BTO, STO (Ferro Co., Penn

Yan, NY, USA) and La_2O_3 (99.99%, Genesis Nanotech Co., Taiwan) powders

were adopted as the starting materials. Powder slurries were prepared by mixing

the BTO and STO powders at fixed molar ratio of 7:3 and then grinding with 5 *wt.*% of PDAAE chemical dispersant in the MiniZeta 03 laboratory mill at the speed of 1800 rpm for 30 min. Afterward, 0.5, 1.0 and 1.5 *mol.*% (0.74, 1.48 or 2.22 *wt.*%) of La_2O_3 was added in to the BTO/STO mixture with PMAA chemical dispersant further grounded in the laboratory mill at 2400 rpm for 20 min to form the slurry containing the ceramic powders of average size = 70 nm. Hereafter, the capacitor samples fabricated based on such a powder sulrry are termed as *x*LBST in which *x* denotes the dopant concentration in *mol.*% as cited above.

3.1.2. Chemical Dispersants

(1) **PMAA-Na**: PMAA-Na is a kind of anionic dispersant used to disperse ceramic powders. The anionic function group is COO^-. The detail data of PMAA-Na is listed in Table 3-1.

(2) **PDAAE**: An amphibious dispersant was adapted. There are two kinds of function groups. The anionic function group is COO^-, same as PMAA-Na. The cationic function group is N^+. The detail data of PDAAE is also listed in Table 3-1.

Table 3-1. Properties of chemical dispersants.

	PDAAE	PMAA-Na
Chemical	polyacrylamide/(α-N, N-dimethyl-N-acryloyloxyethyl) ammonium ethanate	Sodium salt of poly(methacrylic acid)
Formula	Show as below	
Function group	$-$COONa and N$^+$	$-$COONa
Outlook	Citrine liquid	Yellow liquid
Molecular weight (g/m)	1×10^5	1.3×10^4
Solution loading (mass %)	13%	16%

Chemical formula of PMAA-Na:
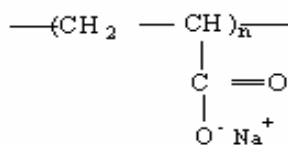
Chemical formula of PDAAE:
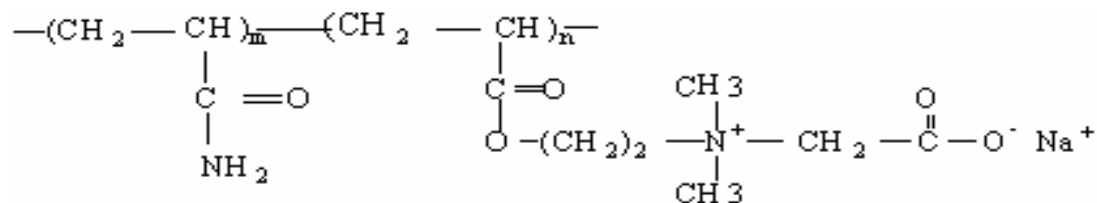
3.1.3. The Experimental Flow

The experimental flows for this study are shown in Figs. 3-2 to 3.4. The experimental procedures are adjusted according to the difference of starting materials.
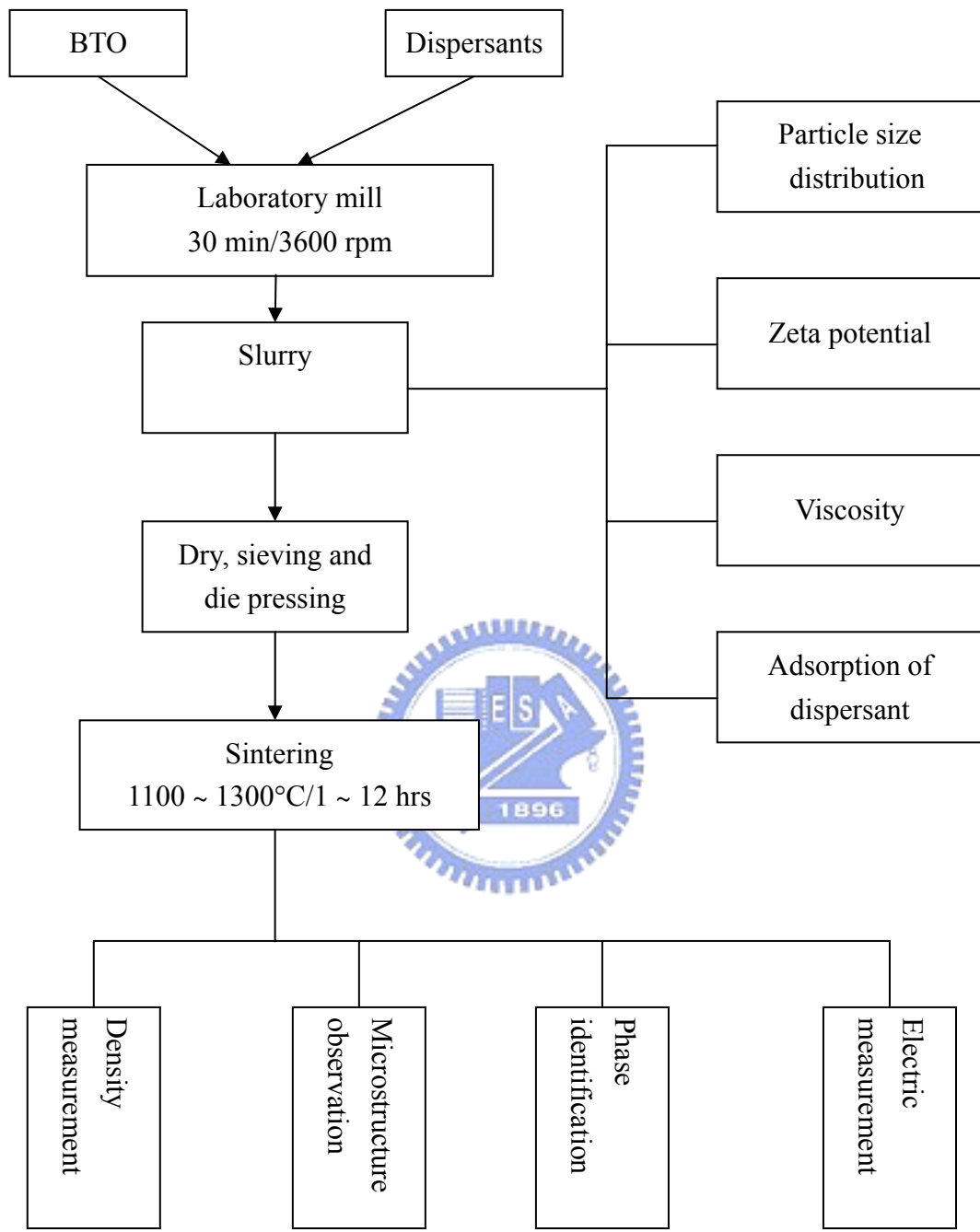
Figure 3-2. Experimental flow of BTO specimens.

```
┌──────────┐      ┌──────────┐      ┌──────────────┐
│   BTO    │      │   STO    │      │  Dispersants │
└──────────┘      └──────────┘      └──────────────┘
      \                │                   /
       \               │                  /
        \              ▼                 /
      ┌──────────────────────────────┐
      │      Laboratory mill         │
      │      30 min/3600 rpm         │
      └──────────────────────────────┘
                    │
                    ▼                          ┌──────────────────┐
      ┌──────────────────┐                     │  Particle size   │
      │                  │─────────────────────│  distribution    │
      │     Slurry       │              │      └──────────────────┘
      │                  │─────────────┐│      ┌──────────────────┐
      └──────────────────┘             ││      │                  │
                    │                  └───────│    Viscosity     │
                    ▼                          │                  │
      ┌──────────────────┐                     └──────────────────┘
      │  Dry, sieving and│
      │   die pressing   │
      └──────────────────┘
                    │
                    ▼
      ┌──────────────────────────────┐
      │         Sintering            │
      │     800 ~1400°C/1 ~ 12 hrs    │
      └──────────────────────────────┘
```
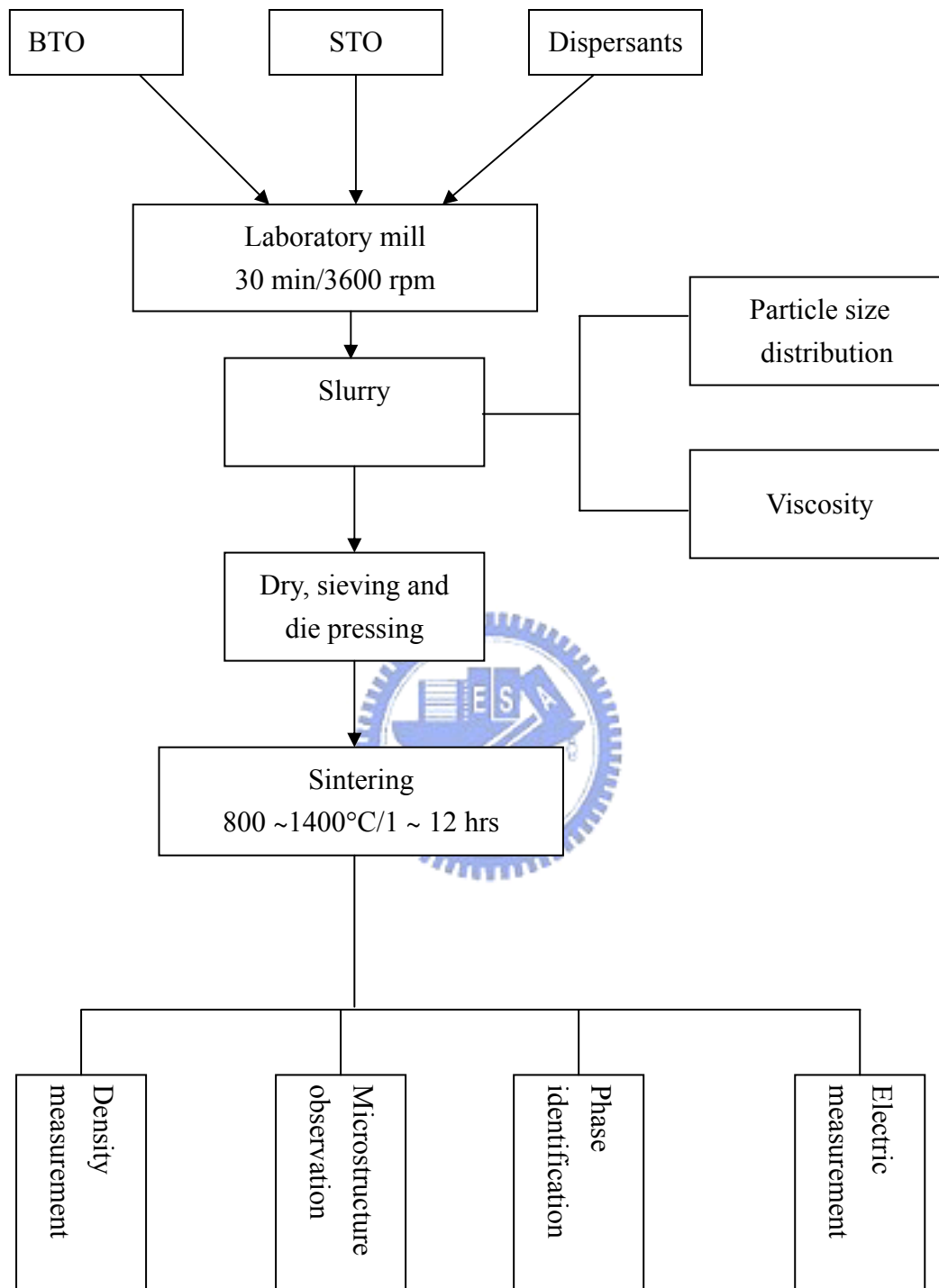
Figure 3-3. Experimental flow of BST specimens.
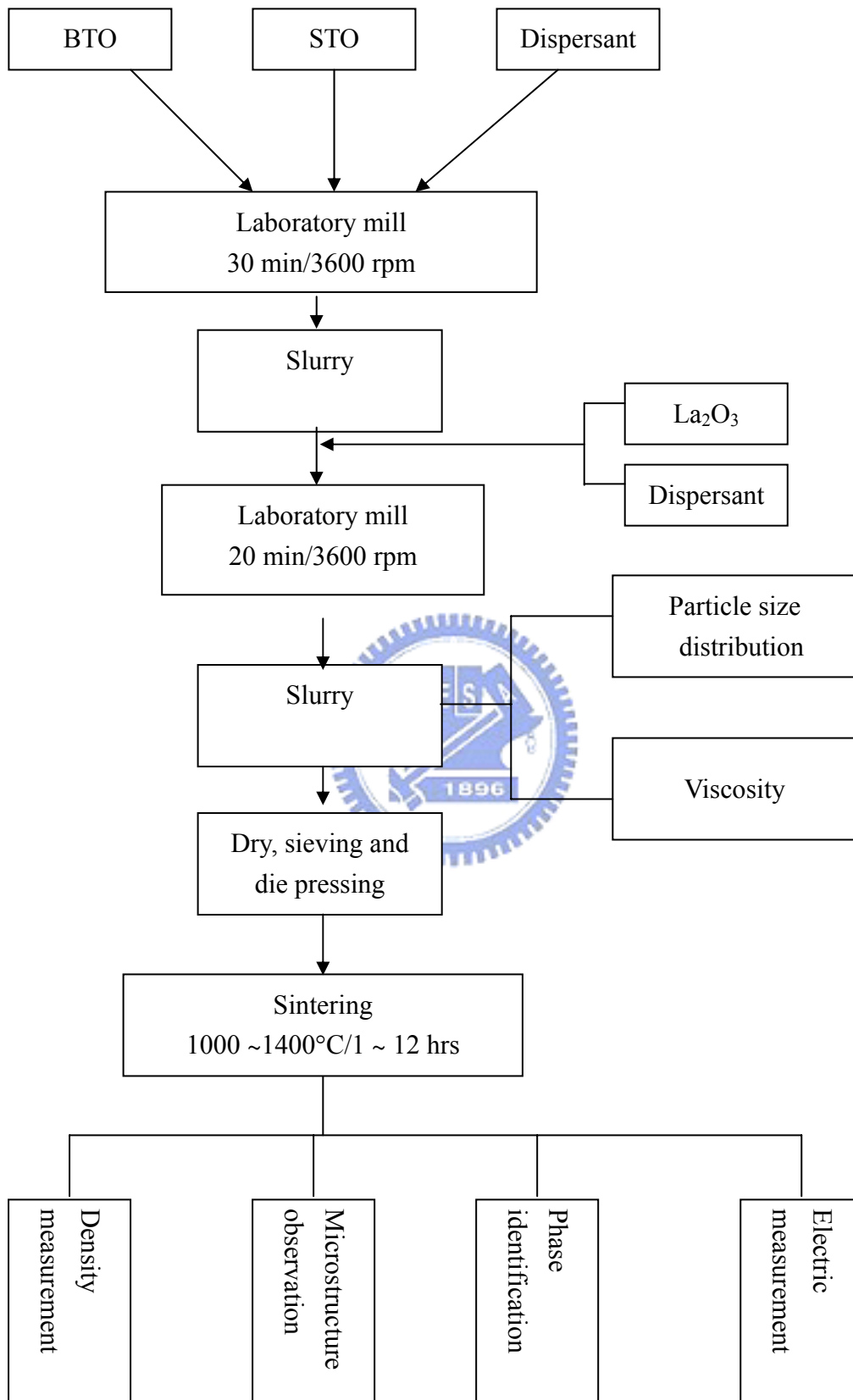
Figure 3-4. Experimental flow of La-doped BST specimens.

3.2. Characterizations of Aqueous Slurries

3.2.1. Particle Size Distribution

Different amounts of PMAA-Na and PDAAE dispersants based on the weight of ceramic powder were added into deionized water and the pH value of solutions were adjusted to 9.5 by adding appropriate amounts of $NH_4OH_{(aq)}$. The purpose of this procedure is to ensure the complete dissociation of chemical dispersants.[55] The nano BTO powder, BST or xLBST mixtures was added. After mechanical grinding/mixing by the MiniZeta 03 laboratory mill, a small amount of slurry was taken out and sent to a particle size analyzer (Malvern Mastersizer 2000, UK) for the examination of the size distribution of powders in the slurry.

3.2.2. Zeta potential

After mechanical milling, a small amount of supernatant was removed from slurries by centrifugation, and zeta potential of the remaining powders in the supernatant was then measured by using a zeta meter (PEN KEN Inc. 501, France).

3.2.3. Viscosity

The viscosity of 60 *wt*.% ceramics suspensions with or without chemical dispersants subjected to mechanical grinding/mixing process *via* a laboratory mill was

evaluated by a viscometer (Brookfield DV-II, USA) at a rotation speed of 0- 60 rpm.

3.2.4. Adsorption of Dispersant

BTO aqueous suspensions of 30 *wt*.% with different concentrations of either PDAAE or PMAA-Na were prepared at pH=9.5. These suspensions were deagglomerated by a laboratory mill. After laboratory milled, the suspensions were centrifuged at a speed of 6×10^3 rpm for 30 min to obtain supernatants. The residual dispersant concentration in the supernatants was analyzed and determined by a titration procedure mentioned above. The amount of dispersant adsorbed on ceramics was calculated from the difference in dispersant concentration before and after adsorption.
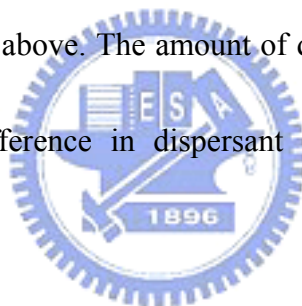
3.3. Characterizations of Sintered Samples

3.3.1. Density Measurement

The density of the samples was measured by the Archimedes method. At first, the samples were bake at 150°C for 1 hr. The dry-weight W_1 of it is weighted out with an electronic balance. Sample was then immersed in de-ionized water and heated at 100°C for 30 min with a hot plate. The samples were taken off and laid on a dry tissue to remove the moisture on the samples. The wet-weight of the sample W_3 was

obtained. Then, the samples was hung with a small net and put in a glass of DI water

in order to measure the floating weight W_2. The density D of the sample is obtained

by

$$D = D' \frac{W_1}{W_3 - W_2} \qquad (3\text{-}1)$$

where D' is the density of the de-ionized water.

3.3.2. Microstructure

Grain sizes, morphology and element distribution of sintered bodies were

examined by scanning electron microscopy (SEM, Hitachi 4700) and transmission

electron microscope (TEM, Philips, Tecnai 20, G-2) attached with energy dispersive

spectroscopy (EDS, STUW 3.3). The average grain size was obtained by SEM and the

intercept method.[43]
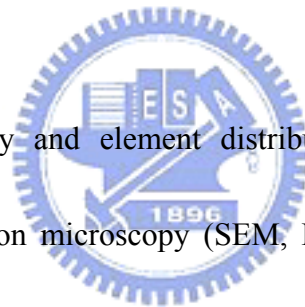
3.3.3. The Phase Identification of Materials

X-ray diffraction (XRD) was performed by using a diffractometer (Siemens

D5000) within Cu-K_α radiation (λ = 0.1542 nm) at the scanning rate of 1°/min in

order to identify the phase constitution of samples.

3.3.4. Dielectrical Properties

The indium-contained silver paste was adopted as the electrode material to provide Ohmic contact. The dielectric properties of sintered body were measured by a HP 4194A impedance analyzer at 1 kHz. Before the measurement was carried out, calibration must be done. With the capacitance of the sample measured, the real part of the relative dielectric constant ε_r was calculated as follows:

$$\varepsilon_r = \frac{Cd}{\varepsilon_o A} \qquad\qquad (3\text{-}2)$$

where C is the capacitance, d is the thickness, A is the area and $\varepsilon_0 = 8.8542\times10^{-12}$ F/m.

3.4. Dispersion of CNTs

3.4.1. Synthesize of PEI

(1) **Materials:** NMP (Aldrich, 99.99%) and N,N-dimethyl -formamide (DMF) (Aldrich, 99.99%) were distilled over CaH$_2$ (Aldrich, 99.95%) under reduced pressure. Pyridine (Aldrich, 99.99%) was dried by distillation after being refluxed with KOH (Aldrich, 99.99%). 4-[Di(4-aminophenyl)-methyl]phenol (Lancaster, 99.99%) was recrystallized from MeOH (Aldrich, 99.99%). Triphenyl phosphate

(TPP) (Aldrich, 99.99%) was purified by distillation under reduced pressure. All other reagents and solvents were used as received from venders unless otherwise stated.

(2) **4-{4-[Di(-aminophenyl)methyl]phenoxy}phthalonitrile (1)**: A mixture of 4-[Di(4-aminophenyl)-methyl]phenol (5 g, 26.96 mmol), 4-nitrophthalonitrile (4.65 g, 26.9 mmol), K_2CO_3 (5 g, 36.2 mmol) (Aldrich, 99.99%), and DMF (20 ml) was heated at 130°C for 4 hrs. After the heating period, the reaction mixture was cooled and poured into by filtration, dried under vacuum and purified *via* recrystallization from ethyl acetate to yield compound **1** (8.2 g, yield ratio ≈ 85 %).
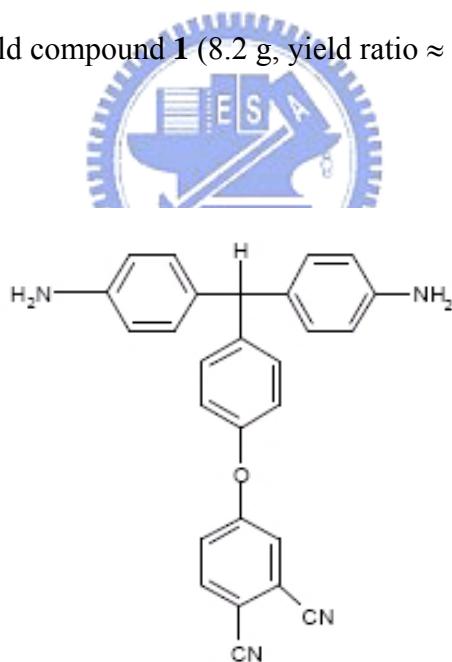
(1)

(3) **4-{4-[Di(-aminophenyl)methyl]phenoxy}phthalic acid (2)**: Solution of KOH (14 g, 0.25 mmol) in a mixture of water-ethanol (100 ml/ 80 ml) was added into

compound **1** (8 g, 28.3 mmol). The mixture was then refluxed for 4 hrs. The resulted

solution was diluted with water (250 ml) and acidified with 6 N HCl(*aq*) to pH ≈ 1.

The precipitate was filtered, washed thoroughly with water, and dried to give

compound **2** (7 g, yield ratio ≈ 88 %).

(2)
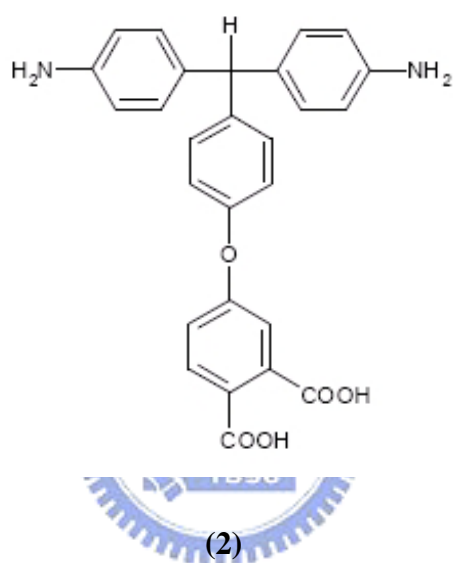
(4) **4-{4-[Di(-aminophenyl)methyl]phenoxy}phthalic Anhydride (3)**: A mixture of

compound **2** (6 g, 17.3 mmol), acetic anhydride (6 ml), and acetic acid (6 ml) was

stirred under reflux for 6 hrs. After cooling, the precipitate was collected by filtration,

washed with a small amount of glacial acetic acid, and then dried in vacuum at 130°C

for 12 hrs to yield compound **3** (4.85 g, yield ratio ≈ 80 %).
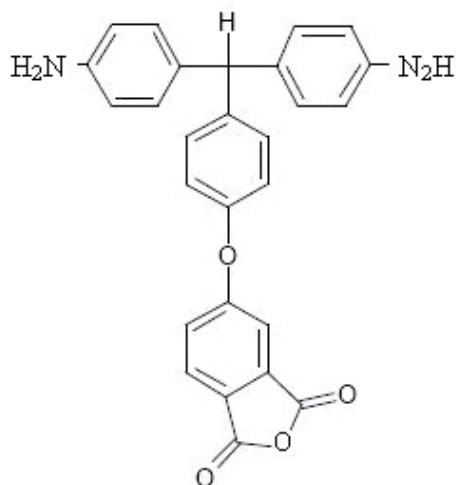
(3)

(5) **PEI**: A solution of compound **3** (3 g, 2.61 mmol), TPP (1 ml, 5.2 mmol), and LiCl (160 mg, 5.77 mmol) in NMP/pyridine (50 ml, 4:1 v/v) was heated at 120°C in nitrogen ambient for 4 hrs. After cooling, the resulted polymer was precipitated in methanol. The polymer was collected, washed with hot water, purified by reprecipitation from DMF into methanol twice and dried in vacuum to produce PEI (2.32 g, yield ratio ≈ 70 %). The chemical reaction was showed in Scheme 3-1 and 3-2. The chemical structure of PEI shown in Fig. 3-5 was identified by ^{1}H-NMR (Varian Unity-300 MHz) and FTIR (Nicolet 360).
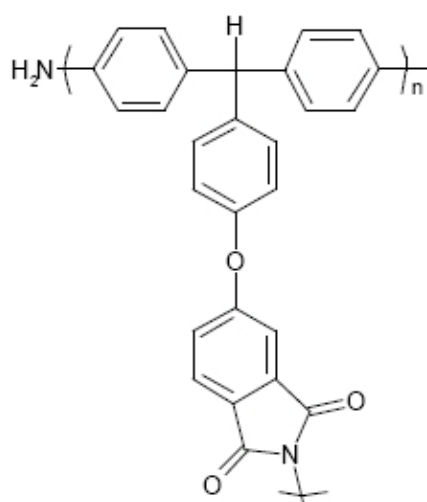
Figure 3-5. Chemical Structure of PEI.
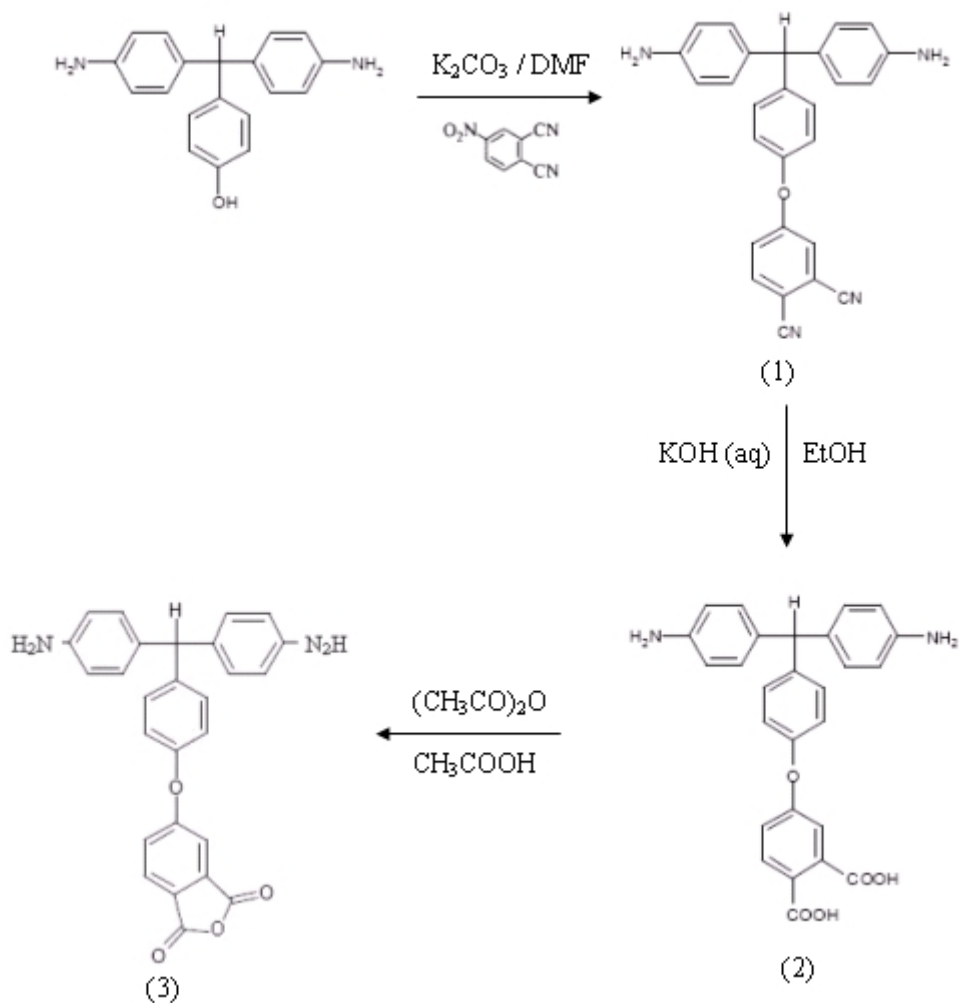
Scheme 3-1
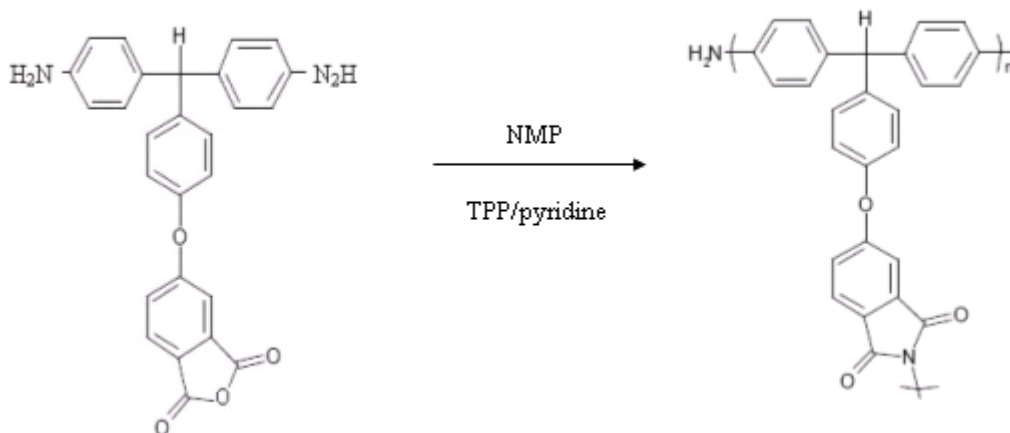
Scheme 3-2

3.4.2. Experimental Flow of LIB Experiment

The experimental flow for this part of study is shown in Fig. 3-6. The $LiCoO_2$ electrode contained 90 *wt*.% $LiCoO_2$ (LICO, Taiwan), 3 *wt*.% polyvinylidene fluoride (PVDF, Kuraha Chemical, Japan) binder and 7 *wt*.% conducting additives. The conducting additives were synthetic graphite (Timrex KS6, Timcal, Switzerland) and CNTs dispersed by various amounts of PEI. The mixture containing above ingredients were mixed by ball milling for 4 hrs and then coated onto 20-μm thick Al foil, dried at 140°C and pressed to form the $LiCoO_2$ electrode with final thickness of 120 μm. The coin cell assembly of LIB test cell is showed in Fig. 3-7.

.
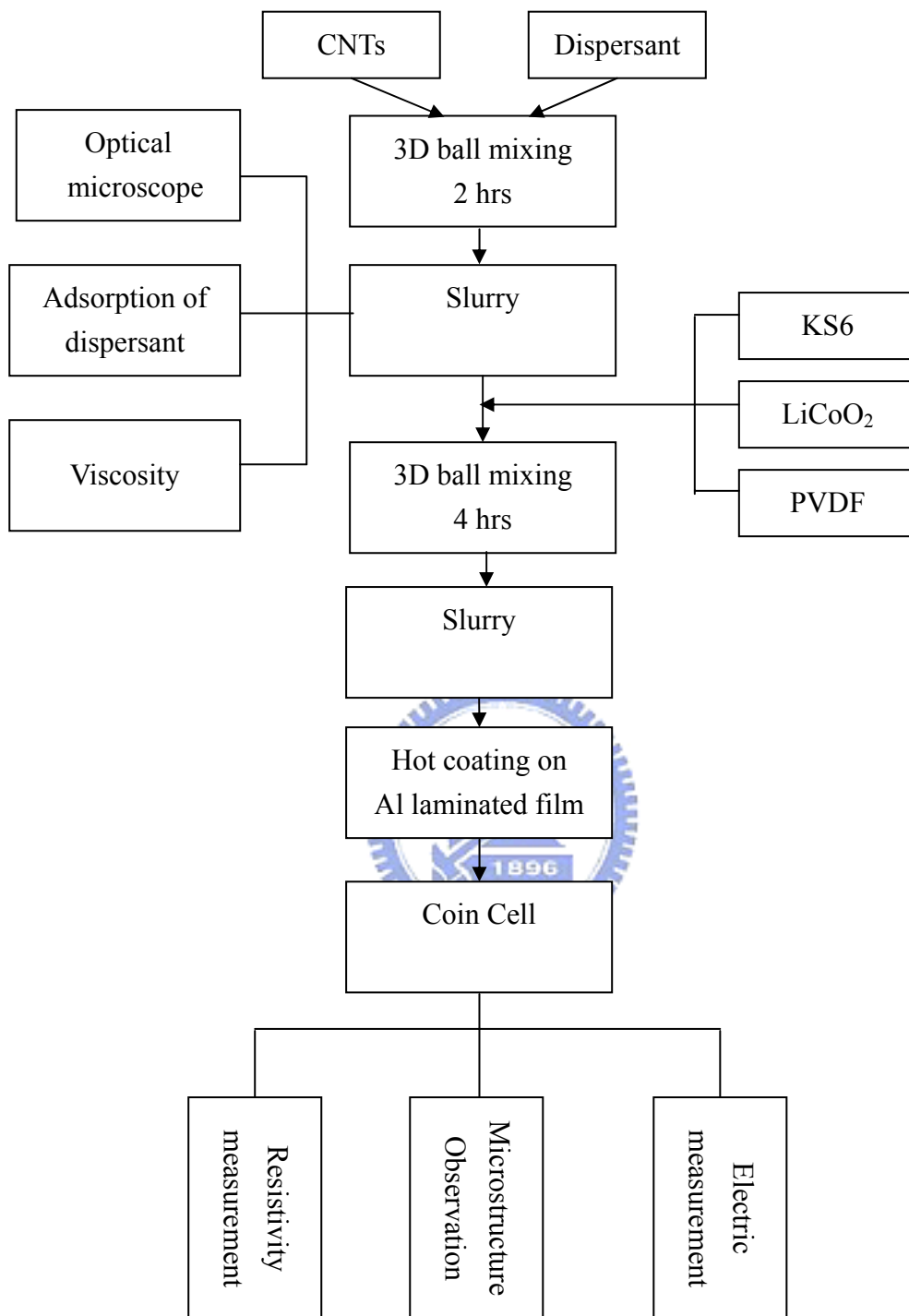
Figure 3-6. Experimental flow for LIB experiment.
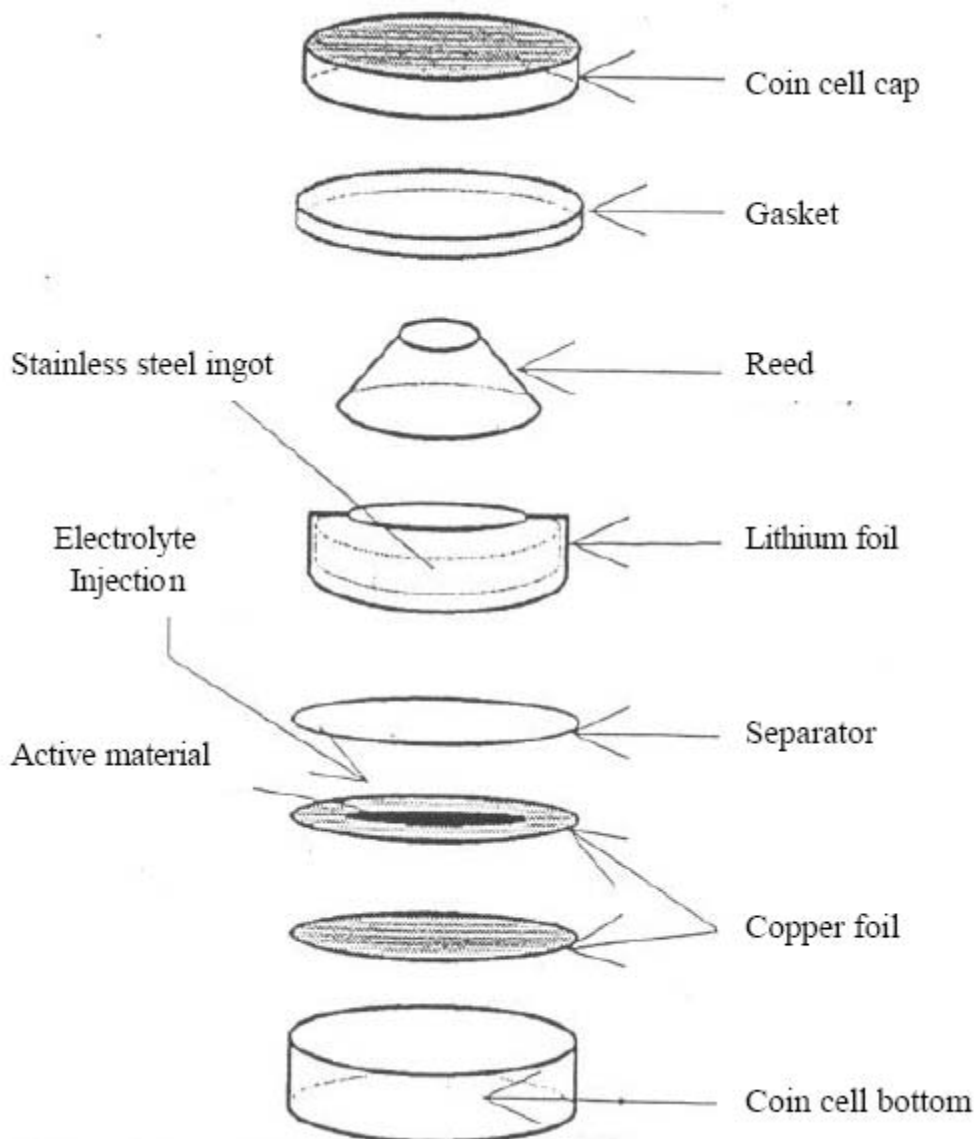
Figure 3-7. The coin cell assembly of LIB test cell.

3.4.3. Optical Microscopy

The CNTs slurry was first prepared with dispersant to confirm that the CNTs was dispersed. The dispersive effect was determined to Optical Microscope (OM, OLYMPUS-Mx40, Japan).

3.4.4. Viscosity Measurement

The rheology of CNTs slurry without or with chemical dispersants subjected to ball mixing was evaluated by a viscometer (ARES-LS1, Germany).

3.4.5. Adsorption of Dispersant

The CNTs suspensions with different concentrations of PEI were prepared. These suspensions were deagglomerated by a 3D ball mixing. After ball mixing, the suspensions were centrifuged at a speed of 1.5×10^4 rpm for 2 hrs to obtain supernatants. The residual dispersant concentration in the supernatants was analyzed and determined by a UV-Visible (V-600, JASCO/Japan). The amount of dispersant adsorbed on CNTs was calculated from the difference in dispersant concentration before and after adsorption.
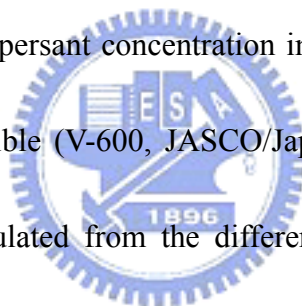
3.4.6. Microstructure Observation

The morphology and CNTs dispersive effect in $LiCoO_2$ electrode was obtained by scanning electron microscopy (SEM, Hitachi 4700).

3.4.7. Cyclic Voltammograms

The test cells without and with 2 *wt.*% PEI in $LiCoO_2$ electrode were evaluated

by a cyclic voltammograms (Biologic, Mac Pile II, USA) operating in between 2.9 and 4.2 V. The purpose of cyclic voltammogram test is to explore the oxidation reduction potential of the test cell and the electrochemistry change in the test cells.

3.4.8. Electrical Characterizations

Electrochemical impedance spectroscopy (EIS, Schlumberger, SI 1286 and SI 1255, England) operating at 3.5 V was adopted to characterize the impedance profile of half cell containing modified $LiCoO_2$ electrode. The measurement was carried out at the scanning frequencies ranged from 0.01 Hz to 50 kHz and with the perturbation amplitude of 10 mV. The cycling performance and charge-discharge capability of LIB test cells were carried out with the aid of charge-discharge apparatus (Arbin, model BT2042, USA) which enables a control of 5 cells synchronously at most. A charge-discharge test consisted of five cycles. The procedure was composed of a constant-current of 2 mA followed by constant-voltage at 4.2 V until the current tapered down to 0.2 mA. Both test cells were first charged at 0.2-C current density.

CHAPTER 4

Results and Discussion

4.1. Dispersion and Preparation of Nano-scale BTO materials

4.1.1. Rheological Behaviors

Viscosity measurement is commonly adopted to evaluate the dispersed extent of concentrated suspensions. Figure 4-1 shows the effect of dispersant concentration on the viscosity of 60 *wt*.% BTO suspensions subjected to conventional ball milling or nano grinding/mixing *via* MiniZeta mill. The viscosity of suspensions without dispersion treatment is about 3200 cps. For the suspensions subjected to different mechanical milling processes, their viscosities decrease when PMAA-Na or PDAAE is incorporated. The viscosity of suspensions first decreases with the increase of dispersant concentration then reaches a plateau. At same of dispersants concentration, the viscosity of suspensions subjected to nano grinding/milling exhibits a lower value in comparison with that of suspensions subjected to conventional ball milling. For the suspensions subjected to nano grinding/mixing, the optimum chemical dispersant concentrations in BTO suspensions are about 2 *wt*.% for PMAA-Na and 3 *wt*.% for PDAAE, which respectively result in the lowest viscosities of 15 and 76 cps.

Figure 4-1 also shows that the suspension containing PMAA-Na exhibits the

51

sharpest descend of viscosity and the amount of PMAA-Na to achieve the lowest

value of viscosity is less in comparison with that of PDAAE. As the PMAA-Na and

PDAAE both have similar molecular weight, the difference in the rheological

behaviors is attributed to the difference of chemical structures. The PMAA-Na is

anionic polyelectrolyte, which causes mainly electrostatic repulsion when adsorbed

on BTO particles. Though PDAAE also causes electrostatic repulsion when adsorbed

on BTO surface, the effect is relatively less because PDAAE is amphibious

polyelectrolyte.
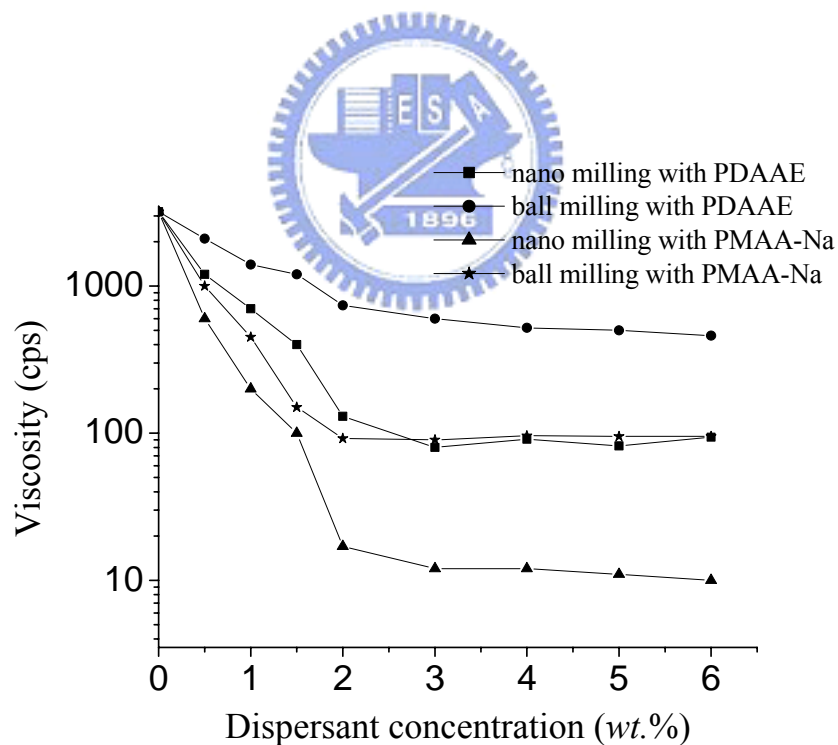
Figure 4-1. The effect of dispersant concentration on the viscosity of 60 *wt*.% BTO

suspensions subjected to various grinding/mixing processes.

4.1.2. Particle Size Distribution

In conventional ball milling, slurry and grinding media are sealed in a bottle and the grinding/mixing is achieved by the rotation motion of grinding balls. Such a milling process provides a relatively low shear force that it is insufficient to achieve nano-scale dispersion. In this work, the MiniZeta mill using the 2-mm-diameter ZrO_2 balls as the grinding media was able to grind the BTO powder down to the sizes smaller then 100 nm. By using the principle of agitator bead mills, a special agitator shaft rotating at a speed as high as 3600 rpm accelerated the grinding media in the MiniZeta mill chamber. It not only provided superfine grinding, but also generated a rather large shear force to disperse the slurry. In addition, the multi-passage grinding/mixing path adopted by MiniZeta mill is able to reduce the sizes of BTO powders in a relatively short time span.

Figure 4-2 presents the mean particle size (d_{50}) of powder as a function of dispersant concentration in 30 $wt.$% BTO suspensions subjected to nano or conventional milling processes. The initial value of d_{50} of powder without chemical dispersants in suspensions is 1 μm. With the increasing amount of chemical dispersant, the values of d_{50} of powders in all types of suspensions decrease. As shown in Figure 4-2, the variation of d_{50} with the dispersant concentration is very much the same as that of viscosity presented in Fig. 4-2. The smallest d_{50} of BTO suspensions occurs at

about 2 *wt*.% for PMAA-Na and 3 *wt*.% for PDAAE; it equals to 80 nm and 83 nm,

respectively. Apparently, more PDAAE are required to achieve the smallest d_{50} in

suspensions and the minimum particle size in suspension containing PDAAE is

slightly larger than that in suspension containing PMAA-Na.
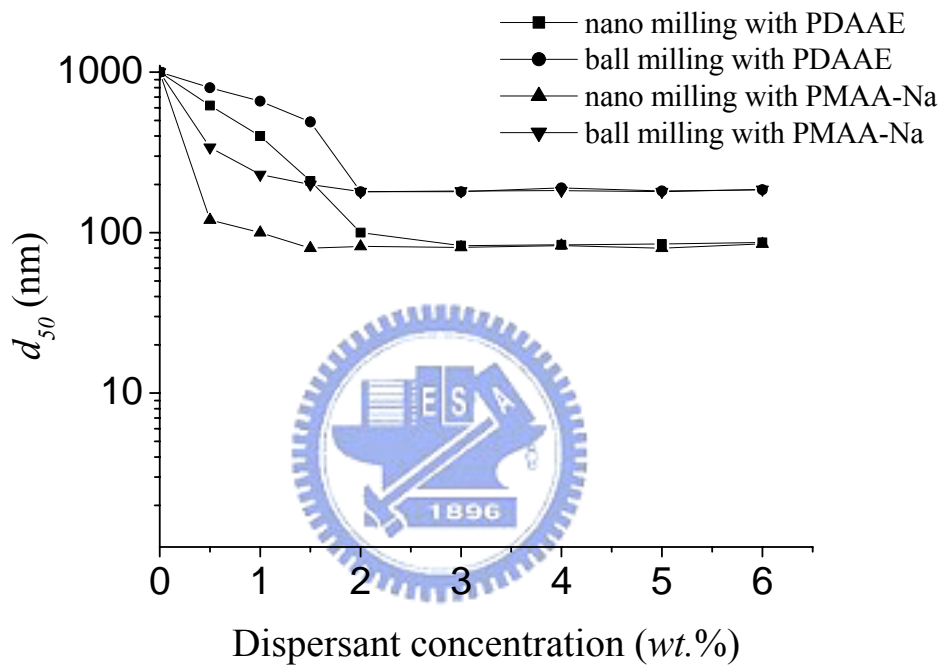
Figure 4-2. The effect of dispersant concentration on the mean particle size (d_{50}) of

powder in 30 *wt*.% BTO suspensions subjected to different

grinding/mixing processes.

Figures 4-3 and 4-4 respectively show the particle size distributions of 30 *wt*.%

BTO slurries containing 2 *wt*.% PMAA-Na and 3 *wt*.% PDAAE subjected to

conventional and nano milling processes. The d_{50}'s of suspensions subjected to the

nano grinding/mixing are 80 nm for PMAA-Na and 83 nm for PDAAE, while that of

suspensions subjected to conventional ball milling are 180 nm for PMAA-Na and 181

nm for PDAAE. Furthermore, narrower shape of distribution curve implies a more

uniform size of BTO particles in the suspensions subjected to nano grinding/mixing

process. It was also found that average size of BTO in suspension without any

mechanical milling is in the range of 200 nm. This indicated that the high shear force

provided by an appropriate mechanical milling process is also beneficial to the

stability of suspensions. Owing to the larger SSA and van der Waals force, the

nano-scale particles in slurry tend to agglomerate together. In addition to the chemical

dispersant, a mechanical milling process that is able to provide sufficient shear force

is required in order to achieve satisfactory dispersion of nano-scale BTO particles in

aqueous suspension.
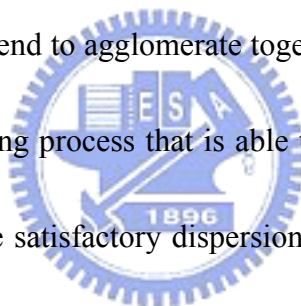
Experimental results of viscosity and particle size distribution also indicated that

a sole mechanical milling process is insufficient to disperse nano-sized BTO particles

in suspensions. Though nano grinding/mixing *via* the MiniZeta mill provides a large

shear force to disperse the particles, it cannot stabilize the suspensions. Owing to the

large SSA and van der Waals force, the particles subjected to nano grinding/mixing

still tend to agglomerate together if the suspensions were free of chemical dispersant.

Hence, in addition to mechanical milling, appropriate amount of chemical dispersant

has to be added to provide sufficient electrostatic repulsions and steric effect in suspensions so that a stable, uniform dispersion in nanometer scale could be obtained.
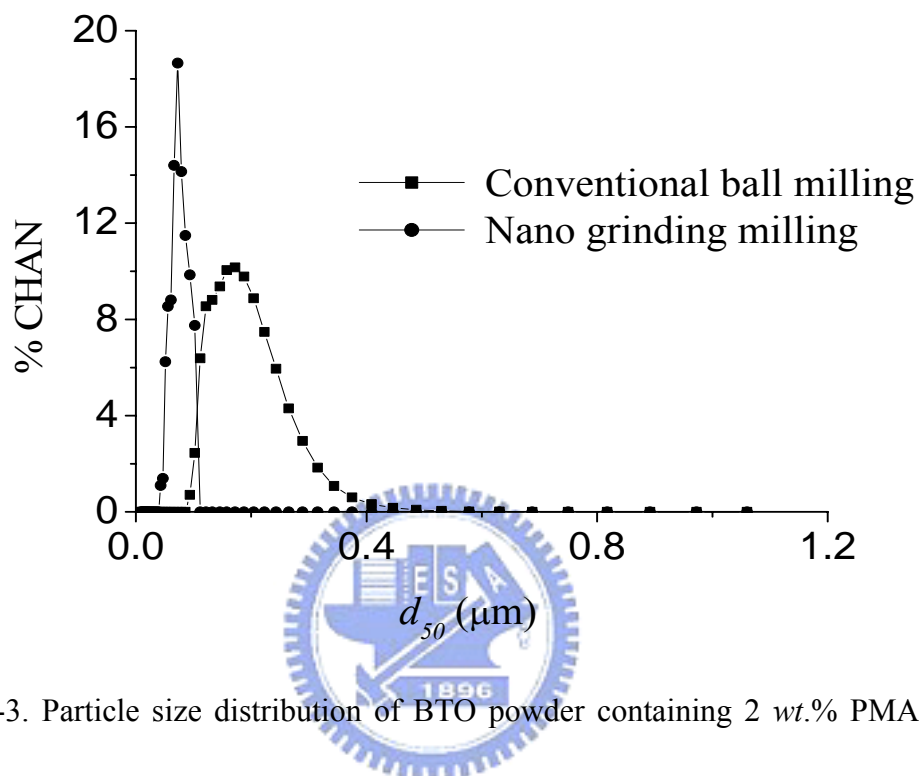
Figure 4-3. Particle size distribution of BTO powder containing 2 *wt*.% PMAA-Na

subjected to conventional ball milling and nano grinding/mixing processes.

4.1.3. Zeta Potentials

Electrokinetic measurements are widely used to assess the magnitude and sign of particle surface charge as a function of pH value in suspension.[21,55] Figure 4-5 presents the zeta potentials of 30 *wt*.% BTO powder as function of pH values of suspension. Isoelectric points for 80-nm-BTO was at pH = 3.8; for 180-nm-BTO was at pH = 4.5; and for 1-μm-BTO was at pH = 5.2. This indicates the BTO particles tend

to stabilize in aqueous solutions of high pH values.
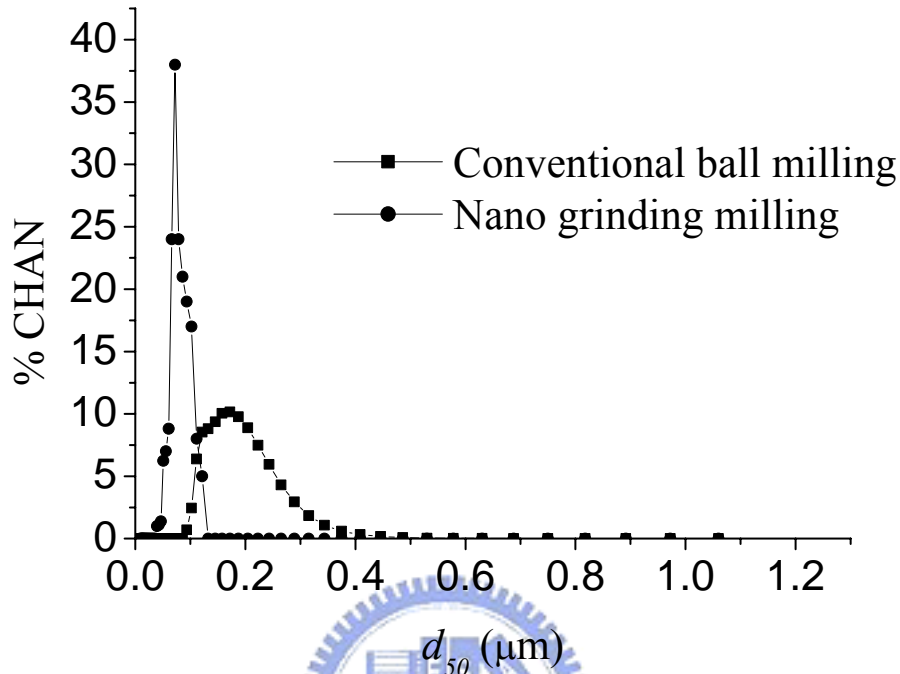
Figure 4-4. Particle size distribution of BTO powder containing 3 *wt*.% PDAAE

subjected to conventional ball milling and nano grinding/mixing processes.

The hydrolysis of BTO in acidic environment is as follows[18]:

$$BaTiO_{3(s)} + H_2O_{(l)} = Ba^{2+}_{(aq)} + TiO_{2(rutile)} + 2OH^-_{(aq)} \qquad (4\text{-}1)$$

$$BaTiO_{3(s)} + 2H^+_{(aq)} = Ba^{2+}_{(aq)} + TiO_{2(rutile)} + H_2O_{(l)} \qquad (4\text{-}2)$$
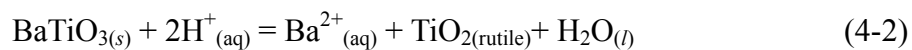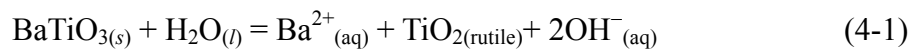
Nano-scale BTO particles possess large SSA. When $HNO_{3(aq)}$ was added into the

suspension, the pH value decreased and more Ba^{2+} ions tended to leach out from the

surface of BTO. The Ba^{2+} ions could nullify some negative charges on the surface of

the BTO, so the zeta potential shows a more positive value as revealed by Eq.(4-2).

On the other hand, when NH_4OH was added into the suspension, the pH increased and

the resulted OH^- ions could neutralize the positive charges on the surface of BTO so

that the negative trend of the zeta potential increased.
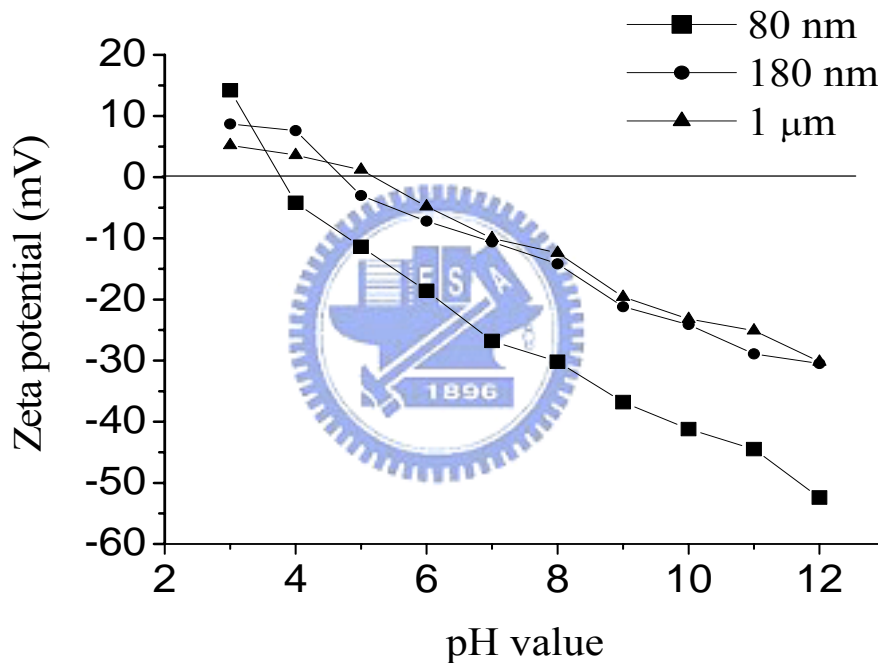
Figure 4-5. Zeta potentials of BTO suspensions at different particle sizes.

Figure 4-6 shows that the zeta potentials for BTO suspensions containing

PMAA-Na or PDAAE at pH = 9.5. It can be seen that at the same particle size, the

zeta potential for the suspension containing PMAA-Na is more negative than that

containing PDAAE. At pH = 9.5, the surface of nano-scale BTO particles is highly

negative charged so that the adsorption of dispersant on particle surface is more

difficult in comparison with the micro-scale particles. This suggests that the rejection

caused by the net negative electric charge of the particles and, for PMAA molecules,

rejection becomes more severe when the particle size is down to nanometer scale.

However, the PDAAE molecules become amphibious in a basic solution (*i.e.*, at the

condition of pH = 9.5). The molecules contain cationic functional groups ($-N^+R_3$)

would favor themselves to be adsorbed on the surface of BTO particles.
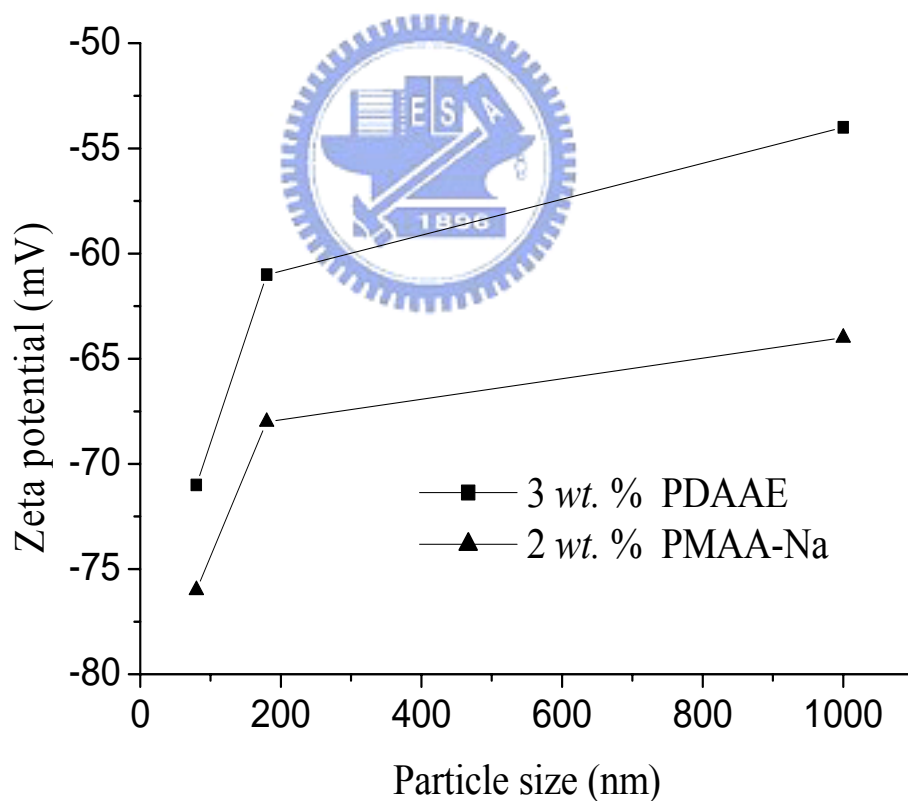
Figure 4-6. Zeta potentials of BTO suspensions containing different chemical

dispersants.

4.1.4 Adsorption of Dispersants on BTO

Figures 4-7 and 4-8 show the specific adsorptions of PMAA-Na and PDAAE on the BTO particles in suspensions at pH = 9.5, respectively. For both types of suspensions, the specific adsorption behaviors suggest a monolayer adsorption concentration onto the particle surface; however, the critical dispersant concentrations to reach the adsorption plateau are different. For PMAA-Na, the critical value decreases with the decrease of particle size and *vice versa* for PDAAE. The critical dispersant concentrations to reach the adsorption plateau for these two types of suspensions are listed in Table 4-1.
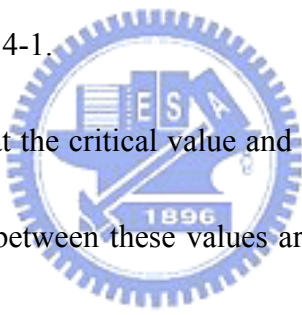
Table 4-1 clear shows that the critical value and amount of absorbent are greater for PDAAE. The differences between these values are attributed to the difference of chemical structures of these two dispersants. At pH = 9.5, the surface charge of BTO particles are negative. For PMAA-Na, its molecules are completely dissociated and become negatively charged. Therefore, it is difficult for PMAA-Na molecules to be adsorbed on the BTO surface. On the contrary, PDAAE molecules become amphibious in a basic solution and the existence of cationic functional groups ($-N^+R_3$) favors the absorption of PDAAE on BTO surface. Accordingly, the amount of adsorbed PDAAE molecules is more than that of PMAA-Na molecules.

Furthermore, an interesting behavior of the adsorption isotherms was observed in

this work. For the BTO particles of different sizes, the initial adsorption behaviors were distinctly different when different dispersant was added. This clearly suggested that nano-scale particles possess highly negative charge on surface that inhibits the adsorption of negatively charged dispersant or increases the adsorption of amphibious charged dispersant. Another possible explanation was that the dispersants might adsorb on the large-sized particles in an orientation that permits higher extent of adsorption on particle surface.[12]

Table 4-1. Critical dispersant concentrations to reach the adsorption plateau.

Dispersant \ Particle size	80 nm	180 nm	1 μm
PMAA-Na	0.03 ~ 0.04 mg	0.11 ~ 0.12 mg	0.25 ~ 0.3 mg
PDAAE	2.8 ~ 3.3 mg	1.1 ~ 1.2 mg	0.3 ~ 0.4 mg

(Unit: per gram of BTO)
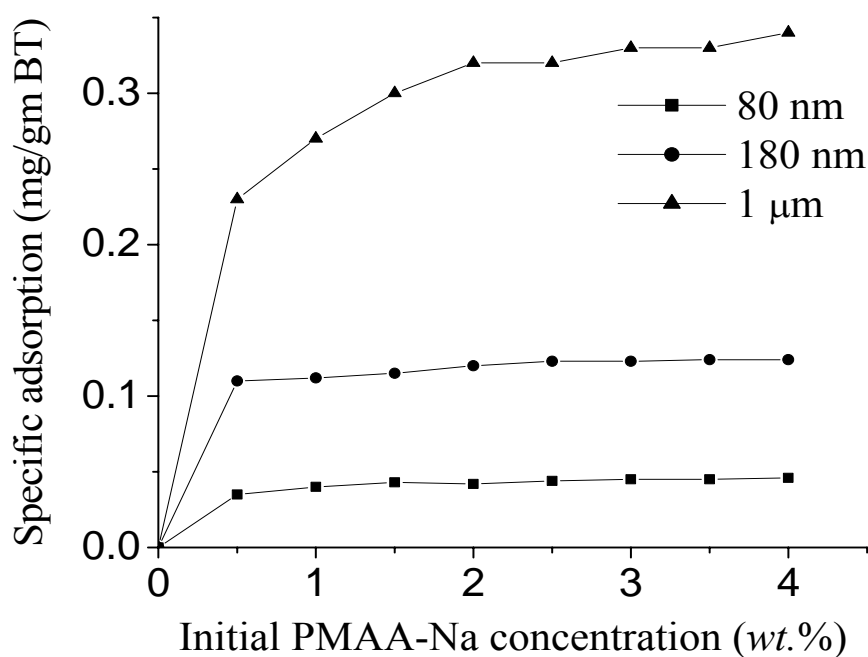
Figure 4-7. Specific adsorption of PMAA-Na on BTO of different particle sizes.
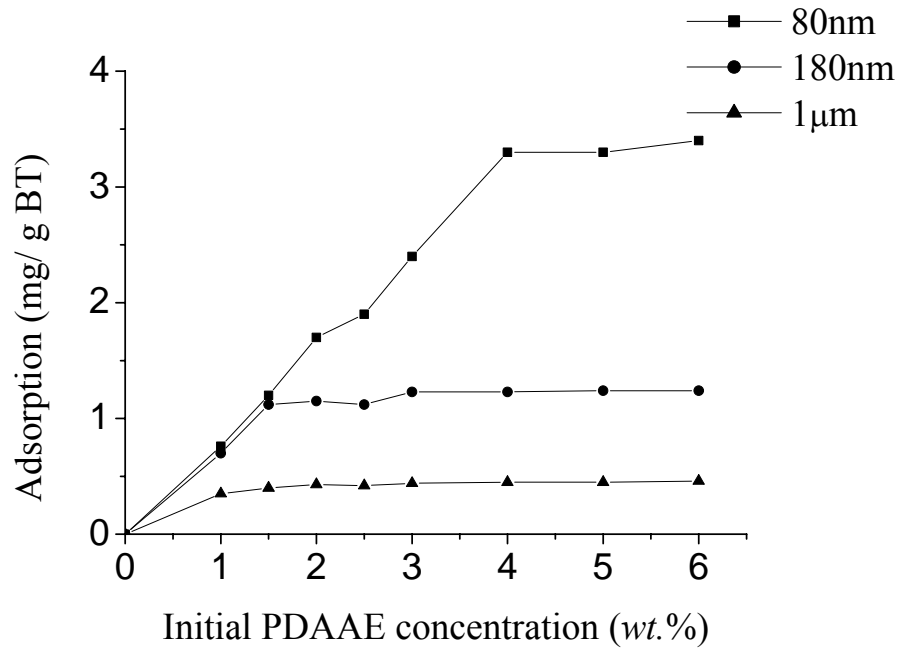
Figure 4-8. Specific adsorption of PDAAE on BTO particles of different particle

sizes.

To determine monolayer PMAA-Na and PDAAEE adsorption quantitatively, the

data in shown in Figs. 4-7 and 4-8 were analyzed by using the Langmuir monolayer

adsorption equation:

$$\frac{Ce}{As} = \frac{Ce}{Cm} + \frac{k}{Cm}$$ (4-3)

where Ce is the equilibrium concentration of dispersants in solution, As is the

adsorbent of the dispersant, and Cm is the monolayer adsorbent of the dispersant, and

k is a constant. The plots of Ce/As versus Ce for these two types of suspensions are

shown in Figs. 4-9 and 4-10, respectively. The slopes of these straight lines represent

the reciprocal of the monolayer adsorption of dispersant ($1/Cm$) and the results are

summarized in Table 4-2. It can be seen that the amount of monolayer PMAA-Na

adsorption decreases with the decrease of particle size and *vice versa* for the case of

PDAAE. However, the results of adsorption and zeta potential indicated that both

PDAAE and PMAA-Na could successfully stabilize the nano BTO slurry. The

dispersive capability of PDAAE is steric effect and electrostatic repulsion, but the

PMAA-Na is solely electrostatic repulsion.
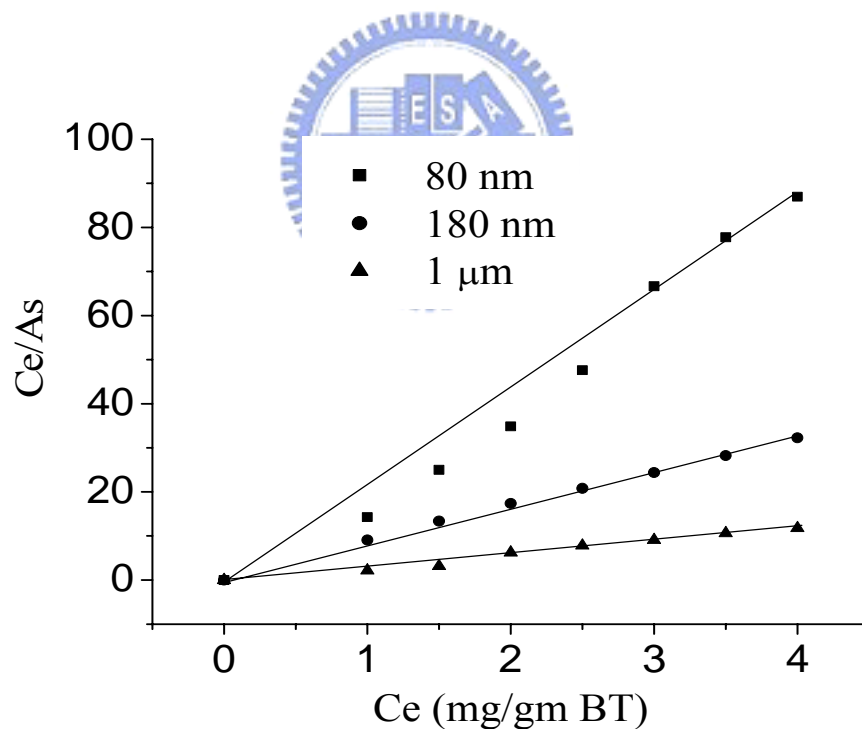
Figure 4-9. Langmuir analysis for the suspension containing PMAA-Na.
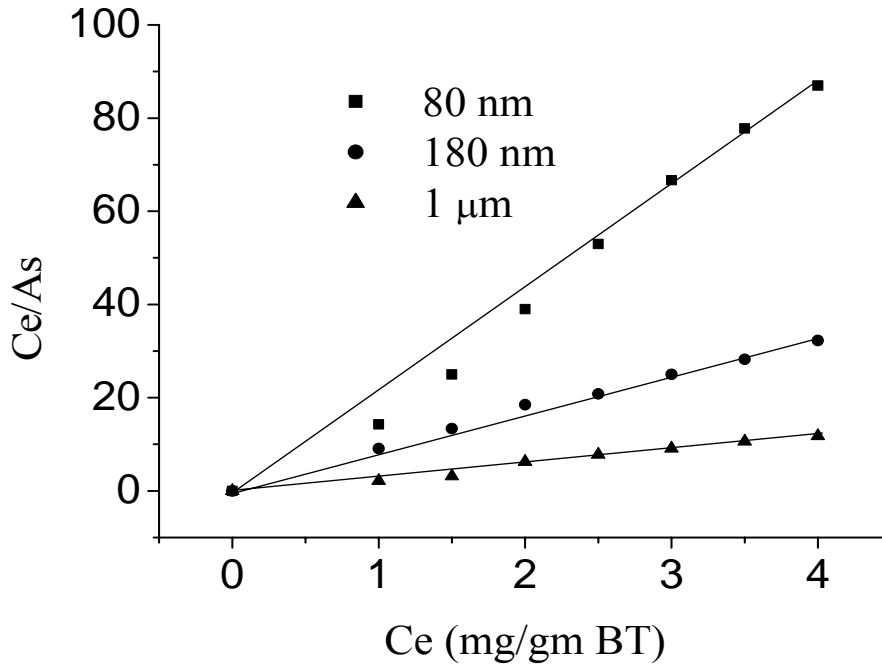
Figure 4-10. Langmuir analysis for the suspension containing PDAAE.

Table 4-2. Monolayer absorption of dispersants on BTO surface.

Particle size Dispersant	80 nm	180 nm	1 μm
PMAA-Na	0.04 mg	0.12 mg	0.32 mg
PDAAE	3.2 mg	1.2 mg	0.4 mg

(Unit: per gram of BTO)

4.1.5. Microstructures

Figure 4-11 shows the morphology of the BTO particles subjected to the chemical dispersion and physical grinding/mixing process. The average size of BTO particles was about 80 nm and no aggregation was observed. This evidenced that the PMMA-Na salt is an appropriate chemical dispersant for the preparation of aqueous nano-BTO solution.
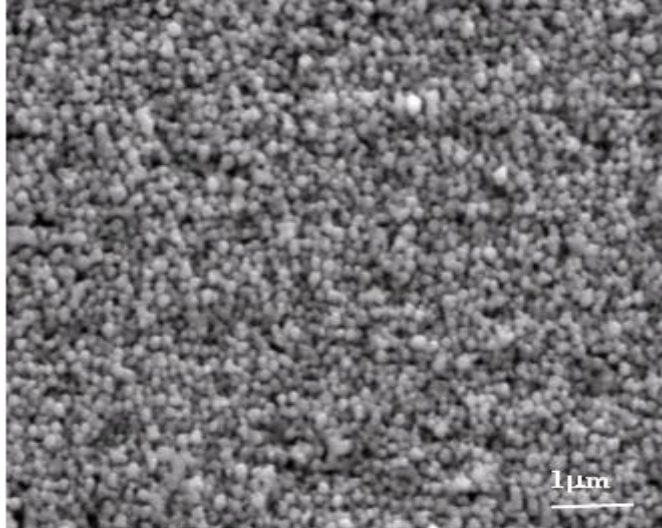
Figure 4-11. SEM Micrograph of nano-sized BTO powders subjected to chemical

dispersion and physical grinding/mixing process.

The microstructures of BTO sintered in the temperatures ranging from 1100 to

1300°C for 6 hrs are depicted in Figs. 4-12(a) to 12(c). The grain sizes of BTO evolve

as follows: at 1100°C, 140 nm; at 1200°C, 900 nm; and at 1300°C, 70 μm. The SEM

morphology observation in conjunction with the results of density measurement

shown in Fig. 4-12 indicates that both the densities of sintered body and grain sizes of

BTO increase with the sintering temperatures. Further, the results presented in Figs.

4-12 and 4-13 revealed three distinct densification processes for nano-BTO particles

at different sintering conditions. When sintering temperatures were below 1100°C,

densification and grain growth are both insignificant that, in essential, no sintering

occurred. For the samples sintered in between 1100 to 1200°C for less than 6 hrs, a

rapid densification takes place with a relatively slow grain growth. When sintering

times exceeded for 5 hrs at 1300°C, grain growth dominated and a slight desintering

phenomenon occurred when sintering times were further increased. As suggested by

previous study,[6] the desintering phenomenon might be caused by gas releasing and/or

abnormal grain growth during sintering.

Figure 4-14 plots the relative density and grain size *versus* sintering time of

nano-BTO sintered at 1100°C. After 6-hr sintering, the sample exhibits a relatively

high densification (about 95% T.D.) with a moderate grain growth that the average

grain size of BTO sample increases from about 80 to 140 nm. This indicates that for

the sintering of nano-BTO powders, grain growth occurs earlier in comparison with

conventional process that the apparent grain growth usually occurs at the end of

sintering.[46] Occurrence of grain growth at the early stage of sintering was attributed to

large SSA of nano-BTO powders. The nano-particles tended to reduce the surface

energy of sample by eliminating the total surface area. Interface-driven processes such

as grain boundary diffusion and surface diffusion dominated the mass transport at the

early stage of sintering and hence a premature grain growth was observed.
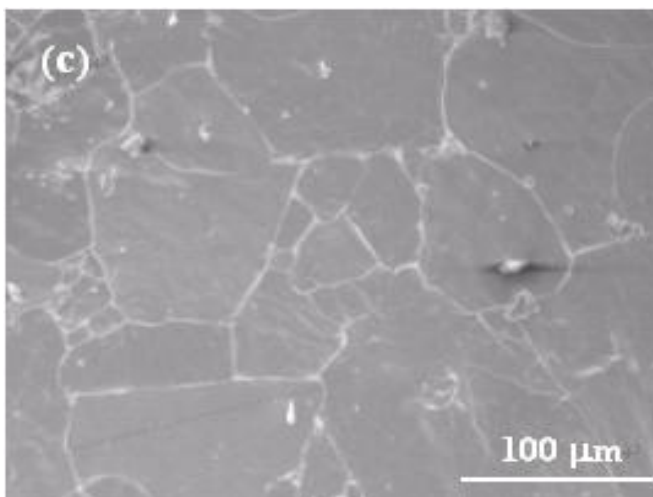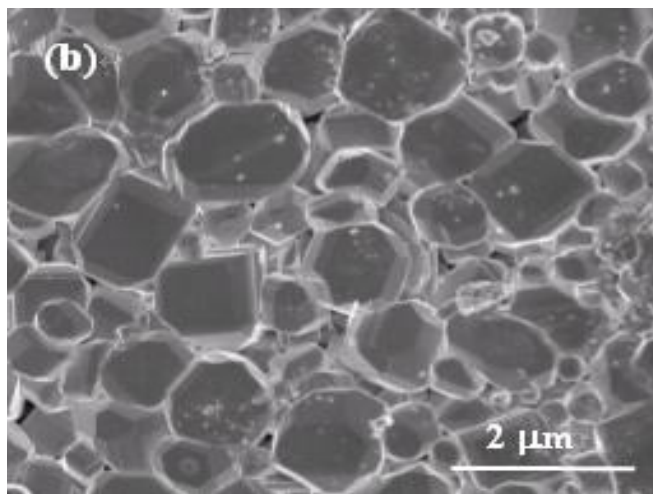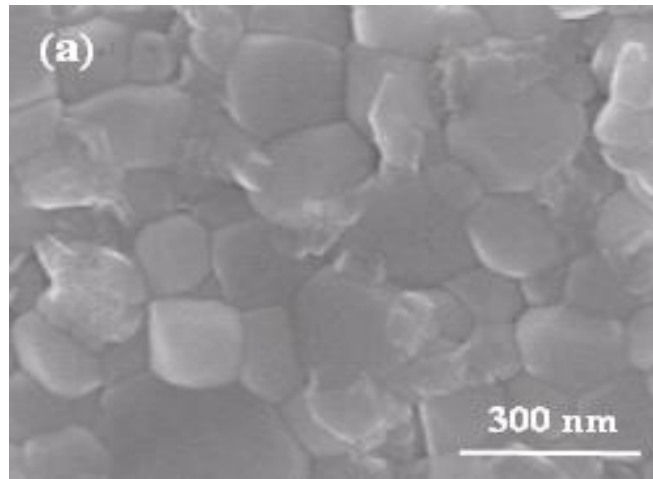
Figure 4-12. SEM Micrographs of nano-BTO sintered at (a) 1100°C (b) 1200°C (c) 1300°C for 6 hrs.
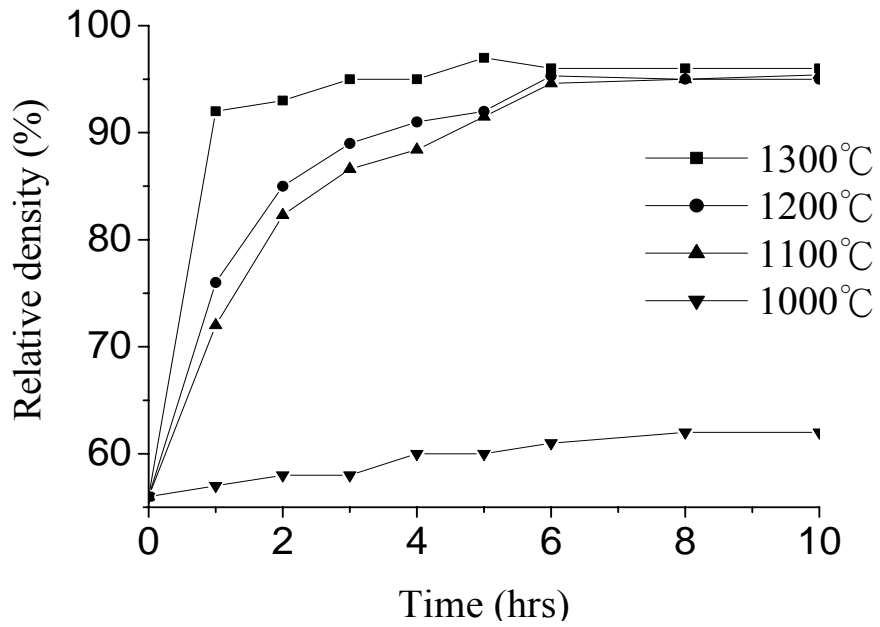
Figure 4-13. Relative density change *versus* sintering times at different temperatures.
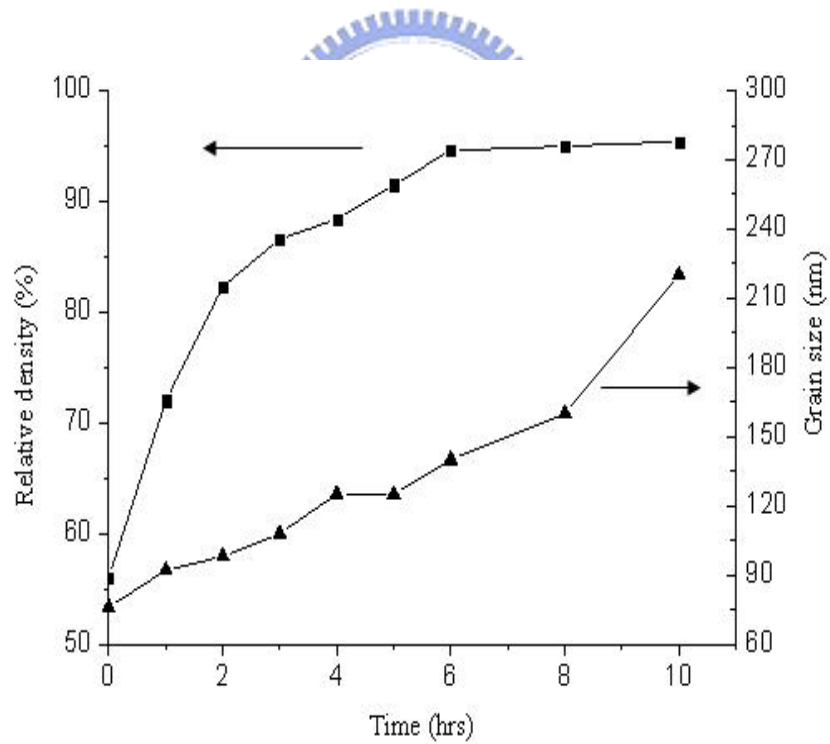
Figure 4-14. The relative density and grain size *versus* sintering time of sample sintered at 1100°C.

4.1.6. Phase Constitution

Figure 4-15 presents the XRD patterns for the samples sintered at temperatures ranging from 1000 to 1300°C for 6 hrs. At the temperatures below 1000°C, tetragonal BTO phase remains insignificant. However, the tetragonal BTO becomes the dominant phase at 1100°C and, when the sintering temperature is raised to 1200°C, most of tetragonal phase evolves into the monoclinic phase. After the 1300°C-sintering, the BTO is overwhelmed by the cubic phase. The XRD pattern for the sample sintered at 1200°C indicates that diffraction peaks corresponding to tetragonal phase are relatively weak in comparison with those corresponding to monoclinic phase. Table 4-3 shows the Ba:Ti ratio obtained by using the EDS attached to SEM. The higher Ba:Ti ratio ≈ 1:1.76 indicates that the stoichiometry of monoclinic phase is likely $BaTi_2O_5$. It was hence concluded that the phase constitution for the sample sintered at 1200°C is monoclinic $BaTi_2O_5$ mixed with a relatively small amount of tetragonal BTO.

Previous studies reported that the $BaTi_2O_5$ may form in the surface reaction layer and also in the bulk of $BaTiO_3$ pellets when the $BaO-TiO_2$ samples were sintered in oxygen-rich ambient at high temperatures.[19] It was also found that the $BaTi_2O_5$ is of paraelectric[19] and, when monoclinic $BaTi_2O_5$ is present in BTO, it would shift the capacitor sample from ferroelectric to paraelectric and hence decrease its dielectric

constant.[19]
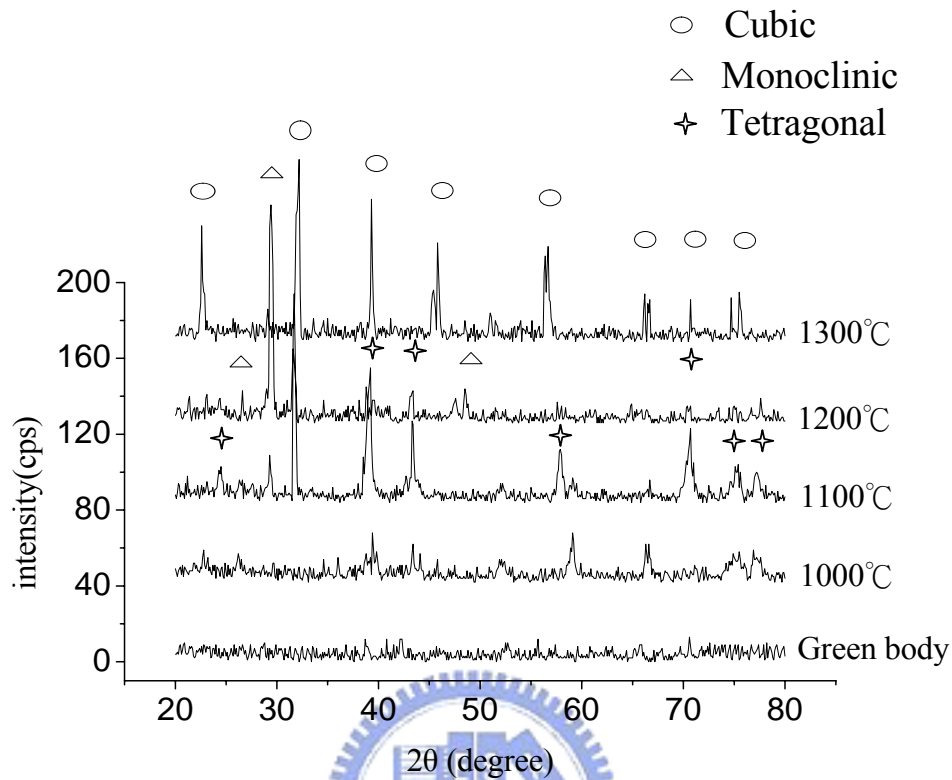
Figure 4-15. The XRD patterns for the BTO sintered at different temperatures.

Table 4-3. The EDS analysis of Ba:Ti ratio of samples sintered at different

temperatures for 6 hrs.

Sintering temperatures	Ba:Ti ratio
1100°C	1:1.12
1200°C	1:1.76
1300°C	1:1.14

4.1.7. Dielectric Properties

Figures 4-16, 4-17 and 4-18 presents the 1-kHz dielectric constants and dielectric

losses *versus* the grain sizes of BTO sintered at 1100, 1200 and 1300°C, respectively.

It can be seen that for the samples sintered at 1100 and 1200°C, the dielectric constant first increases with the increase of grain sizes then decreases with the further increase of grain sizes and *vice versa* for the dielectric loss. The highest dielectric constant about 8000 and lowest dielectric loss about 5×10^{-3} were achieved in the sample sintered at 1100°C for 6 hrs with grain size about 140 nm. As to the samples sintered at 1300°C, the dielectric constant decreases and dielectric loss increases monotonically with the increase of grain sizes, which is in the same trend as reported by previous studies relating to micro-scale BTO.[25]

The sintering temperatures for conventional BTO process usually exceed 1300°C. The results above clearly indicate that, in addition to the upgrading of dielectric properties, the sintering temperature for nano-BTO is 200°C lower than that for conventional process. The reduction of sintering would be a merit of thermal budget for the BTO device fabrication.

During the sintering of nano-BTO, the voids might be rapidly eliminated at the early stage of sintering due to the mass transport processes driven by the large SSA of nano-particles. A relatively dense sintered body thus might achieve prior to the apparent coarsening of grains, resulting in distinct dielectric properties as shown in Fig. 4-16. Figure 4-16 also shows that when the grain sizes exceeds 200 nm, the dielectric constants decrease and dielectric losses increase with the increase of grain

sizes. Though further grain growth implies denser sintered body, the grain sizes

become micro-scale and the samples exhibit the dielectric properties similar to those

of conventional BTO samples.[19,25] The results above evidence that the adoption of

nano-BTO powder for device fabrication requires specific control on the sintering

condition so as to obtain desired dielectric properties.
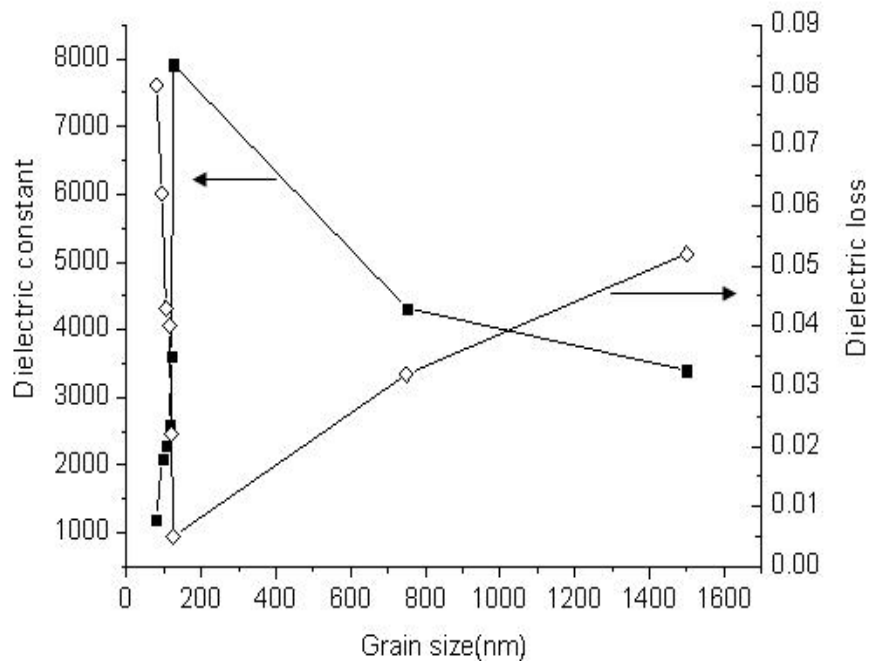
Figure 4-16. 1-kHz dielectric constants and loss *versus* grain sizes of nano-BTO

sintered at 1100°C.

A comparison of Figs. 4-17 and 4-18 shows that the dielectric properties of

1200°C-sintered BTO are inferior to those of 1100°C-sintered BTO thought they

exhibit a similar trend of property change with the grain sizes. The decrease of

dielectric constant of 1200°C-sintered BTO was attributed to the presence of monoclinic $BaTi_2O_5$ phase as indicated by XRD and EDS analyses. As stated previously, $BaTi_2O_5$ is paraelectric[19] and its presence reduces the spontaneous polarization and thus deteriorates the overall dielectric performance of the capacitor sample.[19]
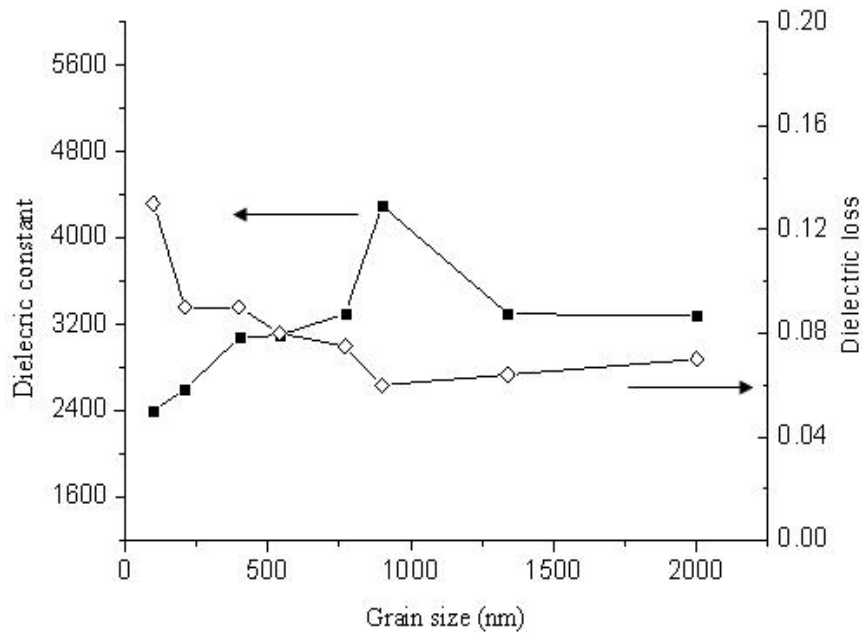
Figure 4-17. 1-kHz dielectric constants and loss *versus* grain sizes of BTO sintered at

1200°C.
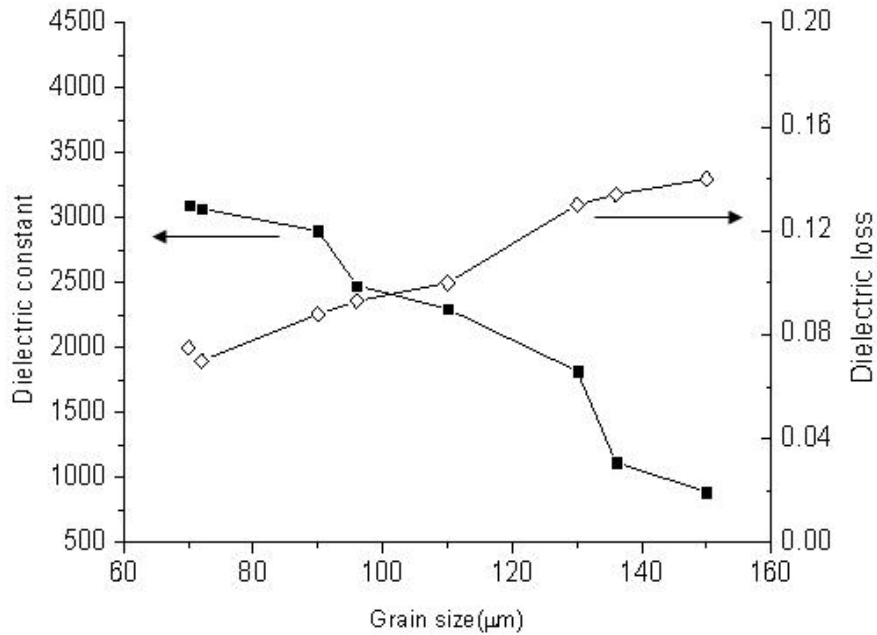
Figure 4-18. 1-kHz dielectric constants and loss *versus* grain sizes of BTO sintered at

1300°C.

4.2. Preparation of Nano-BST Ceramics and Their Characteristics

Barium Strontium titanate ($Ba_{1-x}Sr_xTiO_3$, BST) is widely used in many

application because of its exception high dielectric constant. The BST have been used

in the multilayer ceramic capacitor (MLCC) and positive temperature coefficient

resistor (PTCR).[56] Many studies have been done on the dielectric properties of BST

and the best dielectric properties of BST at about $x = 0.3$, in this work we hence chose

to prepare the BST samples at such a stoichiometric ratio and investigated the

dielectric properties and their relationships to microstructure.[54]

In this work we try to identify the dispersion method of nano-BST powder and the

74

sintering process of capacitor samples based on such a BST powder so that an in-depth understanding on the microstructure evolution and its effects on dielectric properties of BST could be obtained.

4.2.1. Dispersion and Preparation of Nano-BST Ceramic

Before sintering, the mixture of BTO and STO powders must be dispersed in order to eliminate the agglomeration caused by van der Waals attraction resulted from large SSA of nano-sized particles. Figure 4-19 presents the morphology of the mixed powders subjected to chemical dispersion and physical grinding described previously. The mean particle diameter measured from Fig. 4-19 is about 60 nm. Particle size distribution of the dispersed mixed powder is plotted in Fig. 4-20. It shows the average particle size is about 60 nm and, in conjunction with the morphology shown in Fig. 4-19, hence there is no aggregation of BTO/STO powders in slurry.

In Section 4.1 reported that PDAAE is able to provide the electrostatic repulsion and steric hindrance between the particles to inhibit the agglomeration. This study hence adopted the same dispersion formula to disperse the BTO/STO powders. The rheological measurement of aqueous suspension shown in Fig. 4-21 reveals that the viscosity of suspension is rather low ($\eta \approx 10$ mPa·s) and its variation along with the shear rate is relatively small. This implies the Newtonian fluid behaviors of BTO/STO

slurry and hence, according to the studies of Cesarano *et. al*.,[4] a good dispersion of

BTO/STO powders in the aqueous suspension. The dispersion method for nano-BTO

powder is hence equally applied to the dispersion of nano-scale BTO/STO powders.
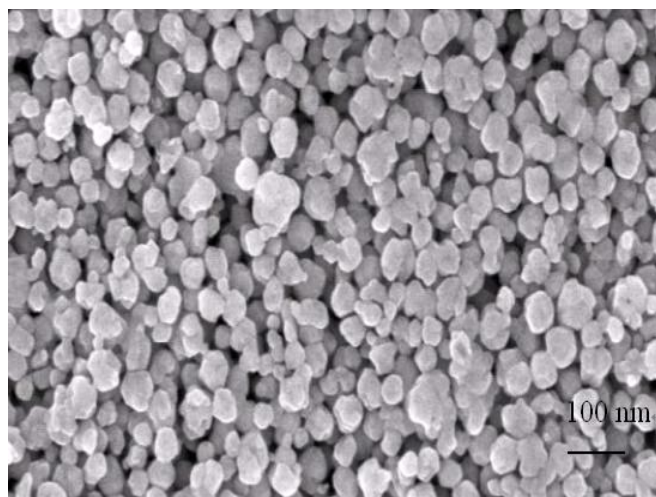
Figure 4-19. SEM micrograph of nano-scale BST powders subjected to chemical

dispersion and physical grinding process.

4.2.2. Sintering Behaviors and Microstructure Evolution

Figure 4-22 depicts the relative density of capacitor samples (called nano-BST

samples hereafter) prepared *via* the solid-state reaction of BTO/STO powders as a

function of sintering temperatures. For all samples, sintering duration was fixed at 1

hr. It shows that the increase of density is relatively slow below 1000°C; in between

1000 to 1200°C, densities increases rapidly; beyond 1200°C, the densities become

saturated at about 95%. The plot in Fig. 4-22 indicates that the densification of
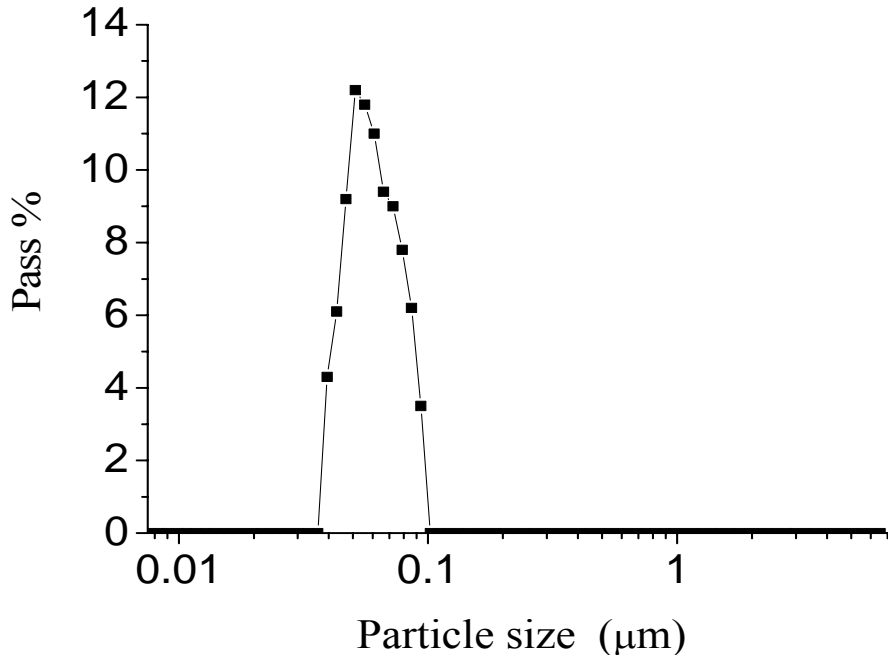
Figure 4-20. Particle size distribution of nano-BST powder in the slurry subjected to

chemical dispersion and physical grinding process.
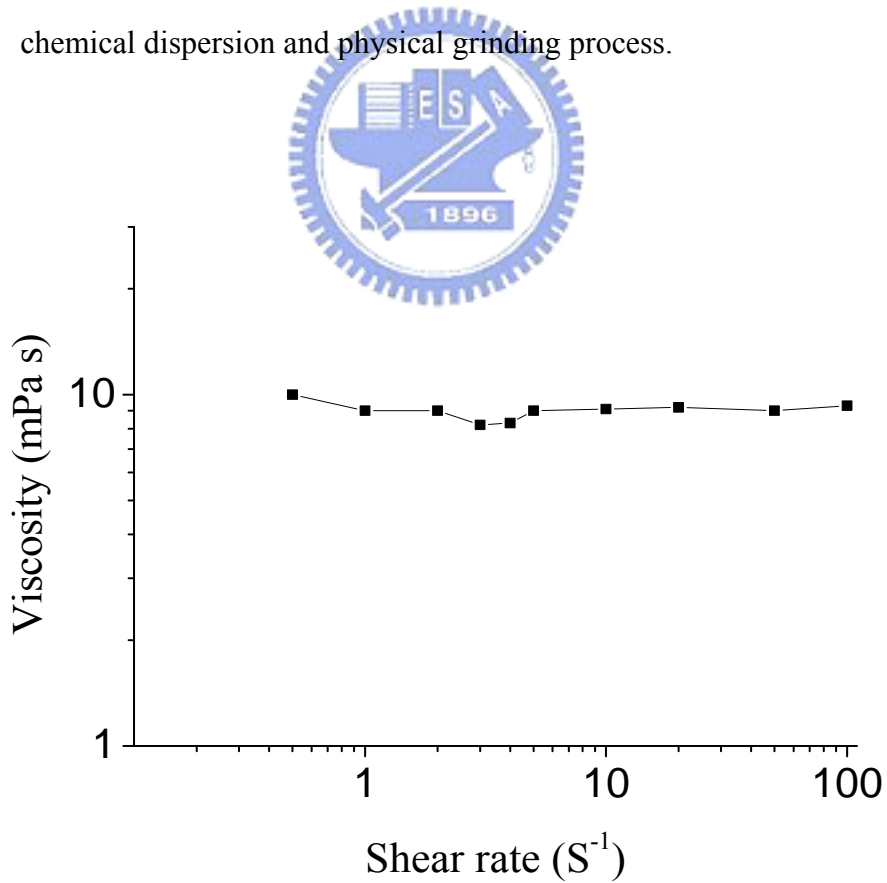
Figure 4-21. Viscosity of aqueous suspensions containing nano-BST powder and 5

wt.% of PDAAE as a function of shear rate.
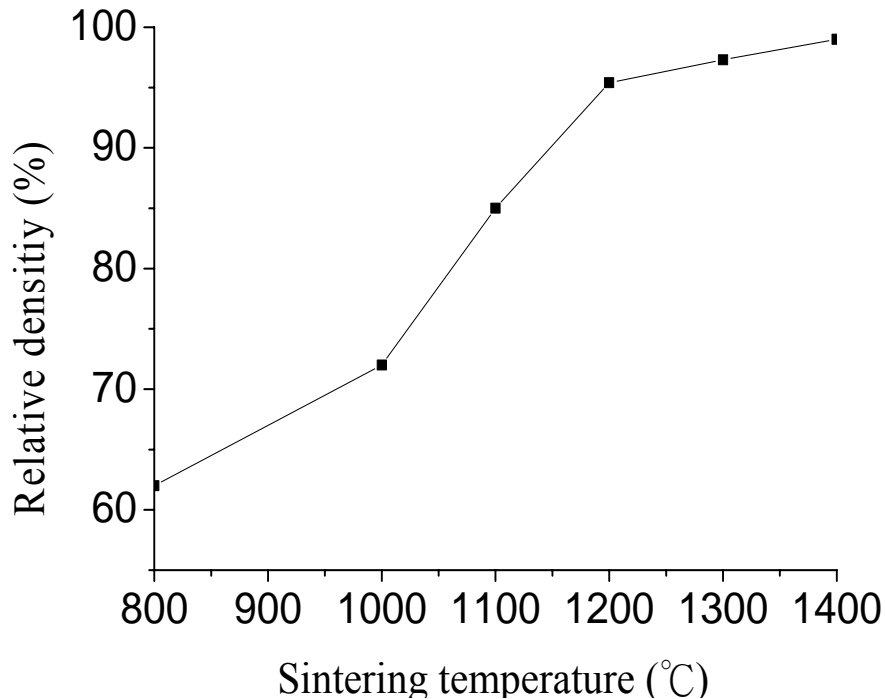
Figure 4-22. Relative density change of nano-BST samples *versus* sintering temperature.

nano-BST samples occurs at around 1200°C. Previous our study showed that the densification temperature of nano-BTO is about 1100°C (section 4-1-5) and, hence, the addition of Sr did not suppress the densification temperature of nano-BTO ceramics. This is similar to the micro-scale BST which requires a higher sintering temperature than that of conventional BTO.[19,25] However, the densification temperatures for micro-BST system could be as high as 1400°C.[19,56] Therefore, the reduction of raw powder size to nanometer scale did suppress the sintering temperatures of capacitor samples. The ignition of densification at lower sintering temperatures was attributed to the large SSA of nano-BTO/STO powders. During

sintering, the sample tended to reduce its surface energy by eliminating the total surface area of nano-particles. The interface-driven processes such as grain boundary diffusion and surface diffusion must dominate the mass transport at the early stage of sintering and result in the densification of nano-BST samples.

The SEM morphologies of nano-BST samples sintered at 1200 and 1300°C for 1, 3, 6 and 8 hrs are presented in Figs. 4-23 and 4-24, respectively. Figures 4-23(a) and 23(b) shows a rather mild grain growth in samples subjected to 1200°C-sintering for the sintering times up to 6 hrs. The grain sizes remain uniform in the range around 200 nm. However, the grain sizes rapidly enlarge to about 5.5 μm when the sintering time is raised to 8 hrs as illustrated in Fig. 23(d). As to the samples subjected to 1300°C-sintering (see Fig. 4-24), monotonous grain growth occurs as the average grain sizes increase from 220 nm for 1-hr sintering to about 45 μm for 8 hrs-sintering. Previous study reported that the average grain sizes are about 1.5 μm and 100 μm for the nano-BTO sintered at 1200 and 1300°C for 6 hrs, respectively (Section 4.1.5). This implies that the addition of Sr is able to suppress the grain growth in BTO, a result similar to that reported in micro-BST system.[57] The suppression of grain growth becomes much obvious in the specimens sintered at high temperatures, *e.g.*, 1300°C. Ionic radius of Sr^{+2} (0.113 nm) is smaller than that of Ba^{+2} (0.135 nm). As we known from the knowledge of dislocation interactions, lattice irregularity induced by the

difference of ionic radii would impinges the dislocation motions in BST lattice and hence retards the grain growth. In addition, before the grain boundaries being eliminated by substantial grain growth, numerous grain boundaries presents in the samples with nano-scale grain sizes. Grain boundary is known as the structural discontinuity, which may serves as the obstacle of dislocation motions and thus suppresses the grain growth.
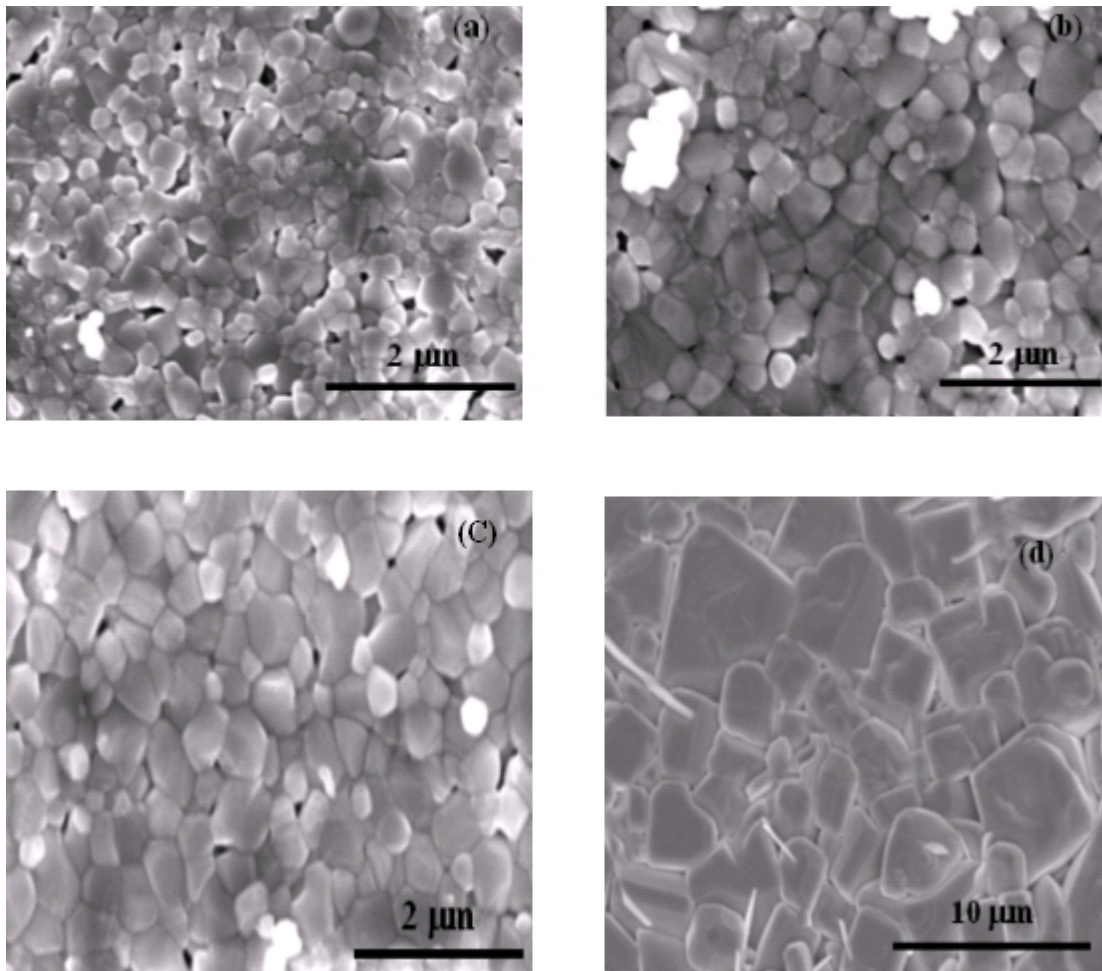
Figure 4-23. SEM micrographs of nano-BST samples sintered at 1200°C for (a) 1 hr,

(b) 3 hrs, (c) 6 hrs (d) 8 hrs.
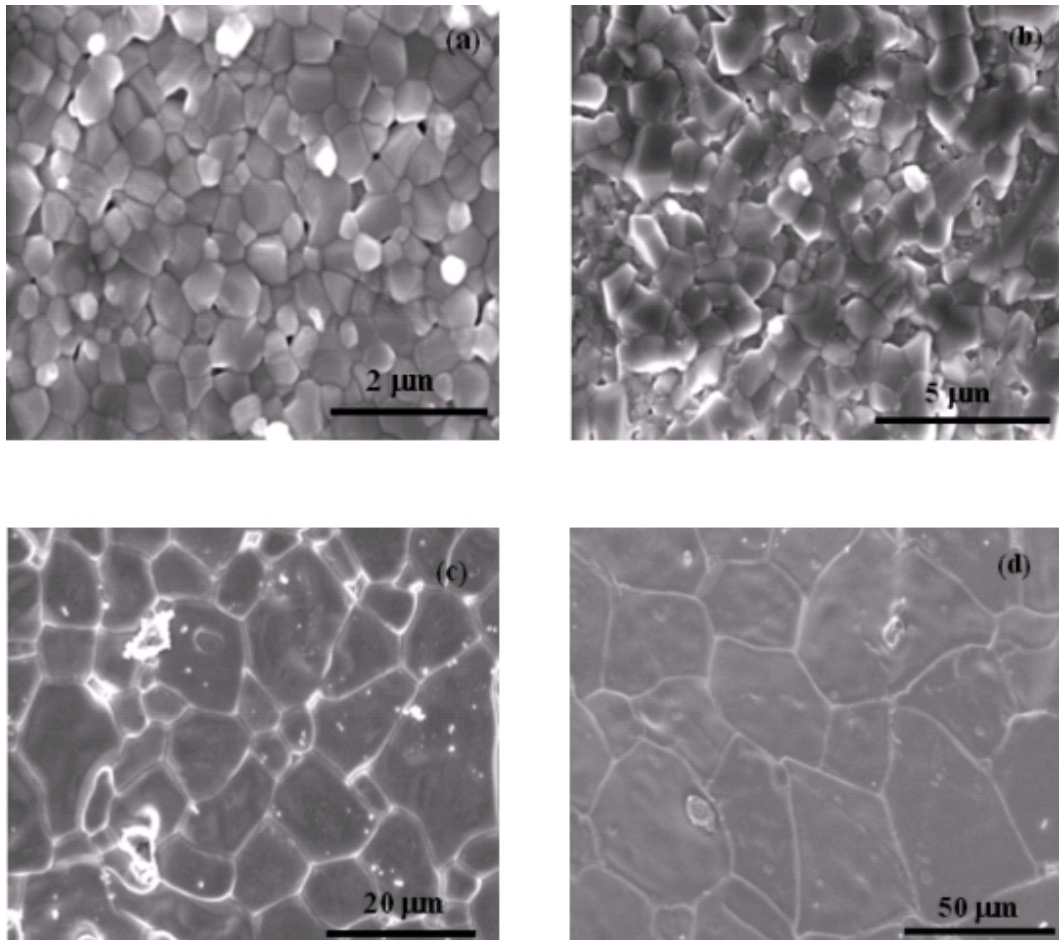
Figure 4-24. SEM micrographs of nano-BST samples sintered at 1300°C for (a) 1 hr, (b) 3 hrs, (c) 6 hrs and (d) 8 hrs.

Figure 4-25 presents the XRD patterns of the raw BTO/STO powders and the samples sintered at 1100, 1200, 1300°C for 6 hrs, respectively. It shows that the raw sample is a mixture of cubic BTO and STO powders; the sample sintering at 1100°C becomes tetragonal BST mixed with some cubic BTO/STO phases; the samples sintered at temperatures above 1200°C are all tetragonal BST. It was reported that the tetragonal phase forms in conventional BST (average grain size ≈ 10 μm) at the

temperatures as high as 1400°C.[57] Above XRD analysis indicates that in samples fabricated by using the nano-scale powders, the tetragonal phase appears at lower sintering temperatures (about 1100°C) in comparison with the conventional BST system.[58] The results above illustrate that, with specific control on sintering process, employment of nano-scale raw powders is able to secure the desired microstructure and phase constitution in the samples at lower sintering temperatures. This would be a great merit of thermal budget for device fabrication.
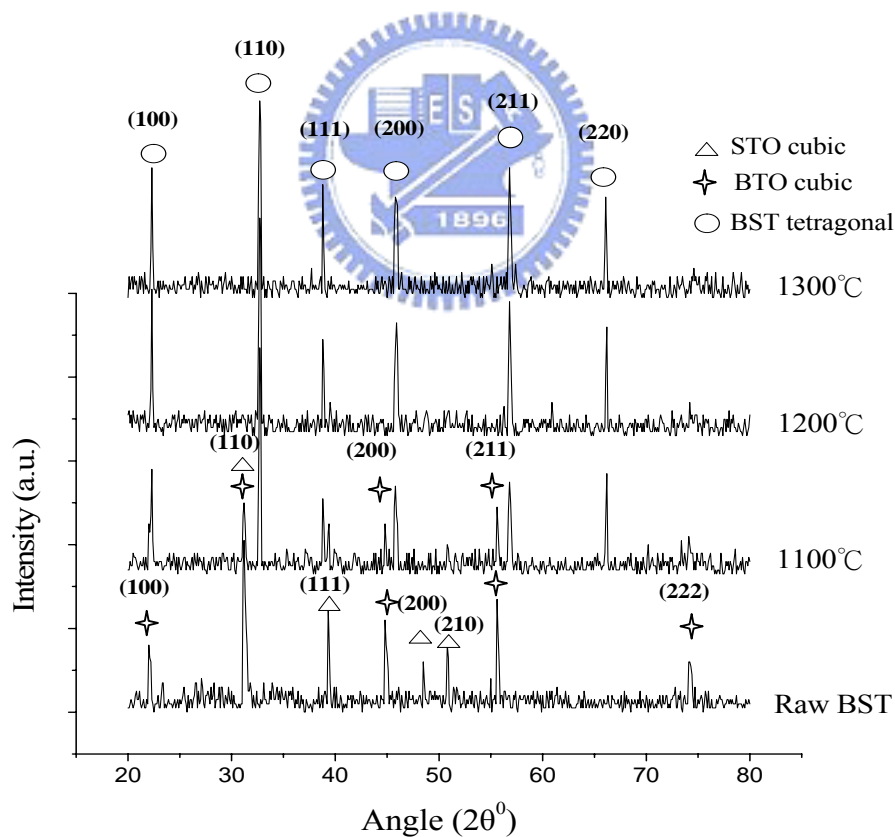
Figure 4-25. The XRD patterns for the BST sample sintered at different temperatures.

4.2.3. Dielectric Properties

Since the dielectric properties and density of ceramics are strongly related[19,25], in below only the dielectric properties of high-density (*i.e.*, greater than 95%) nano-BST samples sintered at 1200 and 1300°C are presented.

The 1-kHz dielectric constant and dielectric lose of nano-BST samples sintered at 1200 and 1300°C for different time spans are shown in Figs 4-26 and 4-27, respectively. For 1200°C-sintering, the dielectric constant increases from 8300 to 9700 with the increase of sintering times from 1 to 6 hrs, and then decreases to 6300 after 8 hr-sintering. As to the 1300°C-sintering samples, the dielectric constant monotonously decrease from 9800 to 2200 when sintering time increase from 1 to 6 hrs. The result above indicates that, *via* appropriate control of sintering conditions, high dielectric constant property could be achieved in nano-BST samples in comparison with nano-BTO (dielectric constant ≈ 8000) (Section 4.1.7) and conventional BST (dielectric constant ≈ 7200) systems[19].

Addition of Sr is known to rise the dielectric constant of BTO,[19,54] however, reduction of grain size should also play an important role on the improvement of dielectric constant of samples based on nano-scale raw powders. In conventional coarse-grained samples, each of grains is divided by several electric domains and the dipole moments corresponding to neighboring domains tend to arrange in an

anti-parallel manner (called 180°-domains).[42] It has been reported that the domain

size of BTO is known to be about 1 μm.[59] Therefore, in BST samples with grain sizes

smaller than 1 μm (*e.g.*, the samples subjected to 1200°C-sintering), each of grains

could treated as a single electric domain. Since grain boundary is the structural

discontinuity, the coupling between adjacent electric dipoles in the samples with fine

grain structure becomes weaker and, hence it is comparatively easy for the electric

dipoles to align in parallel manner when external bias is applied. This implies a higher

net electric polarization and thus the high dielectric constants in the samples with fine

grain structure.[54]

In conjunction with the SEM observations shown in Figs. 4-23 and 4-24, the

results above clearly illustrate that in addition to the fine grain sizes, a

high-density/low-void content structure is essential to accomplish satisfactory

dielectric properties in BTO and related ceramics.[19,25] This iterates the importance on

the control of sintering process to achieve desired phase and microstructure in the

samples based on nano-ceramic powders.
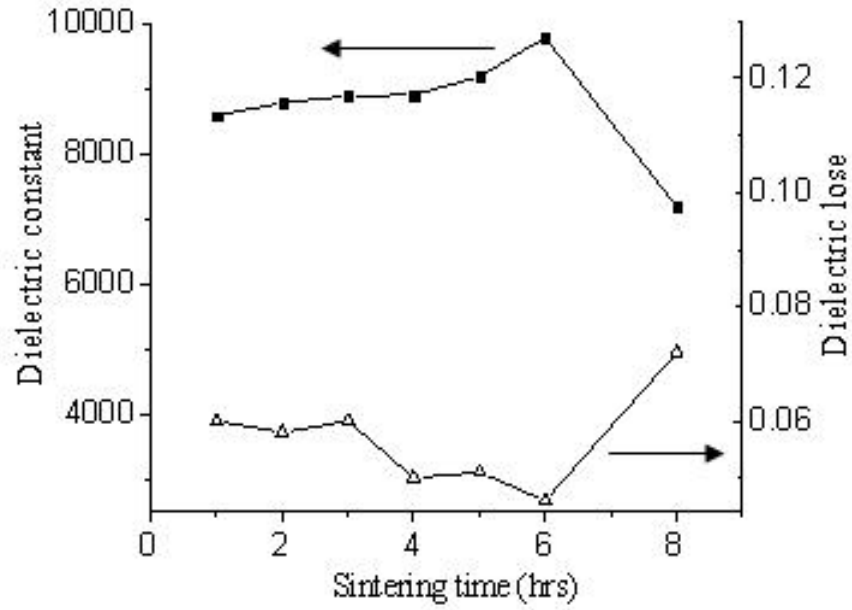
Figure 4-26. 1-kHz dielectric constant and dielectric loss of nano-BST samples

sintered at 1200°C *versus* sintering time.
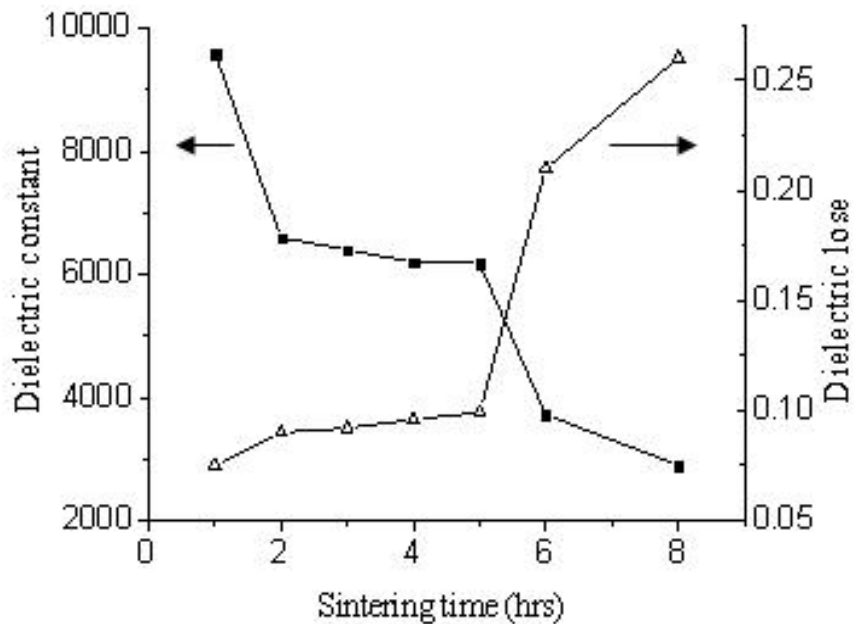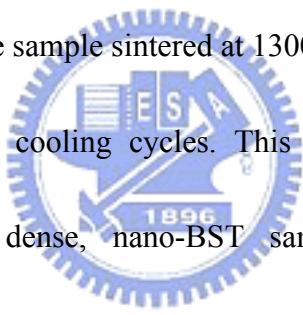
Figure 4-27. 1-kHz dielectric constant and dielectric loss of nano-BST samples

sintered at 1300°C *versus* sintering time.

4.2.4. Characterization of T_C

STO is usually added in BTO in order to shift the T_C to lower temperatures and it is well known that the T_C of BTO decreases linearly with amount of STO in BTO.[54] Figure 4-28 shows the variation of dielectric constants of BST samples sintered at 1200 and 1300°C for 1 hr as a function of temperature during a heating cycle and a cooling cycle. The grain sizes of the BST sample sintering at 1200°C and 1300°C for 1 hr are about 200 nm and 220 nm, respectively. It is found that the T_C corresponding to the heating and cooling cycle is about 36°C and 33°C for the BST sintered at 1200°C, respectively. As to the sample sintered at 1300°C, the T_C's are about the same at 25°C for the heating and cooling cycles. This indicates a negligible thermal hysteresis of T_C's in the dense, nano-BST samples studied in this work. Stress/strain-induced phase transitions such as martensite transformation is commonly characterized by the hysteresis of transition temperature. Lack of thermal hysteresis in nano-BST sample hence implies that the minor effect of stress/strain energy term on the transition. Further, the effect of volume free energy term is ruled out since the phase transition of BST samples at T_C involves no composition change. According to the theory of phase transitions in solids, interfacial energy term would dominate the transition and thus the presence of grain boundaries in fine-grained BST samples should play a important role in the phase transition of BST at T_C.

Previous studies reported that the T_C of micro-BTO is about 130°C.[19] In addition

to the suppression of T_C by adding Sr into BTO, the results above also illustrate that

the reduction of grain size in the nano-BST achieves lower T_C's in comparison with

conventional BST whose T_C is about 50°C.[54] It is known that the lattice of BST

switches from cubic to tetragonal structure when the paraelectric-to-ferroelectric

transition occurs at T_C. Internal stresses are built up in the samples when crystal

structure changes and somehow they must be eliminated so that the phase transition

may proceed. However, the stress relaxation *via* the presence of 90°-domain is no

longer applicable to the nano-BST sample with grain size $\leq$ 1 μm. It is hence

speculated that the fine grain structure in nano-BST samples provides numerous grain

boundaries for stress relaxation. Besides, grain boundaries are known as the

preferential sites for heterogeneous nucleation and fine grain sizes effectively shorten

the distance of atom rearrangement during phase transition. From these reasons, it

should be easier to initiate the phase transition in nano-BST samples and hence the

lower T_C's were observed.
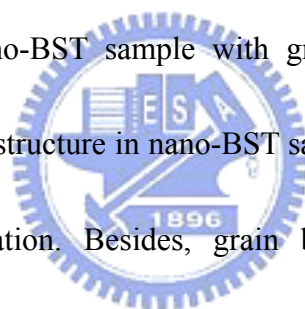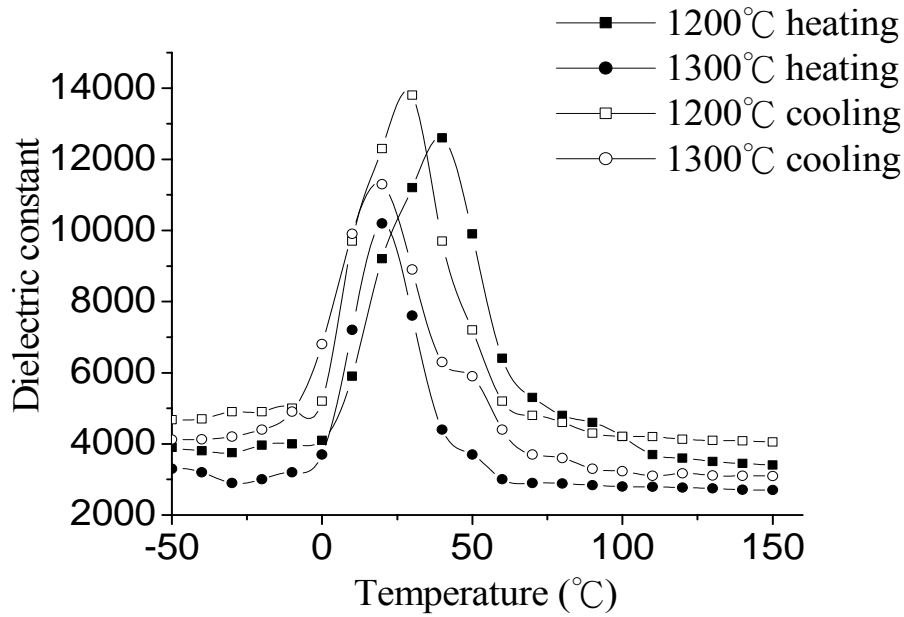
Figure 4-28. The dielectric constants of BST sample sintered at 1200 and 1300°C for

1 hr as a function of temperature.

4.3. Preparation and Characterizations of La-doped BST Ceramics

Previous results show that the dielectric constant of nano-BST is higher than that

of conventional BTO and BST systems. However, the dielectric loss of nano-BST is

comparatively high. In order to improve this disadvantage, we dope the La_2O_3 in BST

samples (called LBST samples hereafter) and investigate its dielectric properties

relation to microstructure and phase transformation.

4.3.1. Dispersion and Preparation of LBST Samples

In order to avoid the agglomeration caused by van der Waals attraction resulted

from large SSA of nano-sized particles, the ceramic powders must be dispersed before

sintering.[18] Viscosity of 1.0LBST (the number appearing in front of LBST represents

the molar ratio of La_2O_3 added in BST) slurry as a function of PMAA amount is

presented in Fig. 4-29. It can be seen that at first the viscosity sharply decreases with

the increase amount of chemical dispersant, reaches the lowest value at 3 *wt*.%, then

increases with further increase of chemical dispersant concentration. The lowest

viscosity indicates the finest dispersion of powders in slurry. Similar results were

observed in other *x*LBST slurries and hence it is concluded that the optimum content

of PMAA chemical dispersant = 3 *wt*.% for the dispersion the nano-scale LBST

powders. By the way, in this study, the LBST materials must be prepared by premix

via laboratory mill with an amphibious chemical dispersant (PDAAE). The reason is

that PDAAE molecules have more steric effects and stabilize the BST mixed slurry in

a cloudy longer. In addition, a differential chemical dispersant (PMAA) has also been

used to disperse and prepare LBST mixed slurries. Compared with PDAAE, PMAA

molecules are anionic polyelectrolytes which would cause electrostatic repulsions to

enhance dispersion and decrease viscosity of LBST mixed slurries.

Figure 4-30 shows the particle size distribution of various *x*LBST slurries. The

d_{50}'s of aqueous suspensions are 72, 70, 67 and 69 nm for BST, 0.5LBST, 1.0LBST

and 1.5LBST slurries, respectively. Furthermore, the sharp, narrow shape of
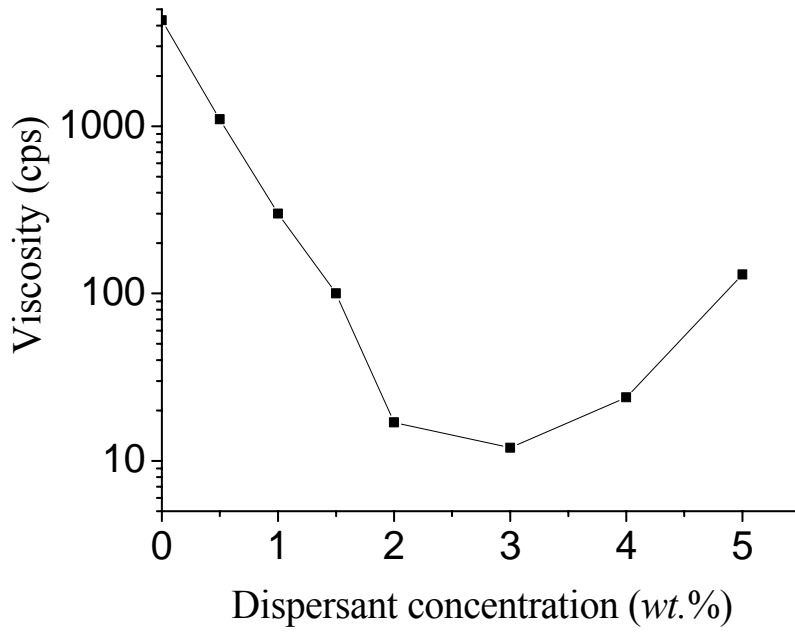
Figure 4-29. The effect of dispersant concentration on the viscosity of 1.0LBST

suspensions subjected to various grinding/mixing processes.
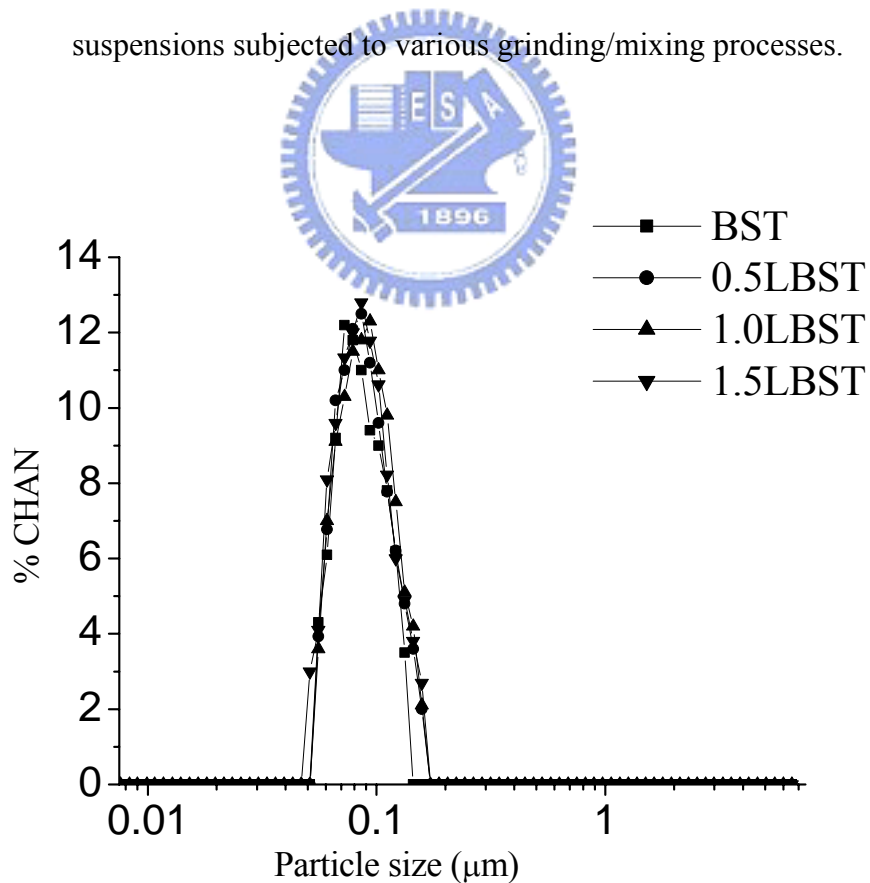
Figure 4-30. Particle size distribution of nano-xLBST powder in the slurry subjected

to chemical dispersion and physical grinding process.

distribution curves implies not only the uniform particle size in *x*LBST slurries, but also the success of nano-scale powders dispersion *via* the methodology described above.

4.3.2. Sintering Behaviors and Microstructure Evolution

Figures 4-31 presents the relative densities of BST and *x*LBST samples sintered at various temperatures for 1 hr. It can be seen that at the same sintering temperature the density of sample decreases with the increase of La content. When sintered at 1400°C, the samples with La$_2$O$_3$ content > 1.0 *mol*.% (*e.g.*, 1.5 LBST sample) cannot reach the satisfactory densification (*i.e.*, relative densities > 90%).

Figure 4-32 shows the average grain sizes of BST and *x*LBST samples as a function of sintering temperature deduced from SEM characterization. It can be seen that with the increase of sintering temperature, grain enlargement in the samples becomes obvious; however, the grain size increment is suppressed with the increase of La content. An illustration of above results is given in Figs. 4-33(a)-4-33(d) which depicts the SEM morphologies of BST and *x*LBST samples sintered at 1400°C for 1 hr. The BST and 0.5LBST samples exhibit highly dense sintered structures with few pores at grain boundaries; nevertheless, their grain sizes exceed micrometer scale. The 1.5LBST sample contains numerous pores in the sintered body and its density remains
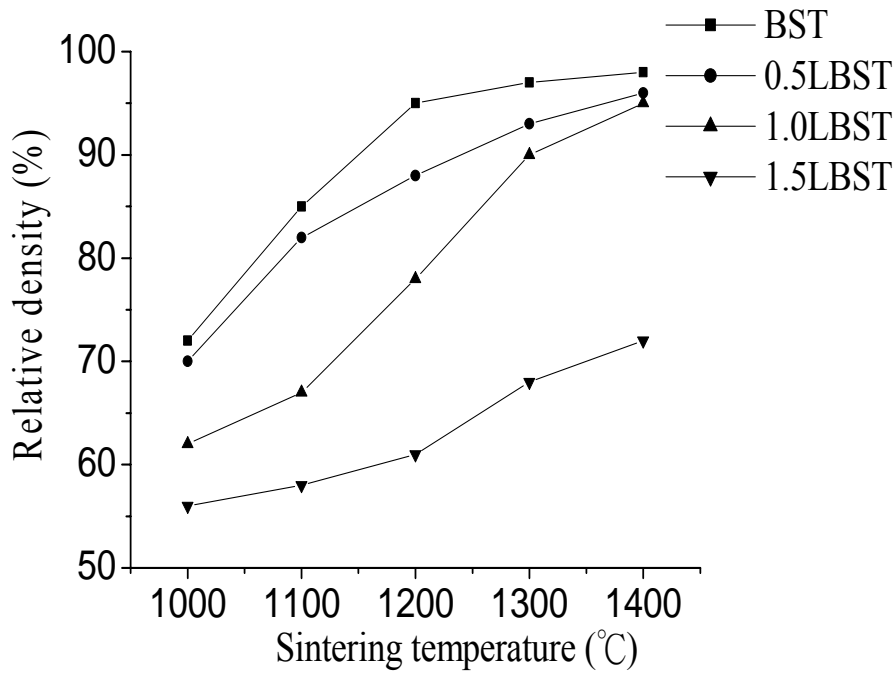
Fig. 4-31. Relative densities of BST and *x*LBST samples sintered at various

temperatures for 1 hr.
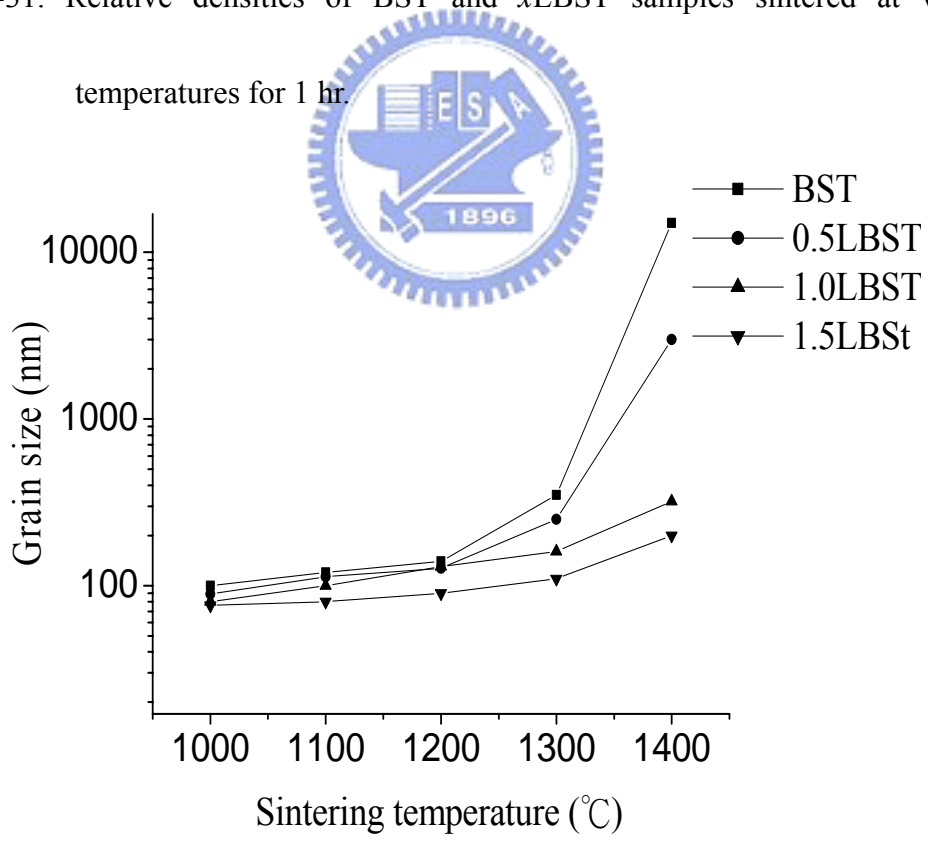
Fig. 4-32. Average grain sizes of the BST and the LBST samples as a function of

sintering temperature deduced from SEM observation.

low at 70% although it exhibits extremely fine grain size about 100 nm after the 1400°C-sintering. As to the 1.0LBST sample, it simultaneously accomplishes the satisfactory densification ($\approx$ 95%) and fine grain structure ($\approx$ 200 nm) *via* 1400°C/1 hr-sintering.

The study on conventional BST sample reported that it requires 1400°C sintering for 1 hr to reach densification and the grain size is about 10 μm.[19,54] As to the BST and BTO samples prepared on the base of nano-scale powders, they respectively possess the average grain sizes about 50 and 150 μm when sintered at 1400°C for 1 hr. The results presented in Figs. 4-31 and 4-32 clearly indicate that doping of La_2O_3 in BST may effectively suppress the grain coarsening during sintering. However, the La-doping also raises the densification temperature of nano-BST ceramics as revealed by Fig. 4-33.

Figures 4-34(a) and 4-34(b) present the TEM micrographs of 0.5LBST and 1.0LBST, respectively. The concentrations of Ba, Sr, Ti and La elements in grain center and at grain boundary for 0.5LBST and 1.0LBST samples obtained by EDX analysis are listed in Table 4-4. The TEM images shown in Figs 4-34(a) and 4-34(b) reveal a uniform granular microstructure in both LBST samples and the grain sizes are in consistent with those obtained by SEM observations (*e.g.*, Figs. 4 and 5). As to the element concentrations, the data listed in Table 4-4 indicate that the La element
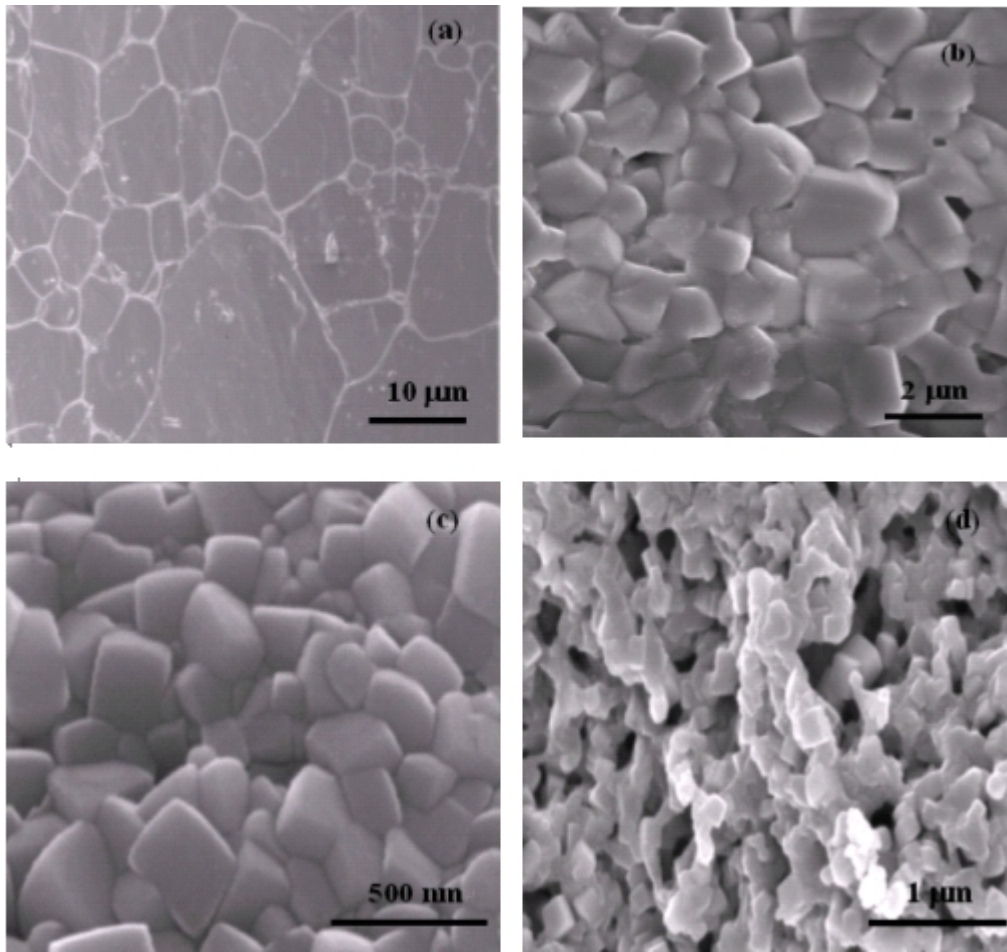
Figure 4-33. SEM micrographs of BST samples doped with: (a) BST (b) 0.5LBST (c).

1.0LBST (d) 1.5LBST sample subjected to 1400°C/1-hr sintering.

tends to segregate at the grain boundaries. It is proposed that the donor dopants

segregated at grain boundaries reduce the mobility of boundaries and effectively

inhibit grain growth during sintering process.[59,60] The TEM/EDX analysis presented

above clearly evidence (from Table 4-4) the segregation of La element at grain

boundaries. It hence restrains the grain growth during sintering and thus the LBST

samples exhibit finer grain sizes in comparison with BST sample sintered at the same

94

sintering conditions.
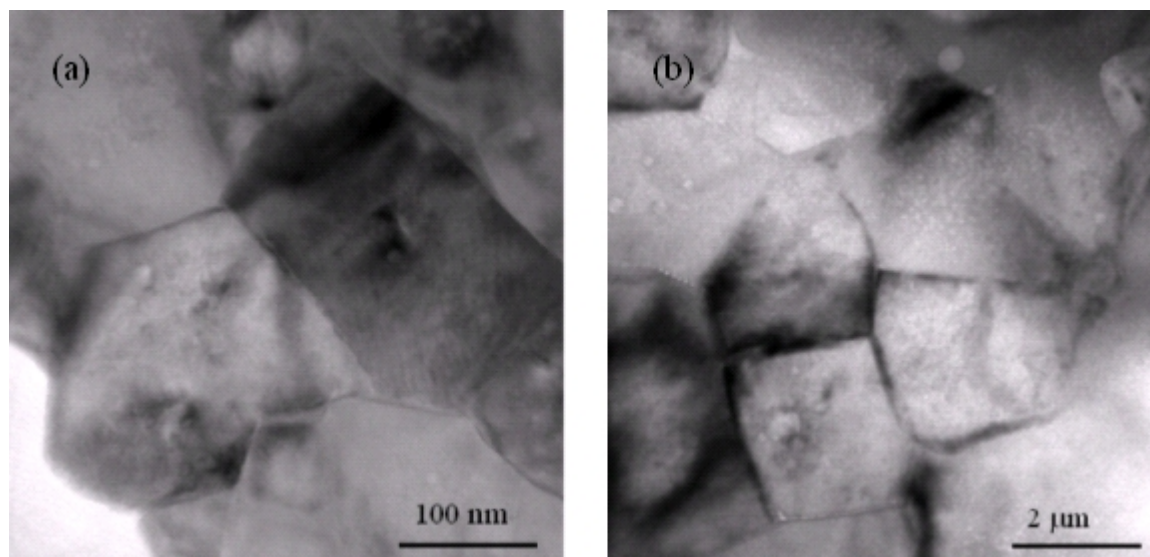
Figure 4-34. TEM micrographs of (a) 1.0LBST (b) 0.5LBST subjected to 1400°C/1-hr

sintering.
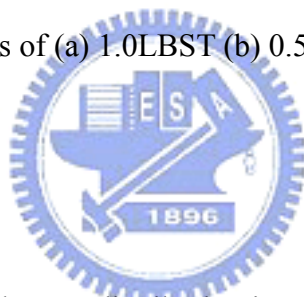
Table 4-4. Element distribution in xLBST sample.

Sample	Element	In grain center (*wt.*%)	At grain boundary (*wt.*%)
0.5LBST	Ba	45.2	44.8
	Sr	12.3	12.6
	La	0.52	0.66
	Ti	21.3	21.9
1.0LBST	Ba	43.9	44.3
	Sr	12.1	12.4
	La	0.92	1.37
	Ti	22.6	21.4

Figure 4-35 presents the XRD patterns of the raw La_2O_3/BTO/STO powder

mixtures and the xLBST samples sintered at 1400°C for 1 hr, respectively. It shows

that the raw powders of BTO, STO and La_2O_3 are all of cubic phases. After the 1400°C/1-hr sintering, the xLBST samples all become tetragonal BST phase. The missing of La_2O_3 peak indicates that La_2O_3 are completely soluble in BST, which is in consistent with the TEM/EDX analysis presented above as well as the results reported by previous study[61]. The ionic radius of La^{+3} (0.115 nm) is smaller than that of Ba^{+2} (0.135 nm) and about the same as that of Sr^{+2} (0.113 nm), hence the relatively small amount of La_2O_3 (< 3 wt.%) may completely dissolve in BTO at high sintering temperatures (> 1300°C).[61]

The XRD analysis for 1.0LBST samples sintered at various temperatures was also carried out so as to explore the evolution of phase constitution during the sintering of nano-scale ceramic powders. The XRD patterns presented in Fig. 4-36 indicates that sintering at temperatures greater than 1200°C is required to yield the tetragonal BST solid solution phase. It has been reported that sintering temperatures as high as 1500 and 1400°C are respectively required to form tetragonal phase in conventional BTO samples doped with La_2O_3.[61] Hence the reduction of raw powder sizes to nanometer scale indeed provides a viable way to secure desired phase structure at lower sintering temperatures.
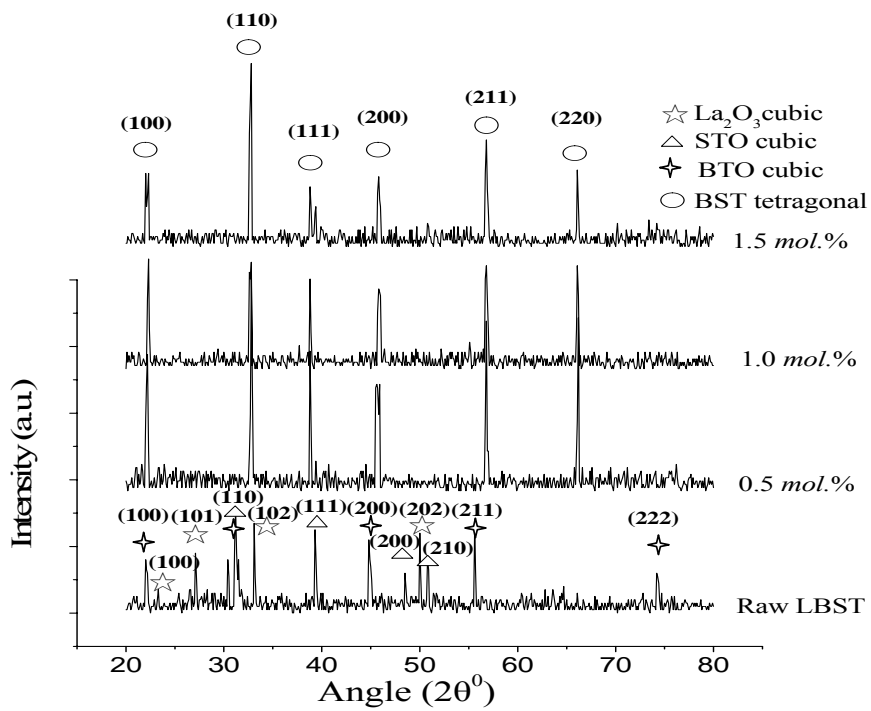
Figure 4-35. XRD patterns for raw powders and xLBST samples sintered at 1400°C
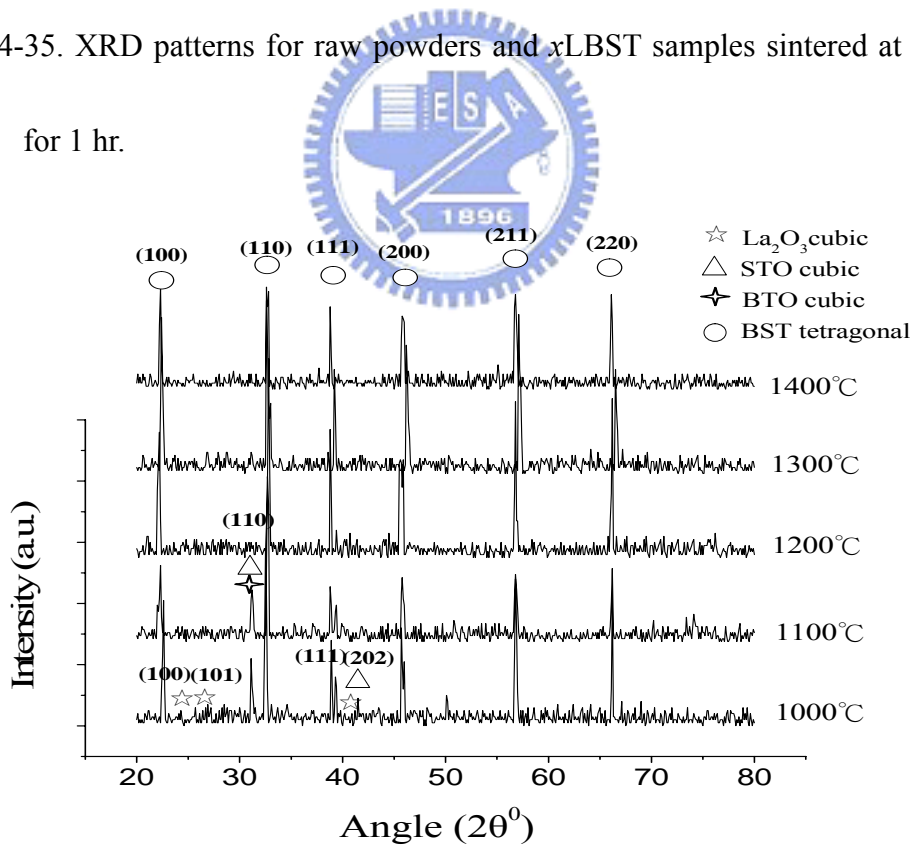
for 1 hr.

Fig. 4-36. XRD patterns for 1.0LBST sample sintered at different temperatures.

TEM image and diffraction pattern of 1.0LBST sample sintered at 1400°C for 1 hr are presented in Figs. 4-37(a) and (b). The analysis of selected area electron diffraction (SAED) pattern shows that such a sample possesses the same tetragonal structure as in BST as revealed by XRD. Besides, SAED patterns does not show the existence of second phases, which is in good coincidence with the result of XRD analysis.
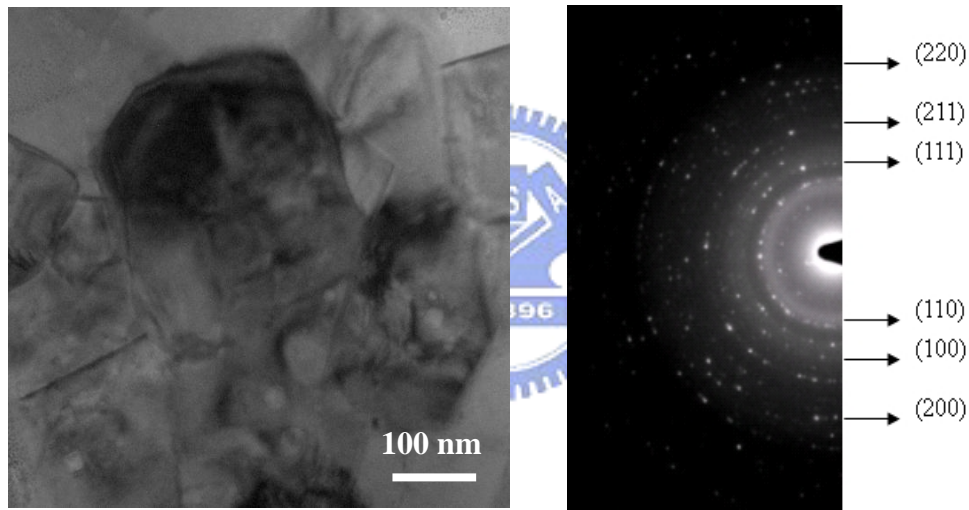
Figure 4-37. (a) TEM image and (b) SAED pattern of 1.0LBST sample sintered at 1400°C for 1 hr

4.3.3. Dielectric Properties

In below, only the dielectric properties of 1.0LBST sample are presented since it is the sample that may achieve the satisfied densification with fine grain size. The 1-kHz dielectric constants and dielectric losses of 1.0LBST samples sintered at 1000

to 1400°C are presented in Fig. 4-38. It can be seen that with the increase of sintering temperature, the dielectric constant increases from 1730 to 13800 while the dielectric loss decreases from 0.32 to 2.8×10^{-4}. As shown in Figs. 4-31 and 4-32, relative density and grain size increase with sintering temperature and, therefore, to achieve high densification density without substantial grain enlargement is crucial to preserve the dielectric properties of capacitor samples prepared based on nano-ceramic powders.

Since the ionic radius of La^{+3} is comparatively similar to those of Ba^{+2} and Sr^{+2} and larger than that of Ti^{+4} (0.068 nm), the La^{+2} would thus occupy Ba^{+2}/Sr^{+2} sites in BST. The associated defect reaction can be expressed as:

$$La_2O_3 \xrightarrow{\text{BST}} 2La^{\bullet}_{Ba/Sr} + V''_{Ba/Sr} + 3O_O. \qquad (4\text{-}4)$$
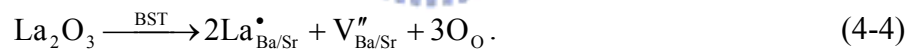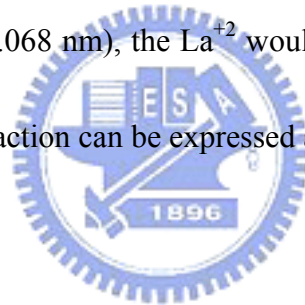
Above reaction depicts the formation of Ba^{+2}/Sr^{+2} site vacancies, $V''_{Ba/Sr}$, induced by the doping of La_2O_3. Previous TEM/EDX analysis revealed the segregation of La at grain boundaries, it is hence speculated that more $V''_{Ba/Sr}$ would residue in the vicinity of grain boundaries which, in turn, benefits the mobility and induced dipoles and thus amplify the dielectric constant property. Meanwhile, the distortion of BST lattice caused by the difference of ionic radii and doping of aliovalent impurity (*i.*e.,

La^{+3}) somehow may contribute to the increase of polarization. Previous studies further demonstrated that the capacitor samples with nano-scale granular structures possess higher dielectric constants in comparison with samples with micro-scale granular structures due to the existence of numerous interfaces that effectively promote the mobility and induced dipoles when external bias is applied.[18,19] The reasons cited above explain the high dielectric constant property observed in 1.0LBST capacitor sample.

Dielectric property measurement also revealed that dielectric loss of 1.0LBST (loss = 2.8×10^{-4}) is lower than that of nano-BST sample (loss = 10^{-2}). In addition, the resistance of 1.0LBST is 4×10^{6} Ω which is lower than nano BST sample (3×10^{8} Ω). This is good sufficient evidence to prove that La$_2$O$_3$ dopant can induce dipole; and further, decrease resistance of BST sample. Besides, the dielectric loss is a lose energy and come from dipole motion. So, the lose energy must be small when dipole move easily. From this point of view, we can understand that dielectric loss of 1.0LBST is lower than nano-BST sample.
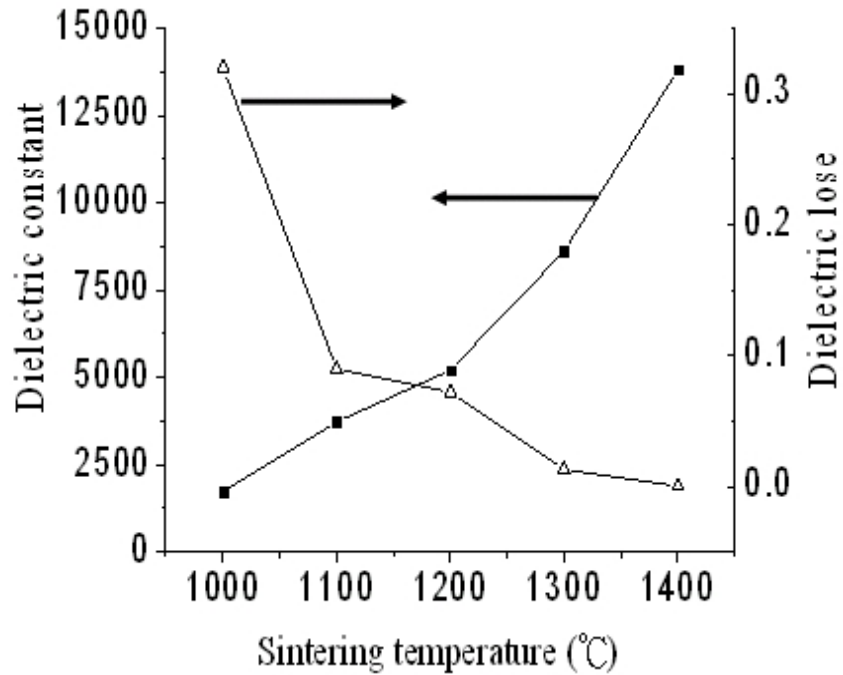
Figure 4-38. 1-kHz dielectric constant and dielectric loss of 1.0 LBST samples

sintered at *versus* sintering temperature.

4.3.4. Characterization of T_C

Figure 4-39 plots the 1 kHz dielectric constant *vers*us temperature for xLBST

samples. The T_C decreases from 50°C for the sample free of La_2O_3 to 25°C for the

BST samples doped with 1.0 *mol*.% La_2O_3. The result illustrates that the 1.0LBST

exhibits lower T_C's in comparison with conventional BST whose T_C is about 50°C.[54] It

is well known that T_C is a critical temperature which the lattice of BST switches from

cubic to tetragonal structure when the paraelectric-to-ferroelectric transition. In this

study, the nano 1.0LBST sample has many grain boundaries and the grain boundaries

are known as the preferential sites for heterogeneous nucleation and fine grain sizes

effectively shorten the distance of atom rearrangement during phase transition. In

addition, grain boundary can relax inter stress and shift T_C to lower temperature. For

reasons mentioned above, nano LBST sample has a lower T_C than micro BST sample.

Furthermore, T_C of nano 1.0LBST and nano BST in our previous study were similar

(section 4-2-4). Nano LBST and BST have lower T_C than that of micro BST,

conclusively nano grain does reduce T_C in BST sample.
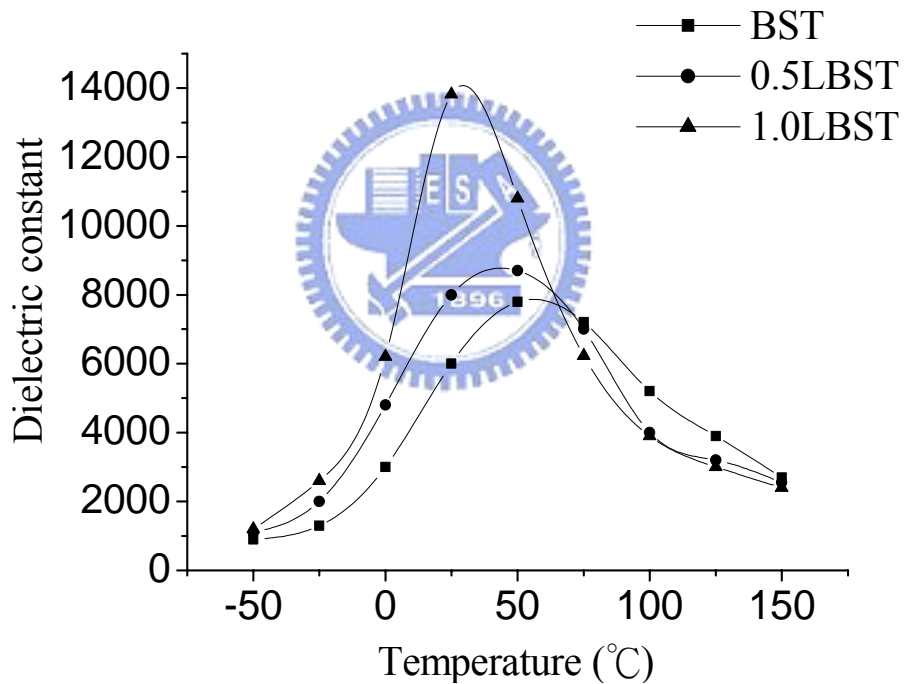
Figure 4-39. The dielectric constants of LBST sample sintered at 1400°C for 1 hr as a

function of temperature.

4.4. Dispersion of CNTs and Its Application to LiCoO$_2$ Electrode in LIBs

4.4.1. Monomer Synthesis

Preparation of monomer, compound **3**, is illustrated in Scheme 3-1. Nucleophilic substitution of the nitro function of 4-nitrophthalonitrile with the 4-[di(4-aminophenyl)- methyl]phenol in a K$_2$CO$_3$/DMF medium yields compound **1**.[62] Alkaline hydrolysis of compound **1** in KOH$_{(aq)}$/ethanol produces compound **2**, which was subsequently dehydrated with acetic anhydride to form the monomer compound **3**. The positions of the chemical shifts for protons in compound **3** obtained from ^{1}H-NMR spectrum are showed in Fig. 4-40. ^{1}H-NMR (DMSO-d_6): δ(ppm) = 5.22 (s,2H), δ(ppm) = 6.51 (d,4H), δ(ppm) = 6.74 (d,4H), δ(ppm) = 7.10 (d,1H), δ(ppm) = 7.33 (d,1H), δ(ppm) = 7.93 (d,1H). In addition, precise mass of compound **3** was determined by mass spectrometry. Mass [M+]: 436.0209. Calculate 436.0219 for C$_{27}$H$_{20}$N$_2$O$_4$.[63]

4.4.2. PEI Synthesis and Characterizations

The PEI was synthesized by the self-polycondensation process which starts from the reaction of monomer **3** in NMP to from the amic acid. As shown in Scheme 3-2, the one-step polymerization was carried out at 120°C for 4 hrs using TPP/pyridine as the condensation agents. The ^{1}H-NMR and FTIR spectra for PEI structure
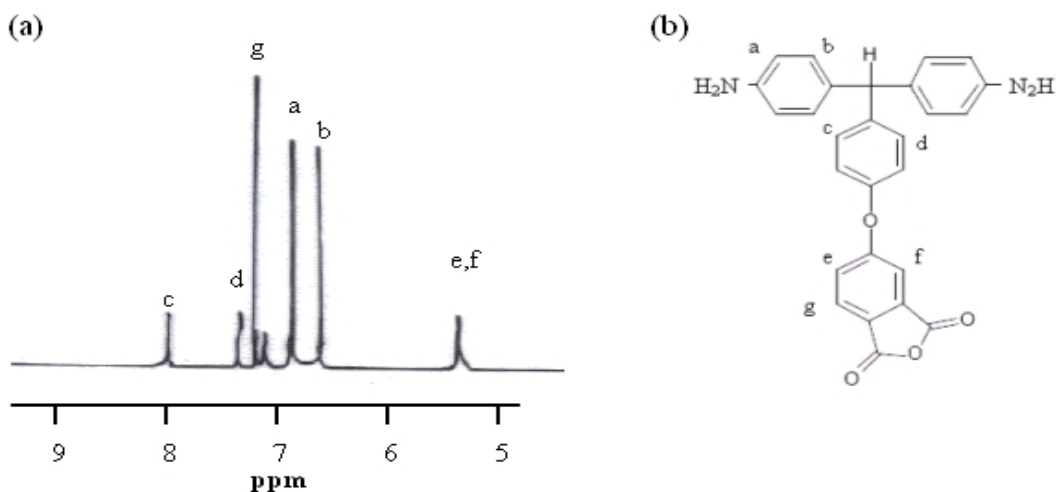
Figure 4-40. (a) ^{1}H-NMR spectrum, and (b) molecule structure of compound **3**.

characterization are shown in Figs. 4-41 and 4-42, respectively.[64,65] In the ^{1}H-NMR

spectrum, the resonance of the proton of the amide group appears at 2.6 ppm. In

addition, the resonances at 6.6, 6.8 and 7.4 ppm correspond to the proton of the

terminal, linear and dendritic subunits in the hyperbranched polymer, respectively.[66]

In the FTIR spectra, the polymer exhibits characteristic carbonyl absorptions

corresponding to an imide ring at 1716 and 1772 cm^{-1} (C=O symmetric stretching) in

addition to the typical aromatic-imide C-N stretching at 1373 cm^{-1}. Furthermore, the

aromatic stretching of the amide group appears at 1665 cm^{-1}. The broad bands

between 2500 and 3500 cm^{-1} are attributed to amide N-H and N-H$_2$. As determined by

GPC method, the average molecular weight of hyperbranched PEI was found to be

54000.

104
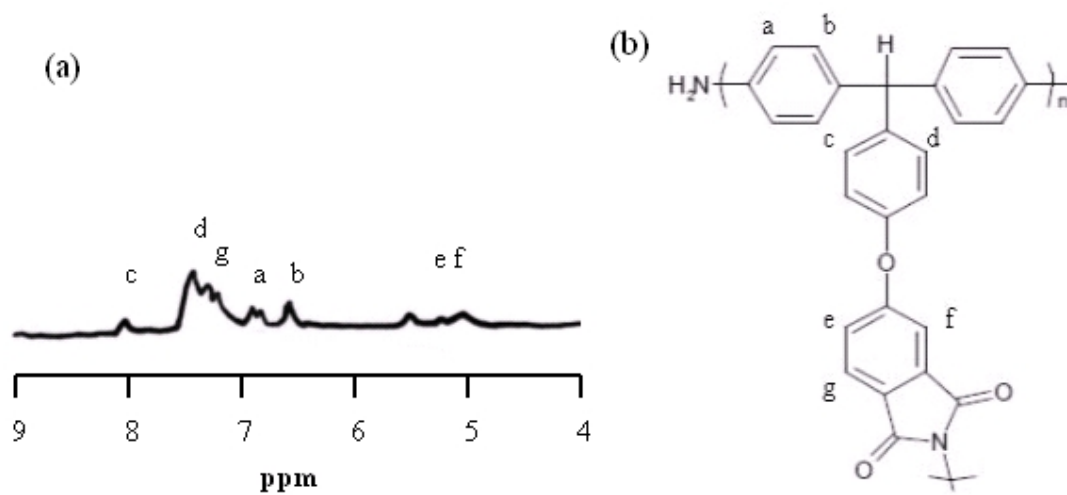
Figure 4-41. (a) ^{1}H-NMR spectrum, and (b) molecule structure of PEI.
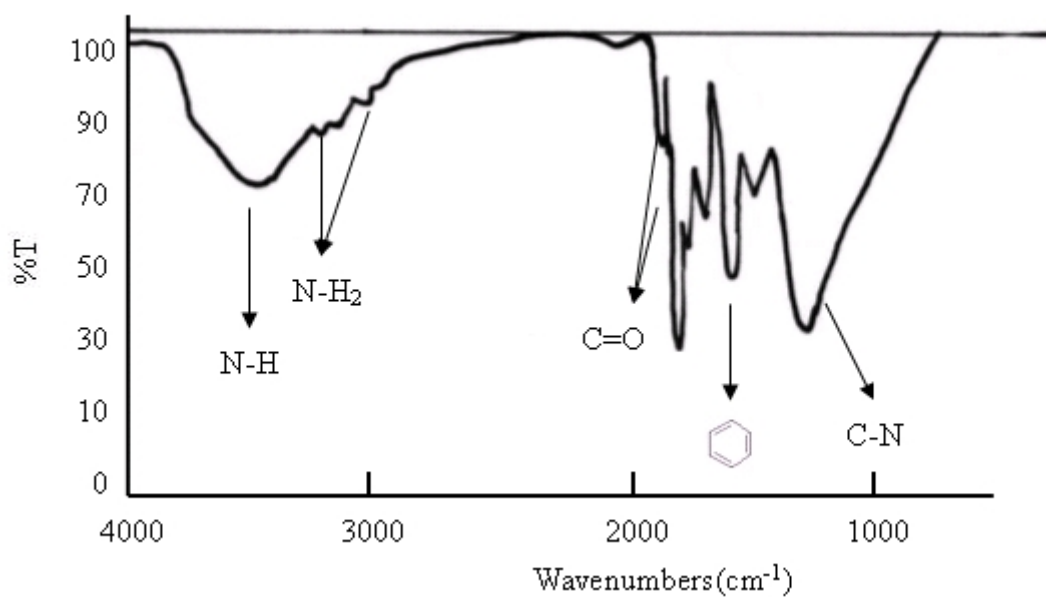
Figure 4-42. FTIR spectra of PEI.

4.4.3. Adsorption Isotherm

Figure 4-43 shows the amount of PEI adsorbed on CNTs as a function of the initial PEI concentration. It can be seen that the amount of adsorbed PEI first

increases with the increase of PEI concentration, then reached a plateau value when

PEI concentration exceeds about 3 *wt*.%. The isotherm depicts the high-affinity

characteristics, as indicated by the rapid increase of the adsorbed amount at low PEI

concentrations. Previous studies reported that the electrostatic interactions between

the oppositely charged electrolyte and the powder enhance the adsorption of

polyelectrolyte dispersants.[4] In this work, PEI and CNT are both electro-neutral and

the increase of adsorption is owing to the large surface area and porous structure of

CNTs. In addition, the adsorption of PEI may take place *via* chemical interactions

(dipole-induced interactions) or hydrogen bonding. It is known that the CNT can

adsorb hydrogen atoms on its surface.[54] As a result, hydrogen bonding may form *via*

the interactions of hydrogen atoms on CNTs and the nitrogen atoms in PEI.

Furthermore, the PEI is a hyperbranched polymer that may enhance the loop

formation in adsorbed configuration. This results in a dense packing of dispersants on

CNT surface and promotes steric effect.[4]

Quantitative determination of PEI adsorption on CNT was carried out by the

analysis of data presented in Fig. 4-44 in terms of the Langmuir adsorption equation

(*i.e.*, Eq. (4-3)). The plot of *Ce/As versus Ce* for this type of suspension is presented in

Fig. 4-43. Straight line shown in Fig. 4-44 indicates the Langmuir monolayer

adsorption behavior. The slopes of the straight lines represent the reciprocal of the
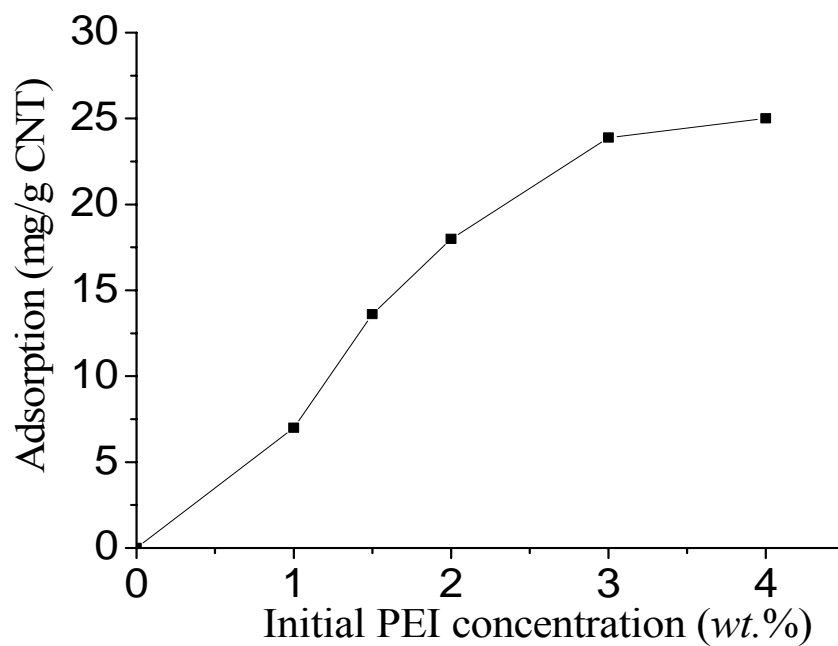
Figure 4-43. The adsorption amount of PEI on CNT as a function of the initial PEI concentration.
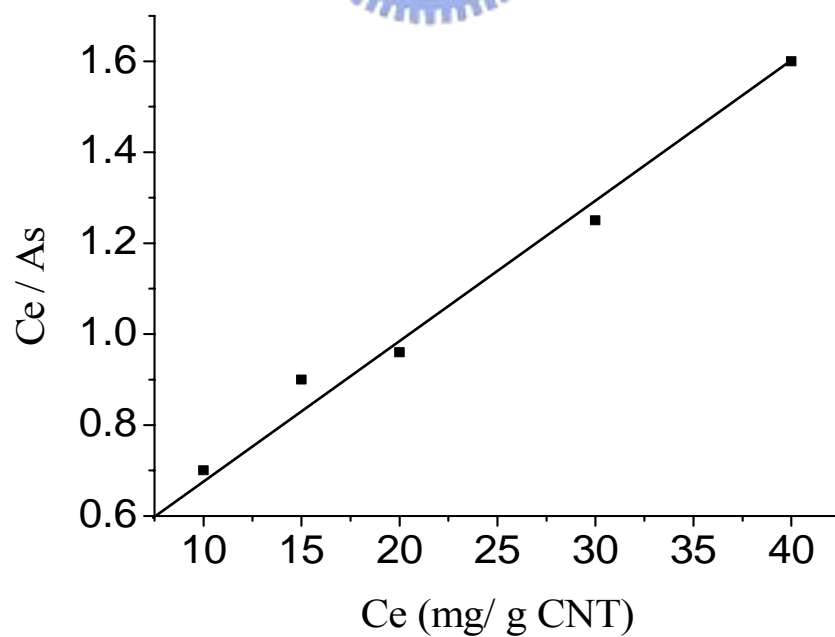
Figure 4-44. Plot of Fig. 4-43's data in terms of the Langmuir adsorption analysis.

monolayer adsorption of dispersant (1/*Cm*) and the value of *Cm* was found to be 24.6

mg/g CNT as calculated from the plot above.

4.4.4. Rheological Behaviors

Figure 4-45(a) presents the shear rate dependence of steady-state viscosity of the

CNTs slurries containing various amounts of PEI. The result for CNTs slurry free of

PEI is not shown because its sediment rate was so high that it exceeds the steady-state

viscosity detection limit. Figure 4-45(a) depicts that, regardless of the PEI contents,

the viscosity of CNTs slurry first decreases dramatically when shear rate is increased.

Afterward, the viscosity of CNTs slurry gradually reaches a plateau value when shear

rate is further increased. Such a shear thinning behavior and its correlation with the

viscosity of slurry have been reported previously.[68-69] When the shear force is exerted

on slurry, it breaks the agglomerates in slurry and the sizes of agglomerates reduce

with the increase of shear rate. Hence, the viscosity decrease behavior depicted in Fig.

4-45(a) is ascribed to the size decrease of CNTs agglomerates in slurries when shear

rate is increased.

In addition to the shear-thinning behavior described above, Fig. 4-45(a) reveals

that the viscosity level of CNTs slurries decreases when PEI concentration increases

from 0.5 to 2.0 *wt.*%. Further increase of PEI concentration raises the viscosity level

of CNTs slurries. The critical amount of PEI to achieve the colloid stable state in slurries is thus about equal to 2.0 *wt.%*, which is consistent with the results obtained by adsorption isotherm analysis. It is noted that such a critical PEI content also implies the occurrence of mono-layer coverage of dispersant on CNTs. When PEI concentration exceeds 2.0 *wt.%*, the slurries change from stabilization to flocculation that the excessive PEIs act as the free solute in the slurries and thereby results in the increase of viscosity. In addition, the excessive PEIs may also bridge with each other to induce the CNT agglomerations and raises the viscosity.[69]

Figure 4-45(b) shows the shear rate dependence of thixotropic-state shear stress for CNTs slurries without and with 2.0 *wt.%* PEI. In the slurry free of PEI, an obvious hysteresis presents in the plot of shear stress *versus* strain rate, indicating such slurry behaves as a clay suspension. As to the CNTs slurry with 2 *wt.%* PEI, its route is similar regardless of the routes of shear rate and hence it is a shear thinning fluid. This also illustrates that CNTs is well dispersed by 2 *wt.%* PEI in the slurry.

As described previously, dispersion of CNTs *via* the electrostatic and/or electrosteric mechanisms is unlikely since the hydrophobic feature of NMP inhibits the dissociation of polyelectrolyte dispersants. One of the purposes of PEI synthesis is to generate a highly branched structure so that when adsorbs on CNTs, it may provide the steric mechanism for dispersion. In addition, the aromatic-imide group in
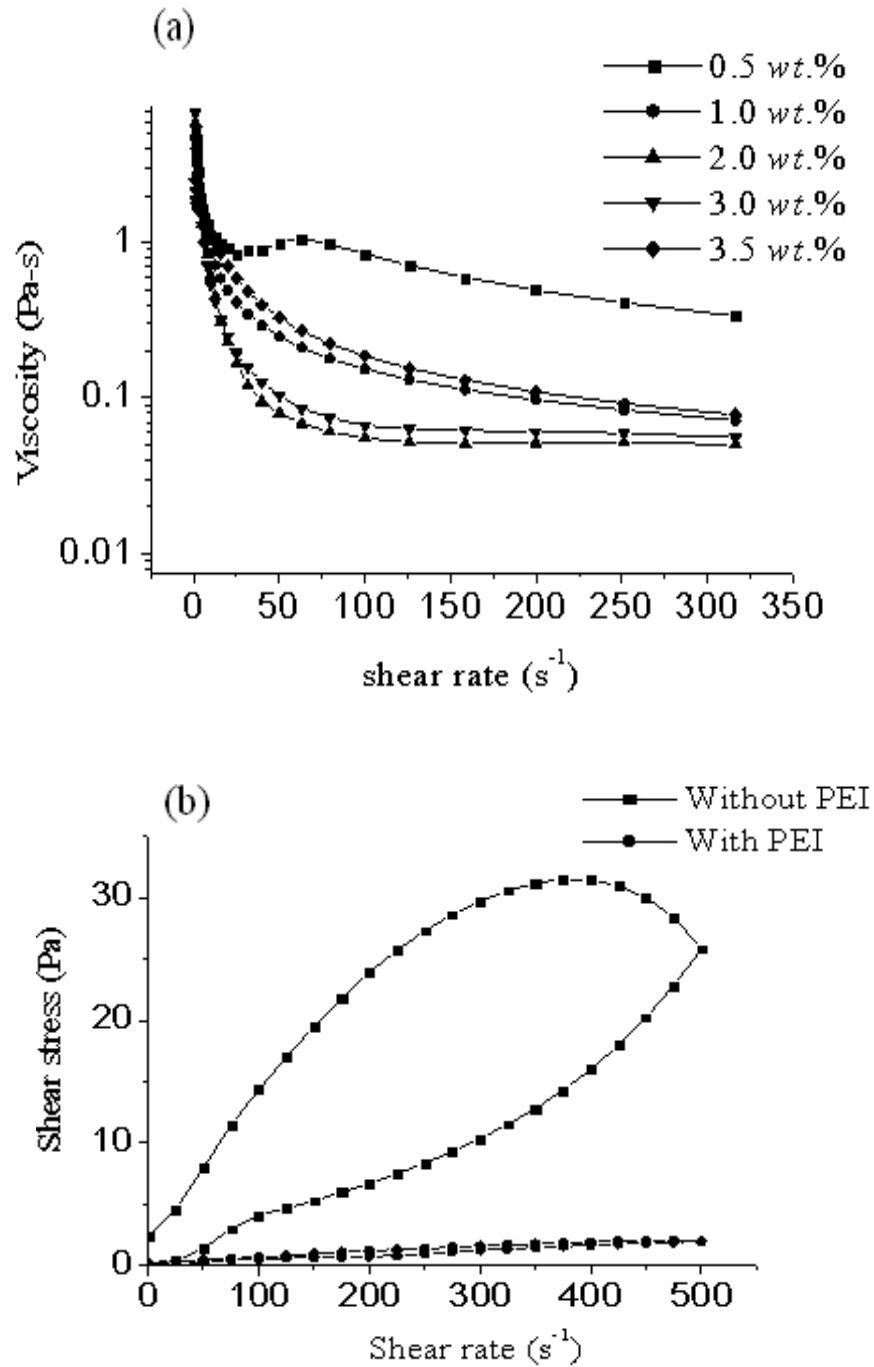
Figure 4-45. (a) Shear rate dependence of steady-state viscosity for CNT slurries containing various amounts of PEI. (b) Shear rate dependence of thixotropic-state shear stress for CNT slurries without or with 2 *wt*.% PEI.

molecular structure of PEI promotes the dissolution of PEI in NMP. As revealed by previous structure analyses, the PEI possesses the aromatic-imide, amide and aromatic functional groups. They enhance the total polarization and hence the dissolution of PEI in NMP. When PEI adsorbs on CNTs, it changes the non-polarization feature of CNTs and enables the wetting of NMP on CNTs. This also explains the viscosity decrease of CNTs slurries containing appropriate amount of PEI and thus the fine dispersion of CNTs in the aqueous suspension.

4.4.5. Sedimentation Behaviors

The sedimentation measurement is a typical way to examine the colloidal stability. An appropriate dispersant enables the suspensions retain the cloudy state, resulting in a small final sedimentation volume.[18,23] Figure 4-46 depicts the sedimentation volumes of CNTs slurries as a function of PEI concentrations. The sedimentation volume first decreases with the increase of PEI concentration, indicating the formation of a denser CNTs structure in sediment. For the slurries with PEI concentrations exceed 2.0 *wt*.%, the sedimentation volumes become relatively insensitive to the change of PEI concentration. The results above indicates that the minimum sedimentation volume occurs in the CNTs slurry containing 2 *wt*.% PEI and thus, in conjunction with the experimental results of rheological and the adsorption

isotherms measurements described above, it is concluded that the optimum PEI

amount for CNTs dispersion in NMP is 2.0 *wt*.%.
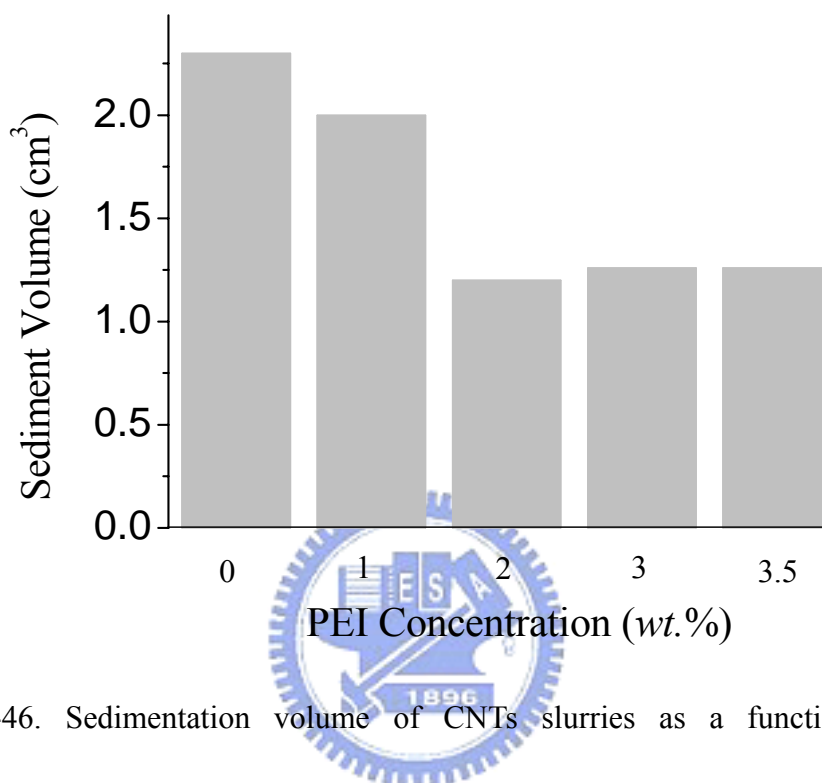
Figure 4-46. Sedimentation volume of CNTs slurries as a function of PEI

concentration.

4.4.6. Microstructure

Figures 4-47(a) and 4-47(b) illustrate the OM morphologies of CNTs in the

slurries free of PEI and with 2 *wt*.% PEI, respectively. The CNTs tangles seriously in

the slurry free of PEI, while the CNTs are well dispersed in the slurry containing PEI.

The dispersion formula was subsequently implanted in the preparation of $LiCoO_2$

electrode for LIBs and the SEM images of composite electrodes containing various

amounts of PEI dispersant are presented in Figs. 4-48(a)-(d). As shown in Fig. 4-48(c), the best CNT dispersion occurs in the electrode containing 2 *wt.*% PEI in which results in a uniform CNT network-like structure. For the electrodes containing less amounts of dispersant, aggregates of CNTs can be clearly seen (see Figs. 4-48(a)-(b)). As to the electrode containing excessive amount of dispersant, the bridging of polymeric dispersant occurs which, in turn, retards the dispersion. Besides, excessive dispersant amount would cause more organic residues in the electrode and then deteriorate the conductivity of electrode.
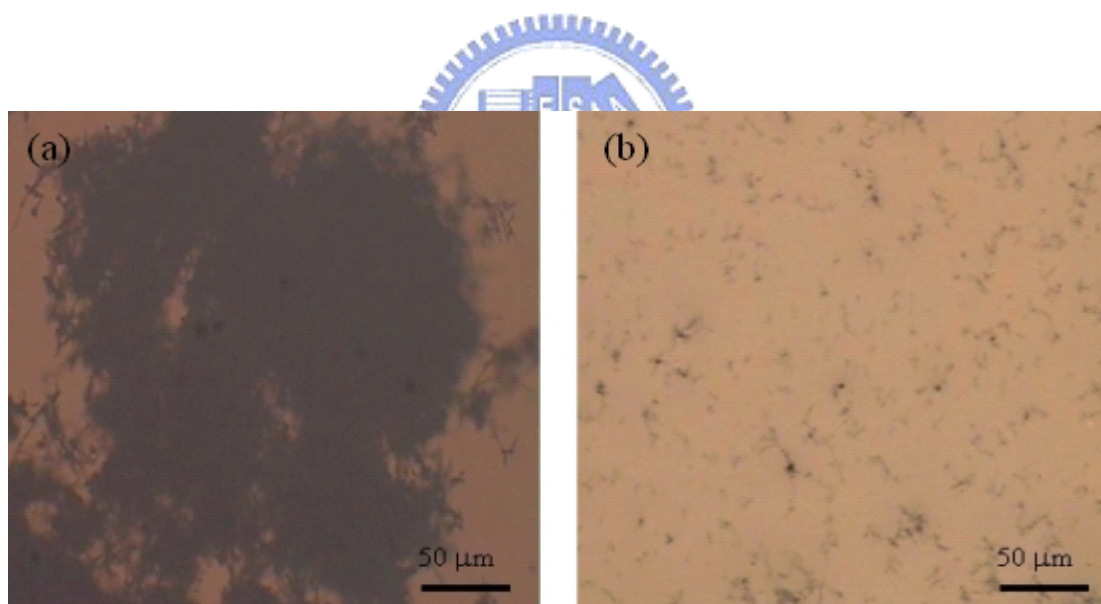
Figure 4-47. The OM morphology of CNTs slurry (a) without and (b) with PEI dispersant.
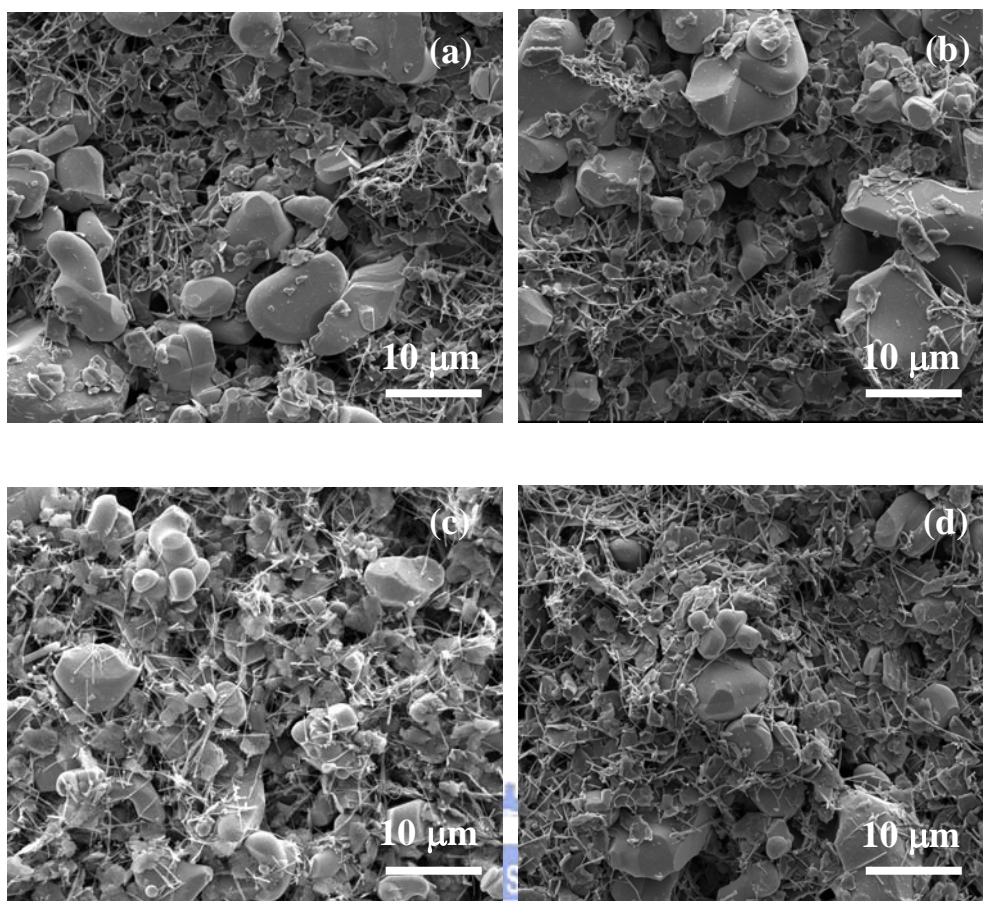
Figure 4-48. SEM micrographs of LiCoO$_2$ electrodes with various amounts of PEI: (a)

0 *wt.%*; (b) 1 *wt.%*; (c) 2 *wt.%*; (d) 3.5 *wt.%*.

4.4.7. Electrical Performance Characterizations

Figure 4-49 shows the ac impedance profiles of the LiCoO$_2$ electrodes containing

various amounts of PEI in the half cells measured by an EIS. The heights of

semicircles of the profiles shown in Fig. 4-49 correspond to the charge-transfer

resistances of test cells. It can be readily seen that the ac resistance decreases from

287 Ω for cell without PEI to 161Ω for the cell at containing 2 *wt.%* of PEI and

further increase of PEI content increases the value or resistance. According to the
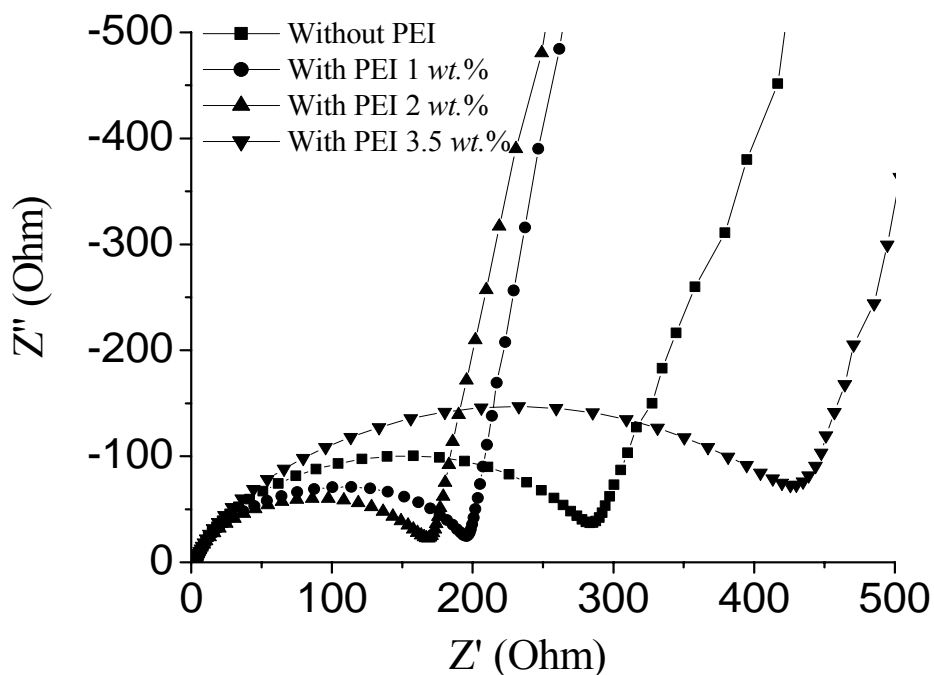
Figure 4-49. The ac impedance profiles of the LiCoO$_2$ electrodes containing various

amounts of PEI in the half cells measured by EIS.
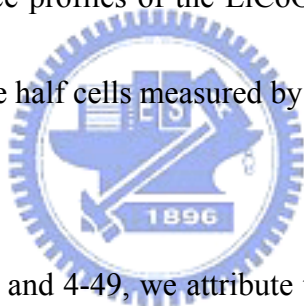
results presented in Figs. 4-48 and 4-49, we attribute the decrease of resistance to the

finely dispersed CNTs which form the network-like structure in the electrode.

Numerous conduction paths established in between the LiCoO$_2$ particles by the

dispersed CNTs provide fluent charge carrier transport and thereby promote the

conduction of electrode. Further, our thermal characterization of PEI indicated that

about 85% of PEI is decomposed away at 140°C, *i.e.*, the highest temperature the test

LIB cells experienced during the assembly. The relatively small amount of PEI

residues in the electrode seems not deteriorate its conductivity as well as the

electrochemical behaviors presented as follows.

Figure 4-50 depicts the cyclic voltammograms of the test cells without and with 2 *wt.%* PEI in LiCoO$_2$ electrode measured in between 2.9 and 4.2 V. It can be seen that the two profiles of the test cells are almost overlap, indicating that the incorporation of PEI in electrode does not affect no electrochemical behaviors of the cells. The cycling performance of the test cells without and with 2 *wt.%* PEI in electrode measured by a charge/discharge unit (Arbin, model BT2042, USA) is shown in Fig. 4-51. The test cell containing 2 *wt.%* PEI obviously exhibits the better capacity retention in comparison with the cell free of PEI. For the cell containing 2 *wt.%* PEI, its capacity retention remains good at about 128 mAh/g after 50 cycles, which is about 93% of value at first cycle (137 mAh/g). On the other hand, the retention capacity of the cell without PEI drops to 106 mAh/g after 50 cycles, which is about 79% of value at first cycle (133 mAh/g).

4.4.8. C-rate Performance of LIB

C-rate behavior of LIB is mainly controlled by Li ion diffusion in LiCoO$_2$ cathode, but the cathode's conductivity also plays a part. Figure 4-52 shows the discharge curves of two test batteries (cathodes with and without PEI addition) under different discharge rates of 0.2 to 8.0 C current densities. In 0.2 C discharge, the two discharge curves almost overlap each other with a capacity value of 140 mAh/g,
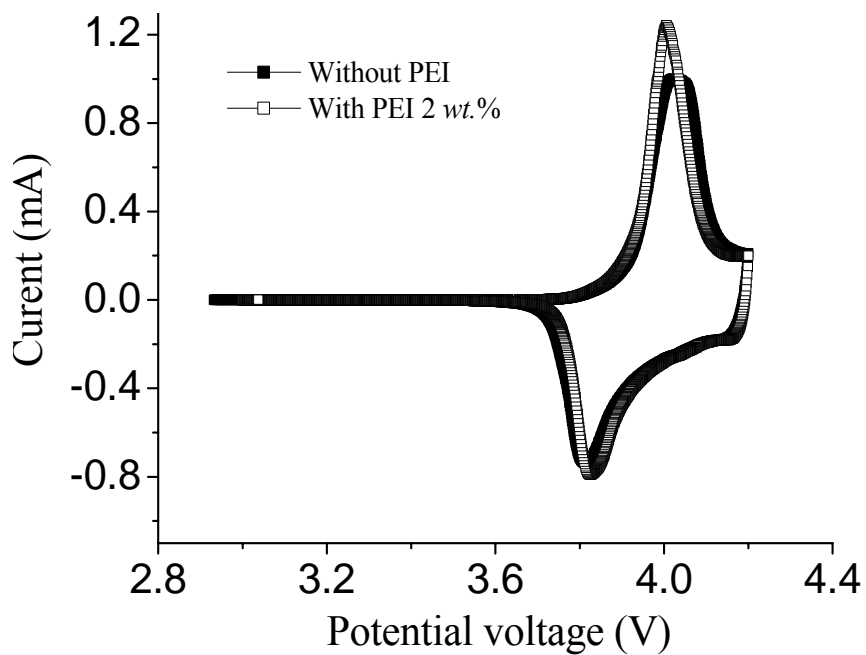
Figure 4-50. Cycle voltammograms of LIB test cells without or with 2 *wt.* PEI in
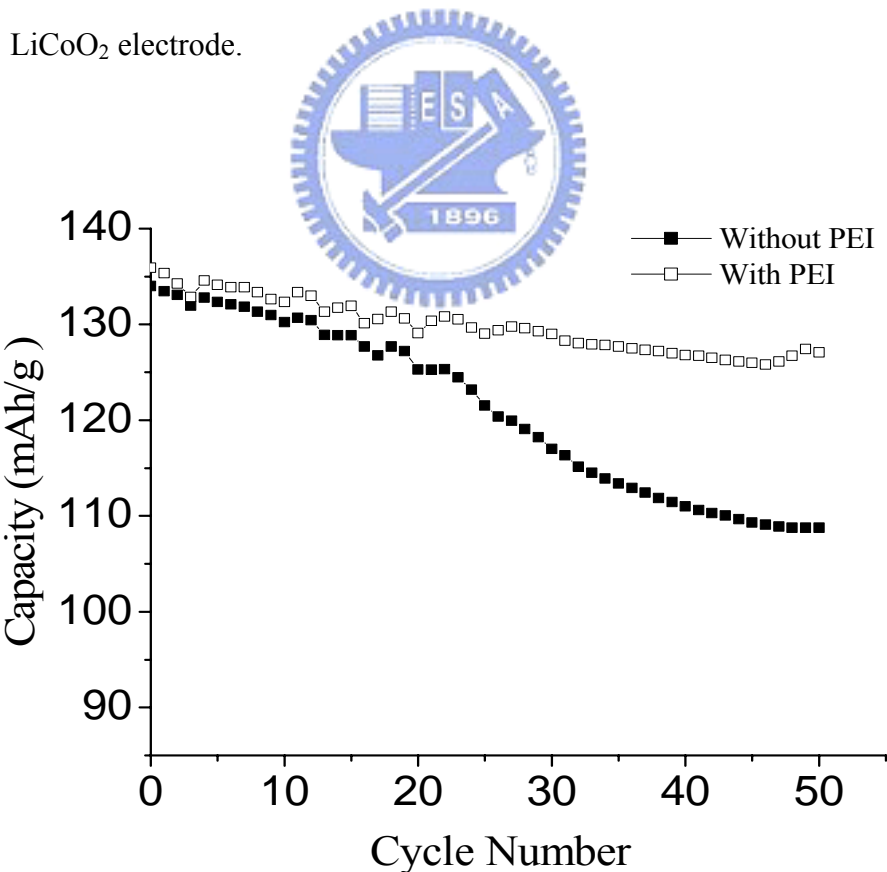
LiCoO$_2$ electrode.

Figure 4-51. The cycle performance at 1 C rate of test battery cells without or with 2

wt. PEI in LiCoO$_2$ electrode at the rate of 1.0-C current density.

indicating a negligible effect of the CNTs addition. But at a discharge current as high as 8.0 C, the two capacity values differ. The battery without PEI has a much lower capacity of 36 mAh/g, which is only 25% of its 0.2 C-discharge capacity. On the other hand, the battery in which composite cathode contains 2 *wt.*% PEI has a discharge capacity of 101 mAh/g, equals to 74% of its 0.2 C-discharge capacity. Since the compositions in both batteries are the same (same weight percent of $LiCoO_2$, binder, and conducting additive), diffusion behaviors in both cathodes are expected to be similar. Since the C-rate performance is controlled by the diffusion behavior and conductivity of cathode, as the diffusion behaviors being similar, the difference is hence lies on the conductivity. The LIB with the cathodes containing well dispersed CNT exhibit a higher discharge capacity because of the efficient charge carrier transport through the electrode. The reason that the dispersion shows no obvious improvement on 0.2-C discharge capacity is due to the relatively small discharge current flow. In such a case, the increase of conducting paths does not mean much for electron transport and thus the benefit resulted from CNT dispersion is obscure. On the contrary, in 8C discharge test, it requires more charge carrier transport paths since the current flow is large. The CNT network might act as a parallel circuit and benefit of resulted from the dispersion became obvious. It reduced the possible current crowding and allowed a fluent electron flow in the modified electrode. Hence an
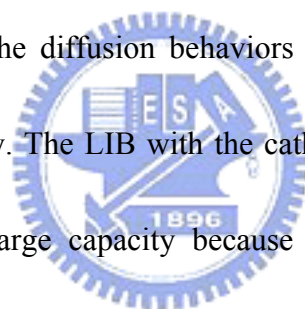
enhancement of 8-C discharge capacity was observed. The results of high rate

capability and long cycle life evidences the promising applications of such a LIB to

power sources, *e.g.*, power tools, electric bicycle, electric motorcycle, *etc*.

Figure 4-52. Discharge curves of LIB test cells without or with 2 *wt.* PEI in $LiCoO_2$

electrode. The two nearly overlapped profiles on the top of the figure are

the charging curves of test cells at the rate of 0.2-C current density.

Chapter 5

Conclusions

This thesis studies the dispersion techniques and its applications to the fabrication nano-scale BTO-relating ceramics and $LiCoO_2$ electrode in LIBs. The major conclusions of this work are summarized in below:

(1) Nano-scale powder materials must be dispersed in order to eliminate the agglomeration caused by van der Waals attraction. This study demonstrated that adding appropriate amount of chemical dispersants (*e.g.*, PMAA-Na or PDAAE) into the ceramics followed by a mechanical grinding/mixing process may effectively reduce the aggregation of nano-scale particles.

(2) In nano-BTO, it was found that distinct room-temperature dielectric properties (dielectric constant = 8000; dielectric loss = 5×10^{-3}) could be achieved in the sample sintered at 1100°C for 6 hrs which possesses relatively small grain sizes about 140 nm and high density (about 95% T.D.). This clearly demonstrated that good dielectric properties could be obtained by a relatively low temperature sintering when nano-scale ceramic powders were adopted. Experimental analyses revealed that due to the large SSA of nano-scale powder, interface-driven mass

transport processes shifts the grain growth to the early stage of nano-BaTiO₃ sintering in comparison with conventional process.

(3) In nano-BST, the best dielectric properties were obtained in the samples sintered at 1200°C for 6 hrs (grain size ≈ 200nm; dielectric constant = 9700; dielectric loss = 4×10^{-2}) or at 1300°C for 1 hr (grain size ≈ 220nm; dielectric constant = 9800; dielectric loss = 7.5×10^{-2}). The improvement of dielectric properties was attributed to the addition of Sr element as well as the fine grain structure in nano-BST samples. In addition, the Tc of nano BST was lower than conventional BST system. The T_C is about 40°C for the sample sintered at 1200°C while the T_C for the sample sintered at 1300°C is about 20°C.

(4) In La-doped BST, addition of La₂O₃ retards both densification and grain growth and the inhibition effects were satisfactorily explained on the basis of La segregate in grain boundaries. The best dielectric properties were obtained in the 1.0LBST sample sintered at 1400°C for 1 hr (grain size ≈ 200nm; dielectric constant = 13800; dielectric loss =$2.8E^{-4}$). The improvement of dielectric properties was attributed to the emergence of Ba^{2+}/Sr^{2+} vacancies, lattice distortion and fine grain microstructure. The 1.0LBST sample possesses lower T_C's in comparison with conventional BST and BTO samples. The lower Tc was attributed to the fine grain structure of nano-LBST samples.

(5) In comparison with conventional ceramics, the nano-ceramics possess advantages including: (*i*) lower sintering temperature; (*ii*) better dielectric properties and (*iii*) shift the *Tc* to lower temperature.

(6) A hyperbranched polymer, PEI, was synthesized as the dispersing agent for CNTs slurry containing NMP solvent. The shear-thinning behaviors observed by rheological measurements as well as the minimum sedimentation volume measurement indicated that optimum amount of PEI for the dispersion of CNTs in slurry is about 2 *wt*.%. Dispersion mechanism for CNTs was attributed to the steric effect resulted from the highly branched structure of PEI. For the electrode with 2 *wt*.% optimal dispersant content, the ac resistance decreased from 287 Ω for cell without PEI to 161Ω for the cell at containing 2 *wt*.% of PEI. This is ascribed to the CNTs network that promotes the charge carrier migration in electrode. The high-rate discharge test indicated that the LIB with modified electrode possesses 8 C-discharge capacity of 101 mAh/g, which is about 74% of its 0.2 C-discharge capacity. The results of high rate capability and long cycle life evidences the promising applications of such a LIB to power sources, *e.g.*, power tools, electric bicycle, electric motorcycle, *etc*.
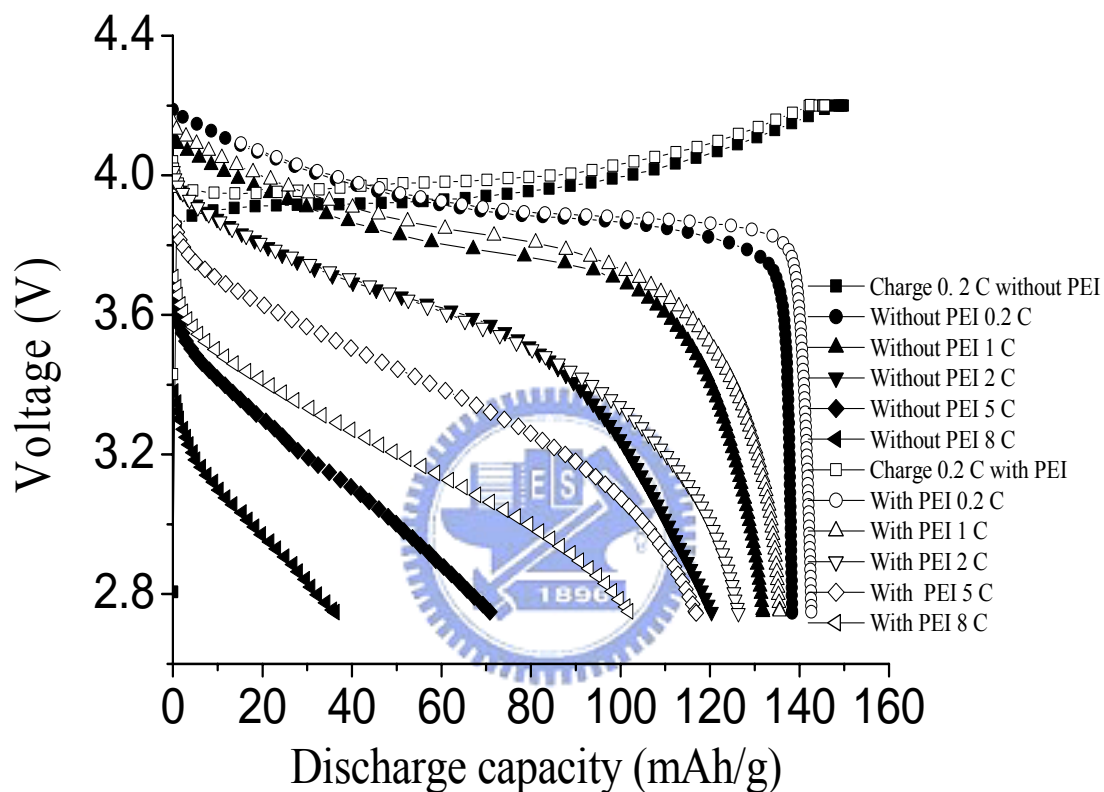
Chapter 6

Future Works

6.1. Nano-ceramics:

In this research, though the best dielectric properties is obtained 1.0LBST sample,

its sintering temperature is still too high. In the future, if the initial particle size can be

reduced to less than 10 nm, a sintering temperature less than 1000°C and further

improvement on dielectric properties can be expected.

At present, the explanations relating to the dielectric properties of ferroelectric

materials are in essential for the conventional micrometer-scale samples. For

nano-ceramics, there exist many ambiguities requiring further in-depth study, in

particular, the fundamental studies on the relationships of microstructure and

dielectric properties. For instance, the effects of internal stress on dielectric properties,

the domain structure in nano-ceramics, the phase transition behaviors at T_C, *etc*. must

to be clarified so that the origin of dielectric properties of nano-ceramics could be

understood.

6.2. CNT-relating Researches:

We successfully synthesized the chemical dispersant that is compatible to the

LiCoO$_2$ electrode preparation utilizing the highly polar NMP solution. The primary

study clearly demonstrates its feasibility to high-power LIBs, however, in order to make this research complete, further researches including life time test, high power electrical measurements and applicability to other electrode materials have to be carried out. Besides, CNT has a relatively high mechanical strength and electrical conductivity. So, one should extends the applications of the finely dispersed CNTs to various occasions such as reinforcement of composites or conductive plastics, chemical or force sensors, electromechanical devices, *etc*.

References

1. 張立德，牟季美主編，*奈米材料科學*， 遼寧科學技術出版社，(2001)。

2. 林振隆主編，*奈米材料導論*， 學富文化事業有限公司，(2002)。

3. 曹茂盛，*超微顆粒製備科學與技術*， 哈爾濱工業大學出版社，(1995)。

4. J. Cesarno and I.A. Aksay, "Stability of aqueous Al_2O_3 suspensions with poly(methacrylic acid) polyelectrolyte", *J. Am. Ceram. Soc.*, **71**(5)(1988), p.250-255.

5. T.S. Yeh and M.D. Sacks, "Low temperature sintering of alumina oxide", *J. Am. Ceram. Soc.*, **71**(10)(1988), p.841-844.

6. T.S. Yeh and M.D. Sacks, "Effect of particle size distribution on the sintering of alumina", *J. Am. Ceram. Soc.*, **71**(12)(1988), p.484-487.

7. K.S. Chou and L.J. Lee, "Effect of dispersants on the rheological properties and slip casting of concentrated alumina slurry", *J. Am. Ceram. Soc.*, **72**(9)(1989), p.1622-1627.

8. F. Zok, F.F. Lange and J.R. Porter, "Packing density of composite powder mixtures", *J. Am. Ceram. Soc.*, **74**(8)(1991), p.1880-1885.

9. V.A. Hackley, "Colloidal processing of silicon nitride with poly(acrylic acid)", *J. Am. Ceram. Soc.*, **80**(5)(1997), p.2315-2325.

10. H. Kamiya, Y. Fukuda, Y. Suzuki and M. Tsukada, "Effect of polymer dispersant structure on electrosteric interaction and dense alumina suspension behavior", *J. Am. Ceram. Soc.*, **82**(5)(1999), p.3407-3412.

11. P.L. Kuo, T.C. Chang and L.M. Lu, "Functional polymers for colloidal applications", *J. Appl. Polym. Sci.*, **44**(1992), p.859-867.

12. Y. Liu, G. Lian and J.Sun, "Effect of acrylic copolymer adsorption on the colloidal stability of a 3Y-TZP suspension", *J. Euro. Ceram. Soc.*, **22**(2002), p.863-871.

13. J.A. Lewis, "Colloidal processing of ceramics", *J. Am. Ceram. Soc.*, **83**(10)(2000), p.2341-2359.

14. R.G. Horn, "Surface force and their action in ceramics materials", *J. Am. Ceram. Soc.*, **73**(5)(1990), p.1117-1135.

15. K.N. Israelachvili, *Intermolecular and Surface Force*, 2nd edition, Academic Press, New York, (1992).

16. D.J. Shaw, *Introduction to Colloid and Surface Chemistry*, Butterworth Heinemann, Oxford, (1992), p.214.

17. D.H. Napper, *Polymeric Stabilization of Colloidal Dispersions*, Academic Press, London, (1983).

18. 虞邦英，*鈦酸鋇膠粒於水基溶液中之表面吸附及分散研究*，國立台灣大學材料科學與工程研究所論文，(2001)。

19. 汪建民主編，*介電陶瓷，* 陶瓷技術手冊，中華民國粉末冶金協會，(1999)。

20. J.S. Reed, *Principles of Ceramics Processing*, Wiley and Sons, New York, (1995).

21. W.M. Sigmund, "Novel powder-processing methods for advanced ceramics", *J. Am. Ceram. Soc.*, **83**(5)(2000), p.1557-1574.

22. H.G. Pedersen and L. Bergstrom, "Forces measured between zirconia surface in poly(acrylic acid) solutions", *J. Am. Ceram. Soc.*, **82**(1)(2001), p.1675-1682.

23. 陳志豪，*高分子分散劑之合成以及對於鈦酸鋇粉末的分散性質*，國立台灣師範大學化學研究所論文，(2005)。

24. 陸立美，*聚丙烯酸系構造對其分散性之影響*，國立成功大學化學研究所論文，(1989)。

25. R.C. Devries, "Microstructure of barium titanate ceramics", *J. Am. Ceram. Soc.*, **40**(6)(1957), p.200-206.

26. M. Kahn, "Influence of grain growth on dielectric properties of Nb-doped BaTiO$_3$", *J. Am. Ceram. Soc.*, **54**(9)(1971), p.455-457.

27. A. Yainaji, Y. Enomoto and T. Murakami, "Preparation, characterization, and properties of Dy-doped small-grained BaTiO$_3$ ceramics", *J. Am. Ceram. Soc.*, **60**(3)(1977), p.97-101.

28. 邱碧秀，*電子陶瓷材料*，徐氏基金會，(1992)，461-464 頁。

29. W.R. Cook, "Domain twinning in barium titanate ceramics", *J. Am. Ceram. Soc.*, **68**(4)(1956), p.17-19.

30. D.F.K. Hennings, R. Janseen and P.J.L. Reyene, "Control of liquid-phase-enhanced discontinuous grain growth in barium titanate", *J. Am. Ceram. Soc.*, **70**(1)(1987), p.23-27.

31. W.D. Kingery, H.K. Bowen and D.R. Uhalmann, *Introduction to Ceramics*, 2nd edition, Wiley, New York, (1976).

32. L.A. Xue, "The kinetics of hot-pressing for undoped and donor-doped BaTiO$_3$", *J. Mater. Sci.*, **25**(1990), p.123-128.

33. H. Schmelz, "Shrinkage and initial grain growth in BaTiO$_3$ ceramics", *J. Mater. Sci.*, **14**(1981), p.203-207.

34. Y. Enomoto and A. Yamaji, "Preparation of uniformly small-grained BaTiO$_3$", *Am. Ceram. Soc Bull.*, **60**(5)(1981), p.566-570.

35. L.A. Xue, "Thermodynamic benefit of abnormal grain growth in pore elimination during sintering", *J. Am. Ceram. Soc.*, **72**(8)(1989), p.1536-1537.

36. H.U. Anderson, "Initial sintering of BaTiO$_3$ compacts", *J. Am. Ceram. Soc.*, **48**(3)(1965), p.118-121.

37. J. Nowotny and M. Rekas, "Defect structure, electrical properties and transport in barium titanate", *Ceram. Int*., **20**(1994), p.265-275.

38. H.C. Ling and A.M. Jackson, "Correlation of silver migration with temperature-humidity-bias (THB) failures in multilayer ceramic capacitors", *IEEE Transactions on Components, Hybrids, and Manufacturing Technology,* **12**(1)(1989), p.1709-1712.

39. C.H. Wang and L. Wu, "Lead borate glass-a new sintering agent for BaTiO$_3$ ceramics", *Jpn. J. Appl. Phys*., **32**(1993), p.2020-2024.

40. Y. Matsuo and H. Saski, "Exaggerated grain growth in liquid phase sintering of BaTiO$_3$", *J. Am. Ceram. Soc*., **54**(9)(1971), p.471-475.

41. K.S. Mazdiyasni and L.M. Brown, "Microstructure and electrical properties of Sc$_2$O$_3$-doped, rare-Earth-oxide-doped, and undoped BaTiO$_3$", *J. Am. Ceram. Soc.*, **54**(1971), p.539-543.

42. W.R. Buessern, L.E. Cross and A.K. Goswami, "Phenomenological theory of high permittivity in fine-grained barium titanate", *J. Am. Ceram. Soc*., **49**(1)(1966), p.33-36.

43. H.T. Martirena and J.C. Burfoot, "Grain-Size effect on properties of some ferroelectric ceramics", *J. Phy. Soc.*, **7**(1974), p.3182-3192.

44. G. Arlt and D. Hennings, "Dielectric properties of fine-grained barium titanate", *J. Appl. Phys.*, **58**(9)(1985), p.1619-1625.

45. P. Murugaraj, T.R. Kutty and M.S. Rao, "Diffuse phase transformation in neodymium-doped BaTiO$_3$ ceramics", *J. Mater. Soc.*, **21**(1986), p.3521-3527.

46. M. Kahn, "Preparation of small-grained and large-grained ceramics from Nb-doped BaTiO$_3$", *J. Am. Ceram. Soc.*, **54**(9)(1971), p.452-454.

47. T.M. Harkulich, J. Magder, M.S. Vukasovich and R.J. Lockhart, "Ferroelectrics of ultrafine particle size", *J. Am. Ceram. Soc.*, **54**(11)(1971), p.548-553.

48. I. Burn, "Mn-doped polycrystalline BaTiO$_3$", *J. Mater. Soc.*, **14**(1979), p.2453-2458.

49. D. Hennings and G. Rosenstein, "Temperature-stable dielectrics based on chemically inhomogeneous BaTiO$_3$", *J. Am. Ceram. Soc.*, **67**(4)(1984), p.249-254.

50. H. Emoto and J. Hojo, "Sintering and dielectric properties of BaTiO$_3$-Ni composite ceramics", *J. Am. Ceram. Soc.*, **100**(4)(1992), p.553-557.

51. J.O. Besenhard, *Handbook of Battery Materials*, Wiley-VCH, Weinheim (1999)

52. S. Ijima, "Helical microtubules of graphitic carbon", *Nature*, **354**(6348)(1991), p. 56-58.

53. A. Pm and S. Ijima, "Smallest carbon nanotube", *Nature*, **358**(6381)(1992), p. 23-24.

54. J.H. Jeon, "Effect of $SrTiO_3$ concentration and sintering temperature on microstructure and dielectric constant of $Ba_{1-x}Sr_xTiO_3$", *J. Eur. Ceram. Soc.*, **24**(1996), p.1045-1049.

55. L.P. Chen, K.L. Ying and K.C. Hsu, "An amphibious water-soluble copolymer: (I) synthesis and its dispersing ability on barium titanate", *J. Appl. Polym. Sci.*, **92**(4)(2004), p.2232-2239.

56. H.V. Alexandru, C. Berbecaru, and A. Ioachim, "Oxides ferroelectric (Ba,Sr)TiO_3 for microwave devices", *Mater. Sci. Eng. B*, **109**(2004), p.152-159.

57. O.P. Thakur, C. Prakash, and D.K. Agrawal, "Dielectric behavior of $Ba_{0.95}Sr_{0.05}TiO_3$ ceramics sintered by microwave", *Mater. Sci. Eng. B*, **96**(2002), p.221-225.

58. V.V. Lemanov, E.P. Smirnova, P.P. Syrnikov, and E.A. Tarakanov, "Phase transitions and glasslike behavior in $Sr_{1-x}Ba_xTiO_3$", *Phys. Rev. B*, **54**(5)(1996), p.3151-3157.

59. G. Patermarkis, "The parallel dehydrative and dehydrogenative catalytic action

of Al_2O_3 pure and doped by MgO Kinetics, selectivity, time dependence of catalytic behavior, mechanisms and interpretations", *Applied Catalysis A.*, **252**(2003), p.231-236.

60. R.C. Buchanan, *Ceramic Materials for Electronics*. 3rd edition, Basel, New York, (2002).

61. H.L. Ming, and Y.L. Hong, "Densification retardation in the sintering of La_2O_3-doped barium titanate ceramic", *Mater. Sci. Eng. A*, **323**(2002), p.167-176.

62. L.J. Hobson, and J.W. Feast, "Poly(amidoamine) hyperbranched systems: synthesis, structure and characterization", *Polymer*, **40**(1999), p.1279-1297.

63. C.F. Shu, C.M. Leu, and F.Y. Huang, "Synthesis, modification, and characterization of hyperbranched poly(ether ketones)", *Polymer*, **40**(1999), p.6591-98.

64. M. Johanasson, E. Malmstrom, and H. Anders, "The synthesis and Properties of Hyperbranched Polyesters", *Polymer Sci.*, **4**(1996), p.398-403.

65. M. Rikukawa, and K. Sanui, "Proton-conducting polymer electrolyte membranes based on hydrocarbon polymer", *Polymer Sci.*, **25**(2000), p.1463-1502.

66. A.J. Varma, J.F. Kennedy, and P. Galgali, "Synthetic polymers functionalized by carbohydrates: a review", *Polymer*, **4**(2004), p.429-445.

67. B.J. Briscoe, U. Asad, and P.F. Luckham, "Optimising the dispersion on alumina suspension using commercial polyvalent electrolyte dispersants", *J. Eur. Ceram. Soc.*, **18**(1998), p.2141-2147.

68. B.A. Firth, and R.J. Hunter, "Flow properties of coagulated colloidal suspensions, Ⅲ. The elastic floc model", *J. Colloid Interface Sci.*, **57**(1976), p.266-275.

69. A.S. Michaels, and J.C. Bolger, "The plastic flow behavior of flocculated kaolin suspensions", *Ind. Eng. Chem. Fundam.*, **1**(1962), p.153-162.

Curriculum Vitae

Kuo-Liang Ying (應國良)

PERSONAL DATA

Born: May 07, 1977, Kaohsiung City, Taiwan

Nationality: Taiwan, the Republic of China

Office Address: Department of Materials Science and Engineering, National Chiao

Tung University, 1001 Ta-Hseuh Road, Hsinchu, Taiwan, ROC.

Tel: 886-3-5712121 ext.55338

E-mail: hsin_i_0507@yahoo.com.tw

EDUCATION

Ph. D. of, Department of Materials Science and Engineering, National Chiao Tung

University, Hsinchu, Taiwan, ROC. October 2007

Master of, Department of Chemistry, National Taiwan Normal University, Taipei,

Taiwan, July 2003

Bachelor of, Department of Chemistry, Soochow University, Taipei, Taiwan, July

2000

Publications:

Journal Papers

1. **Kuo-Liang Ying** and Tsung-Eong Hsieh, "Dispersion of Nano-scale $BaTiO_3$ Suspensions by the Combination of Chemical and Mechanical Grinding/Mixing Processes", *J. Appl. Polym. Sci.*, (2005)

2. **Kuo-Liang Ying** and Tsung-Eong Hsieh, "Sintering Behaviors and Dielectric Properties of Nanocrystalline Barium Titanate", *Materials Science and Engineering B,* (2006)

3. **Kuo-Liang Ying**, Tsung-Eong Hsieh and Yi-Feng Hsieh, "Colloidal Dispersion of Nano-scale ZnO Powders Using Amphibious and Anionic Polyelectrolytes", *Cearm. International*, (2007)

4. **Kuo-Liang Ying,** Jung-Cheng Lin, Tsung-Eong Hsieh, "A Novel Chemical Dispersant for the Dispersion of Carbon Nanotube and Its Applications to High-Power Lithium-ion Battery", *Electrochemistry Comm.,* (2007)

5. **Kuo-Liang Ying**, Jung-Cheng Lin, Tsung-Eong Hsieh, "A New Chemical Dispersant for the Dispersion of Carbon Nanotube: Synthesis, Characterizations and Its Application to $LiCoO_2$ Electrode in Lithium Ion Battery", *J. Appl. Polym. Sci.*, (2007)

6. **Kuo-Liang Ying** and Tsung-Eong Hsieh, "Sintering Behaviors, Microstructure and Dielectric Properties of Nano-$Ba_{0.7}Sr_{0.3}TiO_3$ Ceramic", *J. J. Appl. Physics,*

(2007)

7. **Kuo-Liang Ying** and Tsung-Eong Hsieh, "Sintering Behaviors and Dielectric Properties of Nano La_2O_3-doped $(Ba,Sr)TiO_3$", *Preparedness* (2007)